UNICAMP

Universidade Estadual de Campinas
Instituto de Física "Gleb Wataghin"

Rodrigo Menezes Forti

Translation of a diffuse optical system for monitoring neurocritical patients

Translação de um sistema de óptica de difusão para monitoramento de pacientes neurocríticos

CAMPINAS
2020

Rodrigo Menezes Forti

Translation of a diffuse optical system for monitoring neurocritical patients

Translação de um sistema de óptica de difusão para monitoramento de pacientes neurocríticos

Tese apresentada ao Instituto de Física "Gleb Wataghin" da Universidade Estadual de Campinas como parte dos requisitos exigidos para a obtenção do título de Doutor em Ciências.

Thesis presented to the Institute of Physics of the University of Campinas in partial fulfillment of the requirements for the degree of Doctor in Sciences.

Supervisor/Orientador: Prof. Dr. Rickson Coelho Mesquita

Este exemplar corresponde à versão final da Tese defendida por Rodrigo Menezes Forti e orientada pelo Prof. Dr. Rickson Coelho Mesquita.

CAMPINAS
2020

Ficha catalográfica
Universidade Estadual de Campinas
Biblioteca do Instituto de Física Gleb Wataghin
Lucimeire de Oliveira Silva da Rocha - CRB 8/9174

F776t

Forti, Rodrigo Menezes, 1990-
Translation of a diffuse optical system for monitoring neurocritical patients / Rodrigo Menezes Forti. – Campinas, SP : [s.n.], 2020.

Orientador: Rickson Coelho Mesquita.
Tese (doutorado) – Universidade Estadual de Campinas, Instituto de Física Gleb Wataghin.

1. Espectroscopia ótica de difusão. 2. Espectroscopia de correlação de difusão. 3. Circulação cerebral. 4. Transtornos cerebrovasculares. 5. Tratamento endovascular. I. Mesquita, Rickson Coelho, 1982-. II. Universidade Estadual de Campinas. Instituto de Física Gleb Wataghin. III. Título.

Informações para Biblioteca Digital

Título em outro idioma: Translação de um sistema de óptica de difusão para monitoramento de pacientes neurocríticos
Palavras-chave em inglês:
Diffuse optical spectroscopy
Diffuse correlation spectroscopy
Cerebral circulation
Cerebrovascular disorders
Endovascular treatment
Área de concentração: Física
Titulação: Doutor em Ciências
Banca examinadora:
Rickson Coelho Mesquita [Orientador]
Alessandra Tomal
Mônica Alonso Cotta
Cristina Kurachi
William Andrew Kofke
Data de defesa: 28-01-2020
Programa de Pós-Graduação: Física

Identificação e informações acadêmicas do(a) aluno(a)
- ORCID do autor: https://orcid.org/0000-0002-8978-2525
- Currículo Lattes do autor: http://lattes.cnpq.br/4812232048454506

Universidade Estadual de Campinas
Instituto de Física "Gleb Wataghin"

Membros da comissão julgadora da tese de doutorado de Rodrigo Menezes Forti (RA 084092), apresentada e aprovada ao Instituto de Física "Gleb Wataghin", da Universidade Estadual de Campinas, em 28/ 01 / 2020.

Comissão julgadora:

- Prof. Dr. Rickson Coelho Mesquita
  DRCC/IFGW/UNICAMP
- Profa. Dra. Alessandra Tomal
  DFA/IFGW/UNICAMP
- Profa. Dra. Mônica Alonso Cotta
  DFA/IFGW/UNICAMP
- Profa. Dra. Cristina Kurachi
  IFSC/USP
- Prof. Dr. William Andrew Kofke
  University of Pennsylvania, USA

OBS.: A ata da defesa, assinada pelos membros da Comissão Examinadora, consta no SIGA/Sistema de Fluxo de Dissertação/Tese e na Secretaria do Programa da Unidade.

CAMPINAS
2020

To glorify democracy and to silence the people is a farce; to discourse on humanism and to negate people is a lie.
(Paulo Freire, Pedagogy of the Oppressed)

Acknowledgments

Before acknowledging everyone that was essential for the development of my doctorate, it is necessary to acknowledge how privileged I was to have had the opportunity to be part of UNICAMP. I have been at UNICAMP since 2008, when I started my undergraduate degree. At UNICAMP, I had the opportunity to interact with so many people, with very diverse backgrounds. Through many fruitful discussions, I was able to develop many different social and professional skills, which certainly molded me into the person I am today.

I must especially thank my advisor, Rickson Mesquita, who I have been working with for the last 9 years. Rickson have certainly played a major role in my personal development, he was always very thorough in his feedback, which helped me to greatly improve my writing and public speaking skills. I must also thank Rickson for introducing me to the fascinating area of diffuse optics, which has a lot of potential to improve patient care. Through Rickson, I was able to meet many of the world leaders in the clinical applications of diffuse optics, including Dr. Arjun Yodh, who was my advisor at the University of Pennsylvania (Penn). I worked at Penn for a year and a half as part of an exchange program from FAPESP, and I am immensely thankful for my time there. All the feedback from Arjun have hugely improved my critical thinking, as he made me think about every details and implications of everything I ever presented to him.

It is almost impossible to fairly thank everyone who played a role in the development of my doctorate. I must first thank all my friends that were always there to support me, whenever I needed anything. I must especially acknowledge the help from every student of the Laboratory of Biomedical Optics (LOB) at UNICAMP. I am specially grateful for the people from UNICAMP who followed this process more closely and actively, such as Júlia Bertagna, Sérgio Novi, Edwin Forero, Andres Quiroga, Giovanni Hering, Luiz Simioni, Giovani Grisotti and Giacomo Dollevedo. I must also thank everyone from Yodh's lab, all of them were very important for this project as well as my personal growth: Wesley Baker, Kenneth Abramson, Jeffrey Cochran, Tiffany Ko, David Busch, Sanghoon Chong, Lin Wang, Lian He, Yi Hong, Karla Bergonzi, Jonah Padawer. I also have to thank all the clinical researchers, from both UNICAMP and Penn, without whom this project would never have been possible: Christopher Favilla, Julien Menko, Steven Messé, Michael Mullen, John Detre, Nichole Gallatti, Sean Spangler, Ahmad Zamzam, Andrew Kofke, Marilise Katsurayama, Lenise Valler, Li Min Li, Alexandre Falcão. I must also thank all the clinical staff that helped with all the measurements in the clinic.

Finally, I must thank the funding agencies who supported this project. A special thanks is required for the *Fundação de Amparo à Pesquisa no Estado de São Paulo* (FAPESP), which was the main source of support for this project (Proc. 2014/25468-6, and others). Thanks is also in order to the National Institute of Health (NIH), the *Coordenação de Aperfeiçoamento de Pessoal de Nível Superior* (CAPES) and the *Conselho Nacional de Desenvolvimento Científico e Tecnológico* (CNPq) for their support.

Resumo

As doenças cerebrovasculares são uma das principais causas de morte e incapacidade em todo o mundo. Em 2015, mais de 590.000 pacientes foram hospitalizados por estas doenças no Brasil, com aproximadamente 100.000 óbitos. A prevenção de danos secundários é um dos principais objetivos no tratamento de doenças cerebrovasculares graves, como o acidente vascular cerebral (AVC). No entanto, atualmente há uma falta de métodos não invasivos para monitoramento contínuo da fisiologia cerebral. Neste contexto, a espectroscopia óptica de difusão (DOS) e a espectroscopia de correlação de difusão (DCS) foram recentemente propostas como potenciais monitores não invasivos e contínuos capazes de fornecer informações neurofisiológicas em pacientes neurocríticos. Ao incidir luz infravermelha no escalpo, DCS pode medir o fluxo sanguíneo cerebral (CBF) e DOS pode medir as concentrações de oxi e desoxi-hemoglobina. A combinação de DOS e DCS foi explorada anteriormente para monitorar pacientes em vários cenários clínicos, como monitoramento neonatal, durante intervenções cerebrovasculares e para monitoramento de pacientes neurocríticos. No entanto, a confiabilidade da técnica para fornecer informações precisas em tempo real durante medições longitudinais, bem como durante alguns tipos de intervenções clínicas, permanece em grande parte não estudada.

O principal objetivo desta tese foi mostrar que as técnicas de óptica de difusão podem auxiliar de maneira confiável e no monitoramento em tempo real de doenças cerebrovasculares. Para isso, desenvolvemos sistemas baseados em óptica de difusão e testamos a viabilidade destes sistemas em diferentes ambientes clínicos, envolvendo o monitoramento de pacientes dentro de uma unidade de terapia intensiva (UTI), bem como durante o tratamento endovascular de AVC. Primeiro, relatamos a construção e a translação de um sistema híbrido de óptica de difusão, combinando DOS e DCS, para o monitoramento em tempo real da fisiologia cerebral de pacientes internados em uma UTI. Mais especificamente, apresentamos dois estudos de caso, onde mostramos que os parâmetros neurofisiológicos medidos pelas técnicas de óptica de difusão são consistentes com a evolução clínica destes pacientes. Em seguida, relatamos a translação das técnicas de óptica de difusão para monitorar a hemodinâmicas cerebral durante o tratamento endovascular de dois pacientes com oclusões na artéria carótida interna. Nossos resultados identificaram um aumento induzido pela recanalização no CBF ipsilateral, com pouca ou nenhuma alteração no CBF contralateral e no fluxo sanguíneo extracerebral. Nossos resultados mostraram que a óptica de difusão tem grande potencial para monitorar os danos secundários em pacientes neurocríticos, sem interferir com práticas clínicas. Além disso, nossos resultados sugerem que o monitoramento hemodinâmico cerebral com as técnicas ópticas tem potencial para guiar terapias baseadas na fisiologia individual de pacientes. Por fim, para melhorar a confiabilidade das técnicas de ópticas de difusão, também propusemos a implementação de algoritmos aprimorados para a análise de dados. Mostramos que, usando um modelo de duas camadas para DOS/DCS, podemos melhorar a precisão na recuperação das alterações hemodinâmicas cerebrais.

Palavras-chave: Espectroscopia ótica de difusão; Espectroscopia de correlação de difusão; Fluxo sanguíneo cerebral; Transtornos cerebrovasculares; Tratamento endovascular

Abstract

Cerebrovascular diseases are one of the main causes of death and disability worldwide. In 2015, there were more than 590.000 patients hospitalized due to cerebrovascular diseases in Brazil, with approximately 100.000 deaths. Prevention of secondary damage is an important goal in the treatment of severe neurological conditions, such as head trauma and stroke. However, there is currently a lack of non-invasive methods for continuous monitoring of cerebral physiology in real-time. More recently, diffuse optical spectroscopy (DOS) and diffuse correlation spectroscopy (DCS) have been proposed as noninvasive and continuous bedside monitors capable of providing neurophysiology information in neurocritical patients. By shining near-infrared light from the scalp, DCS can measure microvascular cerebral blood flow (CBF), and DOS can measure oxy- and deoxy-hemoglobin concentrations. The combination of DOS and DCS has been previously explored to monitor patients in several clinical scenarios, such as neonatal monitoring, during cerebrovascular interventions, and for monitoring of neurocritical patients. However, the reliability of the technique to provide accurate real-time information during longitudinal (i.e., across multiple days) measurement as well as during a few different clinical interventions remains largely unaddressed.

The main goal of this thesis was to show that diffuse optics can reliably aid in monitoring cerebrovascular diseases, in real-time. To that end, we have translated a diffuse optical system to different clinic environments: during long-term monitoring of patients inside an intensive care unit, as well as during an endovascular treatment of stroke. First, we reported the construction and translation of a hybrid diffuse optical system combining DOS and DCS for real-time monitoring of cerebral physiology in a neuro intensive care unit. By presenting two representative case-studies, we show that the neurophysiological parameters measured by diffuse optics at the bedside are consistent with the clinical evolution of the patients. Then, we reported the translation of diffuse optics to monitor frontal-lobe cerebral hemodynamic changes during endovascular treatment of two patients with ischemic stroke due to internal carotid artery occlusions. The monitoring instrument identified a recanalization-induced increase in ipsilateral CBF with little or no concurrent change in contralateral CBF and extracerebral blood flow. Taken together, our results showed that diffuse optics holds promise for monitoring secondary damage in neurocritical patients, with minimal interference with current clinical practices. Additionally, our results suggest that cerebral hemodynamic monitoring with diffuse optics has the potential to guide therapy based on the individual physiology of neurocritical patients. Last, to improve the reliability of the diffuse optical techniques, we have also proposed the implementation of improved algorithms for data analysis. We showed that by using a two-layer model for DOS/DCS, we can improve the accuracy of diffuse optics in recovering the cerebral hemodynamic changes.

Keywords: Diffuse optical spectroscopy; Diffuse correlation spectroscopy; Cerebral blood flow; Cerebrovascular disorders; Endovascular treatment

List of Figures

List of Tables

List of Abbreviations

ABP	Arterial blood pressure
APD	Avalanche photodiode
aSAH	Aneurysmal subarachnoid hemorrhage
BFI	Blood flow index
CBF	Cerebral blood flow
CBF_v	Cerebral blood flow velocity
CBV	Cerebral blood volume
$CMRO_2$	Cerebral metabolic rate of oxygen
CT	Computed tomography
CTE	Correlation transport equation
CW	Continuous-wave
DCS	Diffuse correlation spectroscopy
DOS	Diffuse optical spectroscopy
DOT	Diffuse optical tomography
DTOF	Distribution of time of flight
EEG	Electroencephalography
FD	Frequency-domain
FWHM	Full width at half maximum
GUI	Graphical user interface
HbO	Oxyhemoglobin
HbR	Deoxyhemoglobin
HbT	Total hemoglobin
Hgb	Hemoglobin concentration in blood
ICA	Internal carotid artery
ICG	Indocyanine green
ICP	Intracranial pressure
ICU	Intensive care unit
IRF	Instrument response function
LI	Laterality index
MAP	Mean arterial pressure

MBLL	Modified Beer-Lambert law
MCA	Middle-cerebral artery
MRI	Magnetic ressonance imaging
mTICI	Modified treatment in cerebral ischemia
NIHSS	National institute of health stroke scale
NIR	Near infrared
NIRS	Near-infrared spectroscopy
OEF	Oxygen extraction fraction
PET	Positron emission tomography
PFC	Pre-frontal cortex
PMT	Photo-multiplier tube
RBC	Red blood cell
rCBF	Relative cerebral blood flow
RTE	Radiative transport equation
SaO_2	Arterial oxygen saturation
SI	Semi-infinite
SNR	Signal-to-noise ratio
SPAD	Single photon avalanche photodiode
StO_2	Oxygen saturation
TCD	Transcranial doppler ultrasound
TCSPC	Time-correlated single photon counting
TD	Time-domain

Contents

Chapter 1

Introduction

Cerebrovascular diseases are one of the main causes of death and disability worldwide. In 2015 alone, there were more than 590.000 patients hospitalized due to cerebrovascular diseases in Brazil, such as stroke, with approximately 140.000 deaths [1]. The prevalence of cerebrovascular diseases is age-dependent, and since the life expectancy is increasing, the global burden and prevalence of cerebrovascular diseases will also increase, with a disproportionate increase likely in low- and middle-income countries.

One of the main goals in the care of patients with severe cerebrovascular injury is to prevent secondary damage. Additional insults following the primary damage affect and may be affected by both systemic (e.g., arterial blood pressure, ABP) and cerebral physiologies (e.g., cerebral blood flow, cerebral metabolism and cerebral oxygenation) [2–5]. To this end, close patient monitoring following acute brain lesions is essential to prevent secondary damage, and it may directly improve mortality and morbidity rates [6–8]. However, continuous cerebral monitoring often requires invasive catheters that measure brain parenchymal vascular physiology [6]. These devices, however, are typically very expensive and only provide data from a single subcortical location. They are also impractical for hyperacute stroke due to both the time required to place them and the risk of tissue injury and/or hemorrhage, particularly in patients treated with intravenous thrombolysis or antithrombotic medications. Furthermore, due to its invasiveness, continuous cerebral monitoring has only been employed in a few, more severe cases, and it is seldom available in low-budget environments. Less invasive brain imaging techniques, such as computed tomography (CT) and magnetic resonance imaging (MRI), may provide quantification of the cerebral physiology, but these diagnostics usually require transport to an imaging suite, utilize exogenous contrast agents, and/or generally offer only snapshots in time.

Among the few potential noninvasive techniques to probe brain physiology at the patient's bedside, Transcranial Doppler ultrasound (TCD) is generally used to monitor cerebral blood flow velocity (CBF_v) in the large arteries [9]. However, TCD is operator-dependent, not suitable for long-term monitoring, and is not sensitive to changes at the microvasculature. Additionally, placement of TCD probes requires a skilled operator, and approximately 10% of the population do not have adequate temporal insonation windows [10, 11]. Electroencephalography (EEG) is another commonly used noninvasive technique to probe the brain; it assesses electrophysiologic activity rather than hemodynamics. However, transcranial EEG has poor spatial resolution and is very sensitive to artifacts, which limits its use in the clinic [12]. Thus, there is currently a lack of non-invasive monitoring tools capable of providing real-time, reliable long-term information about the cerebral physiology at the bedside. This is specially lacking for applications in the field, such as during sports and in military fields.

More recently, diffuse optical spectroscopy (DOS) and diffuse correlation spectroscopy (DCS) have been proposed as noninvasive and continuous bedside monitors capable of providing neurophysiology information in neurocritical patients. By shining near-infrared light (650-900 nm) from the scalp, DCS can measure microvascular cerebral blood flow (CBF), and DOS can measure oxy- and deoxy-hemoglobin concentrations (HbO and HbR, respectively) [13–21]. In particular, the CBF measurements with DCS have been previously validated against several different gold standard CBF measures [17, 22–29]. In addition, the combination of CBF and oxygenation provides an estimate of the cerebral metabolic rate of oxygen (CMRO_2) [30, 31].

The combination of DOS and DCS has been explored to monitor patients in several clinical and pre-clinical scenarios. For example, diffuse optics have been shown to provide relevant clinical information for critically-ill neonates [32, 33], including during cardiac surgeries to treat heart defects [15, 34, 35]. Additionally, many authors have explored the use of diffuse optics to assess the cerebral hemodynamics during different cerebrovascular interventions, such as during carotid endarterectomy[1] [36–38], during thrombolytic treatments for stroke [39], during head-of-bed manipulations [40–42], during cardiopulmonary resuscitation [43], and others [44–46]. Diffuse optics have also been used to monitor cerebral auto-regulation[2], both in healthy and critically ill subjects [18, 25, 47], as well for assesssing the critical closing pressure of the cerebral circulation[3] [26]. Many authors

---

[1] Carotid endarterectomy is a surgery that may help to prevent stroke by removing the blockage form the carotid arteries.

[2] Cerebral auto-regulation is a neuro-mechanism that aims to maintain adequate and stable cerebral blood flow.

[3] Critical closing pressure is the internal pressure at which a blood vessel collapses and closes completely.

have also validated the optically-derived cerebral hemodynamic parameters for long-term monitoring of neurocritical patients [24, 47, 48], including for the prediction of hypoxic [49] and ischemic events [50]. However, the reliability of the technique to provide accurate *real-time* information during longitudinal measurement as well as during a few different clinical interventions remains largely unaddressed.

Relative to other approaches, the key advantage of diffuse optics is its ability to simultaneously measure blood flow and tissue blood oxygenation noninvasively (and continuously) at the bedside using portable instrumentation. Compared to TCD, DCS has an additional advantage: it measures tissue level perfusion, whereas TCD measures cerebral blood flow velocity in large arteries at the base of the brain. This distinction may be particularly important when evaluating steno-occlusive disease in which both proximal large artery flow and leptomeningeal collaterals contribute to perfusion. Optical techniques also have significant advantages when compared to other traditional imaging modalities, such as PET and MRI. In addition to providing both CBF and HbO/HbR concentration, optical monitoring provides significantly better temporal resolution than either MRI or PET, allowing for the assessment of dynamic cerebral autoregulation [18, 25, 51]. Importantly, the diffuse optical methods are also inexpensive and portable in comparison to PET and MRI which is a critical advantage given the high burden of vascular disease in lower- and middle-income countries. Additionally, diffuse optics do not require ionizing radiation and/or contrast agents, which is generally the case for PET and MRI.

The main goal of this thesis was to show that diffuse optics can aid in *real-time* monitoring of neurocritical patients with cerebrovascular diseases. To this end, we divided the remaining of the thesis in four different chapters corresponding to different studies. In Chapter 2, we review the fundamental aspects of diffuse optics, and highlight the main theoretical and experimental considerations required for conducting an experiment with diffuse optics. In Chapter 3, we report on the translation of a hybrid diffuse optical system to a neuro-intensive care unit of a public hospital in Brazil for real-time, long-term monitoring of neuro-critical patients. Then, in Chapter 4, we describe the application of diffuse optics for monitoring acute ischemic stroke patients undergoing an endovascular treatment. In Chapter 5, we analyze the advantages of implementing an improved data analysis algorithm that attempts to separate the extra-cerebral and cerebral contributions from the optical signal. Finally, in Chapter 6, we summarize the main conclusions of this thesis, as well as suggest potential directions for future studies in this field.

Chapter 2

Principles of Diffuse Optics

In a typical diffuse optical experiment, we shine near-infrared light from the scalp and collect the diffusively reflected photons a distance between 2.5 and 4 cm from the source (Figure 2.1). Due to diffusive nature of light propagation in human tissues, the measured photons will carry information about the surface of the cerebral tissues. More specifically, we can recover information about the microvascular cerebral blood flow (CBF) and cerebral oxygenation. In this Chapter, we will provide the fundamental concepts of diffuse optical methods. More specifically, Section 2.1 will provide the theoretical aspects of both diffuse optical spectroscopy (DOS) and diffuse correlation spectroscopy (DOS), and Section 2.2 will highlight the main experimental considerations for applications in humans, primarily for cerebral monitoring.

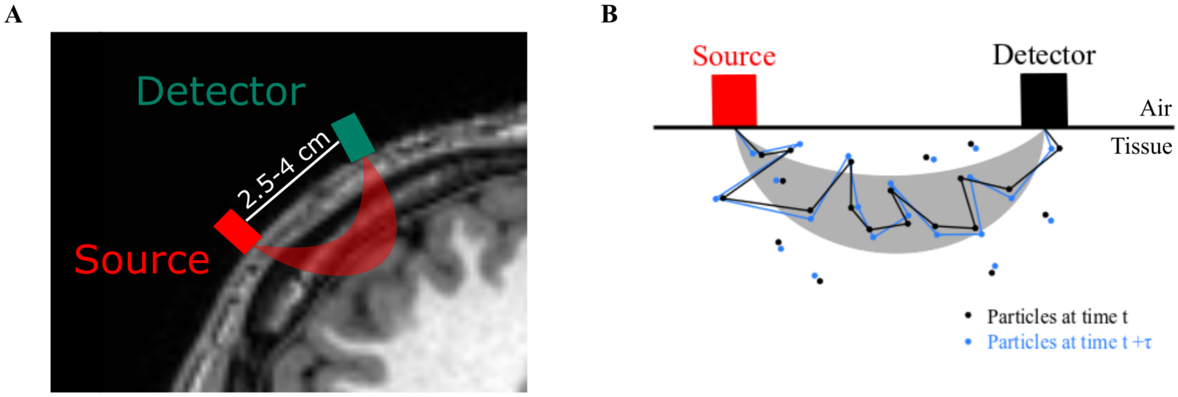

Figure 2.1: Pictorial representation of the average path of the detected photons for a typical diffuse optical experiments with source-detector separations between 2.5 and 4 cm, which is a generally a good compromise between a good SNR and brain sensitivity.

2.1 Theoretical aspects of diffuse optics

2.1.1 Diffuse Optical Spectroscopy

The problem of light transport inside turbid media can be modeled by the Radiative Transport Equation (RTE), or Boltzmann transport (ignoring polarization effects). The RTE is an approximation of Maxwell's equation, and can be written as [13, 52, 53]:

$$\frac{1}{v}\frac{\partial L(\vec{r},\hat{\Omega},t)}{\partial t}+\hat{\Omega}.\nabla L(\vec{r},\hat{\Omega},t)=Q(\vec{r},\hat{\Omega},t)+\mu_s\oint L(\vec{r},\hat{\Omega},t)f(\hat{\Omega},\hat{\Omega}')d\hat{\Omega}'-\mu_t L(\vec{r},\hat{\Omega},t), \quad (2.1)$$

where $L(\vec{r},\hat{\Omega},t)$ is the radiance, defined as the average power at position $\vec{r}$ and instant t across the area oriented in the direction of the unit vector $\hat{\Omega}$; v is the speed of light inside the medium; $\mu_t=\mu_a+\mu_s$ is the transport coefficient, whereas μ_a and μ_s are the absorption and scattering coefficients, respectively; $f(\hat{\Omega},\hat{\Omega}')$ represents the scattering phase function, i.e., the probability of a photon coming from the direction $\hat{\Omega}$ is scattered into $\hat{\Omega}'$, and; $Q(\vec{r},\hat{\Omega},t)$ is a source term. The RTE (Equation 2.1) is an energy conservation equation, i.e., any change in radiance at a specific region, $\vec{r}$, propagating in the direction $\hat{\Omega}$ at time t (left side of the equation) is equal to the input power from any sources (first term in the right side of Equation 2.1), plus the power scattered from all other directions into $\hat{\Omega}$ (second term of the right side of Equation 2.1) minus the power that is scattered to other directions and/or absorbed (third term of Equation 2.1).

To arrive at the RTE, a few assumptions are necessary: 1) intensity is transferred element-wise (based on the principle of energy conservation), and thus, on average, there is no interference of electric fields between different multiple scattering paths; 2) back-scattering is insignificant when compared to the scattering to other directions; 3) the scattering particles are non-interacting; 4) the incident source is perfectly monochromatic, and; 5) the scattering particles are sufficiently distant from each other (much greater than one wavelength), so that we can use a far-field approximation [54].

Analytic solutions to the RTE are only available for very simple and highly symmetric media. However, for highly scattering tissues, it is possible to derive a diffusion equation with a simple approximation of the RTE (Equation 2.1). By expanding $L(\vec{r},\hat{\Omega},t)$ in terms of the spherical harmonics, Y_ℓ^m, up to terms with $\ell=1$ (the P_1 approximation), we can write the radiance as [20, 21, 53, 55]:

$$L(\vec{r},\hat{\Omega},t)=\frac{1}{4\pi}\phi(\vec{r},t)+\frac{3}{4\pi}\vec{J}(\vec{r},t)\cdot\hat{\Omega}, \quad (2.2)$$

where $\phi(\vec{r},t)$ is the fluence rate and is defined as the integral of the radiance over all angles, and represents the number of photons per unit area per unit time, and $\vec{J}(\vec{r},t)\cdot\hat{\Omega}$ is the photon flux leaving position $\vec{r}$ in the direction $\hat{\Omega}$ at instant t. By substituting Equation 2.2 in Equation 2.1, we obtain the diffusion equation for the photon fluence [13, 20, 21, 53, 55]:

$$\vec{\nabla}\cdot[D(\vec{r},t)\nabla\phi(\vec{r},t)] - v\mu_a\phi(\vec{r},t) - \frac{\partial\phi(\vec{r},t)}{\partial t} = -vS(\vec{r},t), \tag{2.3}$$

where $S(\vec{r},t)$ is an isotropic source term, $D(\vec{r})$ is the diffusion coefficient, defined as $D(\vec{r}) = v/(3\mu_t'(\vec{r})) = v/(3(\mu_a(\vec{r})+\mu_s'(\vec{r})))$, and μ_s' is the reduced scattering coefficient. The reduced scattering coefficient, or random-walk coefficient, can be written as $\mu_s' = \mu_s(1-g)$, where $g = \langle\cos\theta\rangle$ is the anisotropy factor.

The validity of the diffusion equation rests on a few important assumptions [13, 20, 53]:

1. *The RTE is valid.* This is often the case for unpolarized light propagating in media with $\ell_a = 1/\mu_a$ and $\ell_s = 1/\mu_s$ much greater than the light wavelength, λ;
2. *Light radiance is nearly isotropic.* This is a requirement from the P_1 approximation (i.e., $\phi \gg |\vec{J}|$), and is usually valid for highly scattering media ($\mu_s' \gg \mu_a$);
3. *Rotational symmetry.* The diffusion equation assumes that μ_a, μ_s and f are independent of the propagation direction of the photons;
4. *Slow temporal variation in photon flux.* As discussed in [20], this is valid for $f \ll 32GHz$, where f is the modulation frequency of the input source;
5. *Light sources are isotropic.*

For biological tissues, all of these assumptions are generally valid in the near-infrared region ($\sim 650-900$ nm), where light is predominantly scattered (i.e., $\mu_s' \gg \mu_a$) [20, 53].

Most commonly, biological tissue is approximated by a semi-infinite medium (Figure 2.2), which is composed of a non-scattering (e.g., air) and a diffusive medium (e.g., a human head). Since there will be a refractive index mismatch between each medium, there will be Fresnel reflections at the boundary. The exact formalism to deal with the Fresnel reflection in a semi-infinite medium is the partial flux boundary condition [56]. However, the partial flux boundary condition involves integral terms that are too difficult for practical purposes. *Patterson et al.* and *Farrel et al.* have employed a more palatable boundary condition in which the fluence is set to zero at an extrapolated boundary located

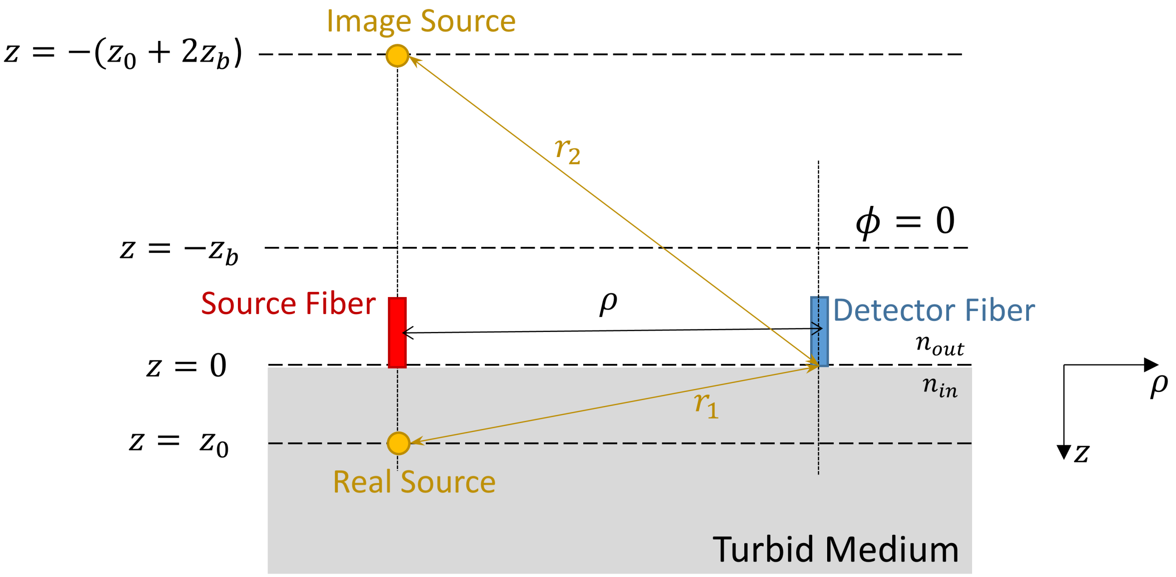

Figure 2.2: Representation of a semi-infinite medium in the extrapolated boundary condition. The semi-infinite medium is composed of a non-scattering (top layer) and a diffusive medium (bottom layer), with refractive indexes n_out and n_in, respectively. Here, we represent the extrapolated boundary condition in which the fluence (Φ) is set to zero at a distance z_b above the diffusive medium. We also represent the standard measurement procedure, where we add a source and a detector at medium boundary, separated by a distance ρ. In yellow, we represent the method of images used to solve the diffusion equation. This Figure was extracted from [21].

at a distance z_b, outside the diffusive medium (Figure 2.2) [57, 58]. The extrapolated zero distance, z_b, can written as [56]:

$$z_b = \frac{1 + R_{eff}}{1 - R_{eff}} \frac{2}{3} z_0. \tag{2.4}$$

Here, $z_0 = l'_t = 1/\mu'_t$ is the reduced mean transport length, where $\mu'_t = \mu_a + \mu'_s$ is the reduced mean transport coefficient. The effective Fresnel reflectivity (R_{eff}) can be approximated as:

$$R_{eff} \approx -1.44 \left(\frac{n_{in}}{n_{out}}\right)^{-2} + 0.701 \left(\frac{n_{in}}{n_{out}}\right)^{-1} + 0.064 \left(\frac{n_{in}}{n_{out}}\right) + 0.668, \tag{2.5}$$

where n_{in} and n_{out} are the index of refraction of the diffusive and non-scattering media, respectively (Figure 2.2). Note that the extrapolated zero boundary condition is an approximation of the exact partial flux boundary condition.

To solve Equation 2.3 for a semi-infinite medium with the extrapolated zero boundary condition, we can use the method of images by adding one imaginary (negative) source in the non-scattering medium, as seen in Figure 2.2. Here, the real source was placed inside the medium at a depth $z = z_0$, which is the average distance in which the direction of the photon propagation is randomized (or the mean random walk distance). By assuming the source is positioned at z_0, we can consider the source to be approximately isotropic. This approximation is valid (less than 5% error) for large source-detector separations ($\rho \gg 10/(\mu_a + \mu_s'))$ [53, 56, 58].

In practical applications of diffuse optics, there are three main types of sources commonly employed: continuous-wave (CW), intensity-modulated (or frequency-domain, FD) and time-pulsed (or time-domain, TD). Each type of source requires a different solution to Equation 2.3, using the appropriate domain. When working with time-pulsed sources, we can solve Equation 2.3 in the time-domain with the extrapolated boundary condition by assuming a unitary input source term $S(\vec{r}, t) = \delta(t - t_0)\delta(\vec{r} - \vec{r_0})$ (i.e., using Green's method). In this regime, we can show that the fluence measured at the medium boundary a distance ρ from the source is [13, 20, 59]:

$$\begin{aligned} \textit{TD Solution: } \phi_G(\vec{r}, t) = \frac{v \exp\left[-v\mu_a(t - t_0)\right]}{(4\pi D(t - t_0))^{3/2}} \Bigg(& \exp\left[-\frac{r_1^2}{4D(t - t_0)}\right] - \\ & \exp\left[-\frac{r_2^2}{4D(t - t_0)}\right]\Bigg), \end{aligned} \tag{2.6}$$

where $r_1 = \sqrt{(z - z_0)^2 + \rho^2}$, $r_2 = \sqrt{(z + 2z_b + z_0)^2 + \rho^2}$, v is the speed of light in the medium, t_0 is the injection time of photons, and D is the diffusion coefficient (from Equation 2.3).

If instead of a time-pulsed laser, we have an intensity modulated source at an angular frequency $\omega = 2\pi f$, we can set $S(\vec{r}, t) = \delta(\omega)\delta(\vec{r} - \vec{r_0})$ and take a Fourier transform of Equation 2.3 to arrive at the frequency-domain (FD) diffusion equation:

$$(\nabla^2 - K_0^2)\phi_G(\vec{r}, \omega) = \delta(\vec{r} - \vec{r_0})\delta(\omega). \tag{2.7}$$

The general solution of Equation 2.7 is a spherical wave with wave vector $K_0^2 = (v\mu_a + i\omega)/D$. By solving Equation 2.7 for a semi-infinite medium with the extrapolated boundary condition, we can show that for an intensity-modulated source the fluence measured on the medium boundary a distance ρ from the point of illumination is:

$$\textit{FD Solution: } \phi_G(\vec{r}, \omega) = \frac{v}{4\pi D}\left(\frac{e^{-K_0 r_1}}{r_1} - \frac{e^{-K_0 r_2}}{r_2}\right), \tag{2.8}$$

where r_1 and r_2 were previously defined for the TD solution, and represent the distances of the real and imaginary sources with respect to the point of measurement, respectively

(Figure 2.2). By taking the $w \to 0$ limit in Equation 2.8, we arrive at the semi-infinite solution for a continuous-wave (CW) source:

$$\textit{CW Solution: } \phi_G(\vec{r}) = \frac{v}{4\pi D}\left(\frac{e^{-K_{CW}r_1}}{r_1} - \frac{e^{-K_{CW}r_2}}{r_2}\right), \tag{2.9}$$

where $K_{CW}^2 = K_0^2(\omega \to 0) = \mu_a/D$.

2.1.2 Diffuse Correlation Spectroscopy

In the previous section, we were only interested in the slow changes in the optical properties of the medium and we ignored the movement of the scattering particles. To account for the mean squared displacement of the scattering particles ($\langle \Delta r^2 \rangle$), we can derive a Correlation Transport Equation (CTE) by introducing small changes to the RTE (Equation 2.1). First, recall that that the radiance, $L(\vec{r}, \widehat{\Omega}, t)$, is the average intensity and can be written as:

$$L(\vec{r}, \widehat{\Omega}, t) = \langle I(\vec{r}, \widehat{\Omega}, t) \rangle \propto \langle \vec{E}(\vec{r}, \widehat{\Omega}, t)\vec{E}^*(\vec{r}, \widehat{\Omega}, t) \rangle, \tag{2.10}$$

where $\langle \rangle$ is an ensemble average, and $I(\vec{r}, \widehat{\Omega}, t)$ and $\vec{E}(\vec{r}, \widehat{\Omega}, t)$ are respectively the intensity and total electric field at point $\vec{r}$ and time t propagating in the $\widehat{\Omega}$ direction. Interestingly, the time-dependent electric-field correlation function ($G_1(\vec{r}, \widehat{\Omega}, t, \tau)$) is defined in a similar form:

$$G_1(\vec{r}, \widehat{\Omega}, t, \tau) = \langle \vec{E}(\vec{r}, \widehat{\Omega}, t)\vec{E}^*(\vec{r}, \widehat{\Omega}, t + \tau) \rangle. \tag{2.11}$$

Since the time-dependent electric field correlation function is proportional to the radiance at zero delay times (i.e., $G_1(\vec{r}, t, \widehat{\Omega}, \tau = 0) \propto L(\vec{r}, \widehat{\Omega}, t)$), it is reasonable to expect that the CTE is identical to the RTE at zero delay times ($\tau = 0$). In previous studies, *Ackerson et al.* and *Dougherty et al.* have shown that the CTE can be written as [54, 60]:

$$\begin{aligned}\frac{1}{v}\frac{\partial G_1(\vec{r}, \widehat{\Omega}, t, \tau)}{\partial t} + \widehat{\Omega}.\nabla G_1(\vec{r}, \widehat{\Omega}, t, \tau) =& Q(\vec{r}, \widehat{\Omega}, t) \\ &+\mu_s \oint G_1(\vec{r}, \widehat{\Omega}, t, \tau) g_1^s(\widehat{\Omega}, \widehat{\Omega}', \tau) f(\widehat{\Omega}, \widehat{\Omega}') d\widehat{\Omega}' \\ &-\mu_t G_1(\vec{r}, \widehat{\Omega}, t, \tau),\end{aligned} \tag{2.12}$$

where $\mu_t = \mu_a + \mu_s$ is the transport coefficient and $f(\widehat{\Omega}, \widehat{\Omega}')$ is the scattering phase function from Equation 2.1. The single-scattering auto-correlation function, $g_1^s(\widehat{\Omega}, \widehat{\Omega}', \tau)$, can be written as [21, 54, 55, 60]:

$$g_1^s(\tau) = \exp\left[-\frac{1}{6}q^2\langle\Delta r^2(\tau)\rangle\right], \tag{2.13}$$

where $\langle\Delta r^2(\tau)\rangle$ is the mean square displacement of the scattering particles; $\vec{q} = \vec{k}_{out} - \vec{k}_{in}$ is the momentum transfer, with amplitude $q = 2k_0 \sin(\theta/2)$; $\vec{k}_{in}$ and $\vec{k}_{out}$ are the incident and scattered wave vectors, where $k_{in} = k_{out} = k_0 = 2\pi n/\lambda$. When comparing Equations 2.1 and 2.12, it is clear that in the $\tau \to 0$ limit, the CTE reduces to the RTE, as expected.

In the derivation of the CTE, apart from the necessary assumptions from the RTE (refer to Section 2.1.1), it is also assumed that the scattering particles are sufficiently separated, such that each scattering event can be considered independent. Additionally, in the CTE (Equation 2.12) it is also implicitly assumed that the speed of the scattering particles is much slower than the speed of light, and thus the correlation can be considered as instantaneous. Note that the CTE can be derived from a perturbative solution to Maxwell's equation [54].

The main difference between the CTE and the RTE comes from the second term on the right side of Equation 2.12, which describes the amount of radiance, or correlation, scattered into $\widehat{\Omega}$ from all other directions. In the RTE, energy is conserved and each scattering event does not alter the radiance, but correlation is not conserved in the CTE. After each scattering event, the amount of correlation transferred depends upon the single scattering correlation function, $g_1^s(\tau)$, which decreases with increasing delay times. Thus, correlation is transferred less and less into the $\widehat{\Omega}$ direction as τ increases.

Since the RTE and the CTE are formally similar, it is also possible to arrive at a diffusion equation for the field auto-correlation function using the P_1 approximation (refer to Appendix A.2 of [55]). Focusing on the continuous wave (CW) case, we can arrive at:

$$v\left(\mu_a + \frac{1}{3}\mu_s'\kappa_0^2\langle\Delta r^2(\tau)\rangle\right)G_1(\vec{r},\tau) - \nabla\cdot\left[D(\vec{r})\nabla\left(G_1(\vec{r},\tau)\right)\right] = vS(\vec{r}), \tag{2.14}$$

where v is the speed of light in the medium; μ_a and μ_s' are the absorption and reduced scattering coefficients; $\kappa_0 = 2\pi/\lambda$ is the incident wave vector; $D(\vec{r}) = v/(3\mu_t')$ is the photon diffusion coefficient, and; $\langle\Delta r^2(\tau)\rangle$ is the mean square displacement of the scattering particles. In the derivation of Equation 2.14, it is assumed that the scattering phase function $(f(\widehat{\Omega},\widehat{\Omega}'))$ and the single scattering auto-correlation function $(g_1(\widehat{\Omega},\widehat{\Omega}',\tau))$ only depends on the scattering angle $(\widehat{\Omega}\cdot\widehat{\Omega}')$ and that $k_0^2\langle\Delta r^2(\tau)\rangle \ll 1$.

For homogeneous media, i.e., media where μ_a, μ_s' and $\langle\Delta r^2(\tau)\rangle$ are position independent, we can recast Equation 2.14 as a Helmholtz equation for the field auto-correlation function:

$$\left(\nabla^2 - K^2(\tau)\right) G_1(\vec{r},\tau) = -\frac{vS}{D}\delta^3(\vec{r}-\vec{r}_0), \tag{2.15}$$

where $K^2(\tau) = v\left(\mu_a + \frac{1}{3}\mu_s' k_0^2 \langle \Delta r^2(\tau)\rangle\right)/D$. In Equation 2.15 we additionally assumed a point-like source term, located at $\vec{r}_0$. Since Equation 2.15 is formally identical to Equation 2.7, we can solve the correlation diffusion equation for a semi-infinite medium using the same methods from Section 2.1.1, but with a different wave-vector ($K_0(\omega) \rightarrow K(\tau)$):

$$\textit{DCS Solution: } G_1(\vec{r},\tau) = \frac{v}{4\pi D}\left[\frac{e^{-K(\tau)r_1}}{r_1} - \frac{e^{-K(\tau)r_2}}{r_2}\right]. \tag{2.16}$$

Note that $G_1(\vec{r},\tau)$ depends on μ_a and μ_s', in addition to $\langle \Delta r^2(\tau)\rangle$.

2.2 Experimental methods of diffuse optics

In this section, we highlight the main experimental considerations necessary to conduct a diffuse optical measurement. We first briefly overview a few important considerations required for applications in human tissues, which is the main goal of this thesis, and then describe the instrumentation as well as the fitting steps for each type of source. In Section 2.2.1, we describe the experimental methods for the three types of sources employed in DOS measurements, and in Section 2.2.2, we describe the experimental methods for DOS experiments.

2.2.1 Diffuse Optical Spectroscopy

Although theoretically similar, there are distinct experimental and theoretical considerations for each type of source commonly employed for DOS measurements. Depending on the source type, we will have access to different features of the scattered light: with CW sources, we can only recover the *changes* in light intensity; with frequency-modulated sources (FD), we can recover the amplitude *changes* and phase shifts, and; with pulsed sources (TD), we can recover the distribution of time of flights of the diffusively scattered photons (Figure 2.3). In Section 2.2.1.1, we describe a few important considerations necessary for human applications, and then in Sections 2.2.1.2 - 2.2.1.4, we briefly describe the most important experimental considerations for each type of source.

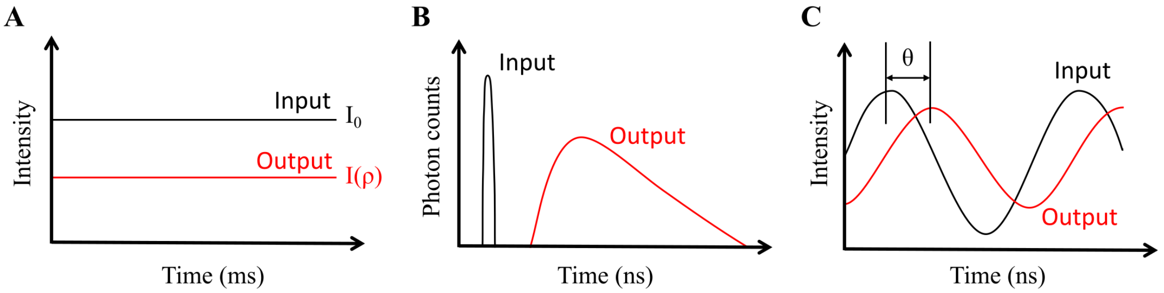

Figure 2.3: Representative signals from the three different DOS techniques. (A) Continuous wave (B) Time-Domain (C) Frequency-Domain. Modified from [21].

2.2.1.1 Considerations for human applications

In the near-infrared range (NIR, 600-900 nm), there is a biological window with low absorption but high scattering where the diffusive approximation is valid. For human tissue, the main absorbers in the NIR are the oxy- and deoxy-hemoglobin (HbO and HbR, respectively) and water (Figure 2.4). Of importance, melanin also absorbs light in the NIR, but it is possible to ignore its contribution since melanin is restricted to a very thin upper layer of the tissue. Finally, we can write the absorption coefficient as a linear mixture of the contribution from each chromophore:

$$\mu_a(\lambda) = \sum \varepsilon_i(\lambda) c_i = \varepsilon_{HbO}(\lambda) HbO + \varepsilon_{HbR}(\lambda) HbR + \mu_{a,H_2O}(\lambda) f_{H_2O}, \tag{2.17}$$

where $\varepsilon_i(\lambda)$ and c_i are the extinction coefficient and the concentration of the ith chromophore, respectively, μ_{a,H_2O} is the water absorption coefficient and f_{H_2O} is the water fraction in tissue. Additionally, for human measurements, we expect a Mie-type scattering, and thus we can write the reduced scattering coefficient as [61, 62]:

$$\mu_s' = A \left(\frac{\lambda}{800} \right)^{-b}, \tag{2.18}$$

where A and b are related to the size, index of refraction, and the concentration of scatterers in tissue, and λ is given in nm.

By measuring the oxy- and deoxy-hemoglobin concentrations, it is useful to compute the total hemoglobin concentration (HbT = HbO + HbR), which is proportional to the tissue blood volume. Additionally, we can also estimate the tissue oxygen saturation ($\mathrm{StO_2}$ = HbO / HbT), as well as the oxygen extraction fraction (OEF). The OEF can be estimated with [30, 31]:

$$OEF = \frac{1}{\gamma} \frac{SaO_2 - StO_2}{SaO_2}, \tag{2.19}$$

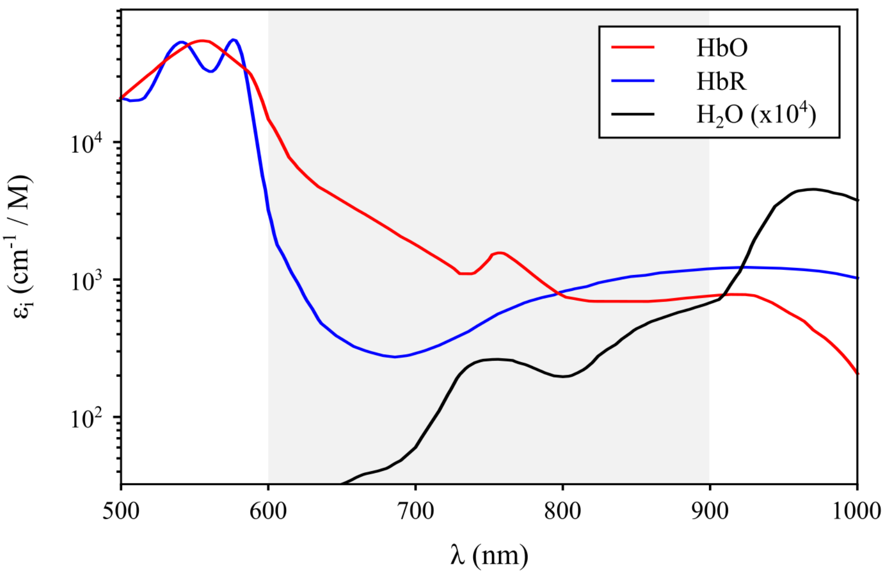

Figure 2.4: Extinction coefficients of the main components of human tissue. In general, the main absorbing particles in human tissue are the oxy- (HbO, red line) and deoxy-hemoglobin (HbR, blue line), as well as water (H_2O, black line).

where SaO_2 is the arterial blood oxygen saturation, and γ is the percentage of blood volume contained in the venous compartment of the vascular system, usually assumed to be 0.75 [63].

In general, to accurately recover the concentration of N chromophores, we need measurements with at least $M \geq N$ different wavelengths to solve a well-posed $M \times N$ system of equations (from Equation 2.17). For DOS applications in humans, a minimum of two wavelengths is necessary as we are only interested in the HbO and HbR concentrations, since we can assume a constant water fraction in tissue ($f_{H2O} \approx 75\%$). *Corlu et al.* developed a formalism to define the optimal wavelengths to maximize the accuracy in the recovery of the concentration of the different chromophores [61, 64]. For example, to maximize the accuracy of the recovery of HbO and HbR, while assuming constant A and b, they proposed that for a set of three wavelengths, the optimum choices are: (650 ± 2) nm, (716 ± 4) nm, and (902 ± 16) nm. It is worth noting that by employing more wavelengths we can increase the accuracy in the recovery of the chromophore concentrations, but this will also increase the cost and complexity of the instrument.

2.2.1.2 Continuous-Wave Diffuse Optical Spectroscopy

The simplest approach for DOS measurements is the use of CW sources. In this approach, we only have access to *changes* in light intensity (Figure 2.3-A) at each wavelength. Theoretically, CW-DOS (commonly referred in the literature as near-infrared spectroscopy, NIRS) is only sensitive to an effective transport coefficient, defined as $\mu_{eff} = K_0(\omega \to 0) = \sqrt{3\mu_a\left(\mu_a + \mu_s'\right)}$, and it is unable to uniquely separate the effects of absorption and scattering in homogeneous tissues [64, 65]. To overcome this issue, most studies use a Modified Beer-Lambert Law (MBLL) formalism that relates changes in the optical density (OD) to changes in absorption [66, 67]. The OD is defined as:

$$OD(t, \lambda) \equiv -\log \frac{I(t, \lambda)}{I_0(t, \lambda)} = \mu_a(t, \lambda)L, \tag{2.20}$$

where I and I_0 are respectively the detected and incident light intensities, and L is the linear photon pathlength inside the medium.

To arrive at the MBLL, we assume that after some time there will be absorption changes ($\mu_a \Rightarrow \mu_a + \Delta\mu_a$) but the scattering will remain constant ($\Delta\mu_s' = 0$). With this assumption, we can write the changes in optical density (ΔOD) due to changes in absorption as:

$$\begin{aligned} \Delta OD(t, \lambda) = OD(t, \mu_a + \Delta\mu_a, \mu_s') - OD(t_0, \mu_a, \mu_s') = \\ \cancel{OD(t, \mu_a, \mu_s')} + \frac{\partial OD(t, \mu_a, \mu_s')}{\partial \mu_a}\Delta\mu_a + \cancelto{0}{\mathcal{O}(2)} - \cancel{OD(t_0, \mu_a, \mu_s')}, \end{aligned} \tag{2.21}$$

where we expanded OD$(t, \mu_a + \Delta\mu_a, \mu_s')$ in terms of the variation in the absorption coefficient ($\Delta\mu_a$). By neglecting the higher order terms and using Equation 2.20, we arrive at the MBLL [66]:

$$\Delta OD(t, \lambda) = -\ln\left(\frac{I(t, \lambda)}{I(t_0, \lambda)}\right) = \underbrace{\frac{\partial OD(t, \mu_a, \mu_s')}{\partial \mu_a}}_{l_{DPF}} \Delta\mu_a(t, \lambda), \tag{2.22}$$

where t_0 is a baseline period and l_{DPF} is the photon's differential pathlength, and is roughly a correction to the non-linearity of the photon paths due to scattering. With Equation 2.22, it is possible to measure absorption changes ($\Delta\mu_a$) without directly measuring μ_a and μ_s'. By measuring changes in the absorption coefficient, we can also measure changes in the chromophore concentrations:

$$\begin{aligned} -\frac{1}{l_{DPF}}\Delta OD(t, \lambda) = \Delta\mu_a(t, \lambda) = \sum \varepsilon_i(t, \lambda)\Delta c_i = \\ \varepsilon_{HbO}(t, \lambda)\Delta[HbO] + \varepsilon_{HbR}(t, \lambda)\Delta[HbR], \end{aligned} \tag{2.23}$$

where we considered a constant water fraction.

Currently, there are several commercially available CW-DOS instruments [67], ranging from few thousand dollars to several hundred thousand dollars. A typical NIRS instrument is relatively simple, as we only need to measure changes in light-intensity. Most systems employ either laser-diodes or LEDs as sources. In general, laser-diodes provide higher power, have a narrower spectrum ($<$1 nm) and are easier to collimate into fiber-optics. However, laser-diodes are generally more expensive and often come in bulky packaging due to cooling and power requirements. On the other hand, although LEDs have a broader emission spectrum ($\sim$ 30 nm), they can be applied directly on the body surface without need for optical fibers, and they are relatively inexpensive and do not require sophisticated cooling and power supplies.

To detect the *changes* in light intensity, CW-DOS instruments usually employ either photodiodes or avalanche photodiodes (APD). Photodiodes have a large dynamic range ($<$100 dB) and are easy to use. However, photodiodes usually require low-noise pre-amplifiers, as they have lower internal gains. On the other hand, APDs have higher internal gains and are more sensitive to light-intensity changes, while still having a reasonable dynamic range ($<$60 dB). However, since the operating voltage of an APD is in the order of tens to hundreds of volts, it is hard to safely place the APDs directly on the body surface, and thus they usually require coupling to fiber-optics. Due to the dependency of the internal gain on temperature and bias voltage, APDs also require stabilized power supplies and often need cooling.

Since CW-DOS instrumentation is relatively simple and inexpensive, it is possible to combine several sources and detectors in a single, relatively small instrument without drastically increasing the cost. For example, with multiple source and detector pairs it is possible to cover a wide area on the head, even allowing whole-head measurements [68–73]. Additionally, with multiple source-detector pairs it is also possible to reconstruct images of brain activation, which have been validated against functional MRI [74]. Due to the low-cost of CW-DOS, some authors have even suggested wireless instrumentation, which allow measurements in natural environments, such as in parks and during physical activity [75–78].

The number of CW-DOS (or NIRS) studies exponentially increased over the last decade, with the majority of studies focusing in functional studies of the brain [19, 67, 79, 80]. Regarding clinical applications, CW-DOS is currently employed as a complementary physiological monitor in several clinical scenarios (e.g., cardiovascular surgeries) [46, 81–87]. However, since CW-DOS is only capable of measuring *changes* in oxygenation, it has been limited as trend monitors, therefore being susceptible to systemic physiological oscillations and diminishing its usefulness for longitudinal monitoring of neurocritical patients [88–93]. For more details about CW-DOS, we refer the reader to recent comprehensive reviews [19, 67, 80, 82].

2.2.1.3 Frequency-domain diffuse optical spectroscopy

By employing frequency-modulated sources and by measuring changes in the amplitude and phase of the scattered wave, we can measure the absolute optical properties of the tissue. In a typical FD-DOS experiment, we employ multiple source-detector separations to recover μ_a and μ_s' at multiple wavelengths [13, 53, 94, 95]. For this, a simplification of Equation 2.8 for large source-detector separations is often employed [21, 53]. If we assume that $\rho >> l_t + 2z_b$, we obtain:

$$\phi_G(\vec{r},\vec{r_0},\omega) = \underbrace{\frac{v}{4\pi D}\frac{e^{-K_{0,Re}\rho}}{\rho^2}\left[2K_0(z_b l_t + z_b^2)\right]}_{A(\rho)} e^{\overbrace{-iK_{0,Im}\rho}^{\theta(\rho)}}, \tag{2.24}$$

where $K_{0,Re}$ and $K_{0,Im}$ are respectively the real and imaginary parts of the wave vector K_0. From Equation 2.24, we can see that the phase ($\theta(\rho)$) and the logarithm of the amplitude times ρ^2 ($\ln\left(A(\rho)\rho^2\right)$) are linearly dependent on the source-detector separation (ρ):

$$\ln\left(\rho^2 A(\rho)\right) = -K_{0,Re}\rho + \ln A_0 \tag{2.25a}$$

$$\theta(\rho) = -iK_{0,Im}\rho + \theta_0. \tag{2.25b}$$

Thus, with a simple linear fitting procedure we can recover $K_{0,Re}$ and $K_{0,Im}$, from which we can compute the absorption and scattering coefficients with:

$$K_0^2 = \frac{v\mu_a + i\omega}{D} \Rightarrow \begin{cases} \mu_a = \frac{\omega\left(-K_{0,Re}^2 + k_{Im}^2\right)}{2vK_{0,Re}K_{0,Im}} \\ \mu_s' = -v\frac{2K_{0,Re}K_{0,Im}}{3\omega} \end{cases}. \tag{2.26}$$

Note that instead of using the approximation for large source-detector, it is also possible to recover the optical coefficients with a non-linear fit using Equation 2.8.

Although most FD-DOS instruments use a single modulation frequency and multiple source-detector separations to recover the optical properties, the requirement for multiple sources and detectors increases the complexity of the measurement as well as the cost of the instrument. The use of several source-detector separations requires multiple optical fibers to be attached to the head, and thus a careful calibration of the coupling coefficient for each separation is necessary, which may introduce additional errors in the retrieval of the optical properties. It is possible to estimate the coupling coefficient for each source-detector separation by measuring a phantom with known optical properties. However, there may be differences in contact between the calibration measurement on the phantom and the actual experiment. Furthermore, since each source-detector separation will probe slightly different regions, the presence of heterogeneities may also reduce the reliability of the optical properties retrieval.

To use a single source-detector separation to retrieve absolute values of μ_a and μ_s', we can vary the modulation frequency, typically between 100 and 700 MHz. By using a single source-detector separation, we will reduce the system cost, as it will require a single PMT and a single laser-diode. Until recently, multi-frequency instruments were restricted to bench-top as they usually required expensive bulky network analyzers. However, *Torjesen et al.* recently proposed an inexpensive system that fully integrates digital signal synthesis and detection to rapidly acquire the amplitude and phase shifts for multiple wavelengths, with frequency sweeps between 50 and 400 MHz, at a repetition rates up to 97 Hz [96]. The biggest disadvantage of multi-frequency measurements is the need for non-linear methods to retrieve the optical properties. However, since we are measuring with a single source-detector separation, we will be less sensitive to heterogeneities as the probed region across each modulation frequency will be more confined than the region probe by multiple source-detector separations.

The biggest advantage of FD-DOS over CW-DOS is the ability to measure phase shifts. In addition to allowing the absolute estimations of the optical coefficients, phase measurements are also more biased toward longer-photon paths [97]; photons with longer paths are likely to undergo more scattering events and thus have larger phase shifts. This is especially relevant for cerebral measurements, where we are mostly interested in changes in the cerebral tissues, which are approximately 1.2cm below the scalp. As an example, a recent study showed that it is possible to improve the depth accuracy of diffuse optical tomography (DOT) by using the phase information from FD instruments [97].

Most FD-DOS instruments use laser diodes modulated with an oscillating driving current. Due to their relatively fast time responses, it is possible to modulate laser-diodes at frequencies up to the gigahertz range [53]. The most common optical detectors employed in FD-DOS instruments are photomultiplier tubes (PMT) and APDs, but some instruments also employ CCD cameras in conjunction with a gated image intensifier [53, 96, 98–103]. For a detailed review about the instrumentation of FD-DOS, we refer the reader to [53].

2.2.1.4 Time-domain diffuse optical spectroscopy

In TD-DOS experiments, we measure the absorption and scattering coefficients of the tissue by shining a pulsed source to the tissue and by measuring the photon distribution of time-of-flight (DTOF) a distance ρ away from the source [13, 59, 104]. The DTOF is a histogram of the number of photons striking the detector as function of the time difference between the source trigger and the photon detection at time t. Due to light propagation through the tissue, the light pulse will be delayed, broadened and attenuated due to absorption and scattering. More specifically, broadening occurs due to the different photon pathlengths due to scattering, while attenuation occurs due to absorption and scattering to other directions. By increasing the scattering coefficient, we increase the delay and broadening of the pulse, and an increase in absorption affects the slope of the tail of the DTOF.

It is worth noting that there are other factors that introduce delays, broadening and attenuation of the light pulse, such as the source-detector separation and the delivery and collection optics. An increase in the source–detector distance yields an increased delay and broadening of the DTOF and decreases the number of detected photons, similarly to an increase in scattering. However, differently from CW-DOS and FD-DOS, the depth-sensitivity of TD-DOS is not directly related to the source-detector separation. Instead, since TD-DOS measures the arrival time of each photon, it is possible to discriminate between the early (superficial) and late (deep) arriving photons [105, 106]. Thus, it is possible to selectively analyze the late arriving photons, which are shown to be more sensitive to deeper tissues, such as the cortex.

Since the lasers and detectors employed in TD-DOS experiments are generally bulkier and require dangerous voltages, most studies employ fiber optics to deliver and collect light from the tissue. However, modal dispersion in the fiber optics will further broaden the light pulse. Modal dispersion can be greatly reduced by a proper design of the refraction index profile of the optical fibers. For example, graded-index fibers have negligible temporal dispersion ($<$1 ps/m), but have lower core diameter ($<$200 μm) and numerical aperture (NA, $<$0.3). Although graded-index fibers are often employed to deliver light to the tissue, they are not suitable to collect light from the tissue. The detected intensity in TD-DOS experiments is usually very small, and thus step-index optical fibers with high NA ($<$0.6) and large diameters (up to 3 mm) are usually required. However, step-index fibers have higher temporal dispersion ($<$100 ps/m), and thus care must be taken with the length of the detection fibers. We note that the attenuation of both graded-index and step-index fibers is negligible for TD-DOS experiments, which are generally limited to optical fibers with less than 10 meters.

Typically, in TD-DOS experiments we measure the DTOF at a single source-detector separation but with multiple wavelengths. Most studies use either non-linear fitting algorithms [13, 59, 107–109] or semi-empirical methods [110–113] to recover the optical properties. Regardless of the analysis algorithm employed, to accurately recover the optical properties of the tissue we need to account for the additional time-delay and broadening caused by the detector and pulse-width of the source. To that end, we can measure the instrument response function (IRF) by directly coupling the light-source and the detector [114]. For example, for non-linear fitting algorithms, we can account for the IRF by convolving the theoretical fluence from Equation 2.6 with the measured IRF. Note that the use of longer optical fibers and poor selection of the temporal resolution of the detector and source may lead to an unacceptable width of the IRF; IRFs with a full width at half maximum (FWHM) larger than 1 ns compromise the accuracy of TD-DOS measurements [115].

To reduce the FWHM of the IRF, care must be taken when designing TD-DOS instruments to choose laser sources and detectors with good temporal resolutions. Most TD-DOS instruments reported in the literature use laser diodes, which have high repetition rates (up to 100 MHz), relatively short pulses (100-200ps) and reasonable output power (1mW-1W). However, it is important to mention that increasing the power of laser-diodes generally will also broaden the pulse, which may be detrimental for applications with poor SNR. Besides good temporal resolution, the biggest advantage of laser-diodes is that they are relatively compact and they are currently commercially available at multiple vendors. More recently, some authors employed supercontinuum lasers for TD-DOS measurements, which have pulses shorter than $<$10 ps, and repetition rates of tens of megahertz. The biggest advantage of supercontinuum lasers is their high spectral brightness ($\sim$ 1mW/nm) and the possibility to automatically select the wavelength and power, with the proper optoelectronic accessories [23, 50, 116, 117]. Note that supercontinuum lasers are also relatively compact and suitable for portable systems.

To detect the weak light signals from TD-DOS, we need detectors with good temporal resolution (in the range of 1-250 ps), and sufficient sensitivity. Among the available options, PMTs and hybrid-PMTs [118] are the most commonly employed due to their fast response and large active area. Single-photon avalanche diodes (SPAD) have potentially faster temporal responses and higher sensitivity than PMTs, but SPAD generally have worse SNR due to their smaller active area when compared to PMTs. Finally, to detect the voltage pulses from the detector, most studies use the time-correlated single-photon counting (TCSPC) technique. Briefly, in TCSPC experiments each voltage pulse from the detector is time-stamped with the arrival time of the photon based on a synchronization signal. This time-stamp can then be used to build up the DTOF after multiple cycles. For an in-depth review of the TCSPC technique (including applications to TD-DOS), we refer the reader to [118].

The biggest disadvantage when working with TCSPC is that we are unable to process more than $\sim 10^6$ photon counts per second. This limits our ability to measure the later arriving photons, as the majority of the photons will be on the earlier portions of the DTOF. Additionally, to measure multiple wavelengths, we need to either compute the DTOF in parallel using different timing electronics (increasing the cost of the instrument) or we need to share the maximum count-rate between each wavelength, further decreasing our sensitivity to the later photons. To overcome the issue of maximum photon counts, some authors have suggested the use of time-gating techniques to selectively measure the late arriving photons [59, 104, 110, 119–122]. Time-to-digital converters that allow higher maximum counting rates were also proposed [59, 104, 123, 124].

For a more detailed review about TD-DOS and its instrumentation, as well as for future prospects of the technique, we refer the reader to [59, 104].

2.2.2 Diffuse Correlation Spectroscopy

2.2.2.1 Considerations for human applications

In Section 2.1.2, we developed a formalism to measure the mean square displacement of the moving scattering particles from the auto-correlation function of the electric field. However, there are two main issues with that formalism: 1) experimentally, we only have access to the intensity auto-correlation function ($g_2(\tau) = \langle I(t)I(t+\tau)\rangle / \langle I(t)\rangle^2$), and; 2) there may be static (or slowly moving) scattering particles mixed with the fast moving particles.

Since experimentally we only have access to the intensity auto-correlation function

$g_2(\tau)$, we must use Siegert's Relation [125]:

$$g_2(\tau) = 1 + \beta |g_1(\tau)|^2, \tag{2.27}$$

where $g_2(\tau) = G_2(\tau)/\langle I(0)\rangle^2$ and $g_1(\tau) = G_1(\tau)/\langle I(0)\rangle$ are the normalized intensity and field auto-correlation functions, respectively, and; β is an experimental parameter that depends on the source and the collection optics. For example, when using single-mode fibers and non-polarized light, we expect $\beta = 0.5$. In general, we expect $\beta \approx 1/N$, where N is the number of modes allowed to propagate in the detection fiber, which is related to the fiber core diameter [20, 21, 125].

Before applying Equation 2.15 to biological tissues, one extra modification must be made to account for the static scatterers, as they do not contribute to the loss of correlation. To this end, we need to take into account the probability that a photon will be scattered by a moving particle. In human measurements, the main moving scatterer measured by DCS are the red blood cells (RBC), and we can define the probability of scattering by a RBC, α, as:

$$\alpha = f_{blood} \frac{\mu'_{s,blood}}{\mu'_{s,avg}} = f_{blood} \frac{\mu'_{s,blood}}{f_{blood}\mu'_{s,blood} + (1 - f_{blood})\mu'_{s,tissue}}, \tag{2.28}$$

where f_{blood} is the volume fraction of blood, $\mu'_{s,blood}$ is the scattering coefficient of blood and $\mu'_{s,avg} = f_{blood}\mu'_{s,blood} + (1 - f_{blood})\mu'_{s,tissue}$ is the volume fraction weighted average scattering coefficient of tissue and blood. Note that with DOS we are only directly sensitive to $\mu'_{s,avg}$. Finally, to account for the static scatterers, we can change the wave vector $(K(\tau))$ from Equation 2.15, so that:

$$K^2(\tau) = v \left(\mu_a + \frac{1}{3}\mu'_s k_0^2 \alpha \langle \Delta r^2(\tau) \rangle \right) / D. \tag{2.29}$$

The mean square displacement of the RBCs is generally given as:

$$\langle \Delta r^2(\tau) \rangle = 6 D_B \tau + v_{RBC}^2 \tau^2, \tag{2.30}$$

where τ is the delay time, D_B is a diffusion coefficient, and v_{RBC} is the speed of the RBCs [13, 126]. Experimentally, it was found that the shear-induced diffusive motion of the RBCs dominate the correlation decay [126, 127]. Thus, we can ignore the v_{RBC} term, and we can define a blood flow index as: BFI $= \alpha D_B$. Using Monte-Carlo simulations, Boas et al. showed that the BFI measured with DCS is indeed a measure of blood flow, as expected from the previous validation studies. More specifically, they showed that the

BFI measured by DCS is directly proportional to the absolute tissue blood flow (BF_{abs}), and their relation can be written as:

$$BFI = \frac{8\alpha_{shear}}{3} \frac{\mu'_{s,blood}}{\mu'_{s,avg}} \frac{1}{R} BF_{abs}, \tag{2.31}$$

where α_{shear} is the shear rate, and R is the average vessel radius in the probed region. Of importance, both the shear rate and the scattering coefficient of blood (α_{shear} and $\mu'_{s,blood}$, respectively) depend on the hematocrit (i.e., the volume ratio of the RBCs in blood). Thus, to convert BFI to BF_{abs}, a blood sample to measure the hematocrit, or a direct measure of both α_{shear} and $\mu'_{s,blood}$ may be necessary. Additionally, it is worth noting that to compute BFI we need knowledge of the average absorption and scattering coefficients of the tissue ($\mu_{a,avg}$ and $\mu'_{s,avg}$), which is possible with DOS. Thus, concurrent measurements of DOS and DCS are necessary to improve the reliability of the DCS measure of blood flow.

2.2.2.2 Instrumentation considerations

The signal-to-noise ratio (SNR) of a DCS measurement can be estimated as [20, 128, 129]:

$$SNR(\tau) = \frac{g_2(\tau) - 1}{\sigma_{g_2 - 1}} \approx \langle I_d \rangle \beta \sqrt{t_{avg}} \frac{\sqrt{T} \exp\left(-2\Gamma\tau\right)}{\sqrt{1 + \beta \exp\left(-\Gamma\tau\right)}}, \tag{2.32}$$

where $\langle I_d \rangle$ is the average intensity measured at the detector, T is the correlator delay-time bin width, t_{avg} is average time for the computation of the auto-correlation curves and Γ is the decay rate of the reduced normalized intensity auto-correlation function ($g_2 - 1$). For a SI medium, we can approximate Γ as:

$$\Gamma(\tau) \approx \sqrt{3\mu_a \mu'_s} \left(\frac{2\pi n_0}{\lambda}\right)^2 \times \frac{\mu'_s D_B}{\mu_a} \sqrt{\left(\frac{1}{\mu'_s}\right)^2 + \rho^2}. \tag{2.33}$$

From Equation 2.32, we can see that the SNR of a DCS measurement is primarily affected by the detected intensity ($\langle I_d \rangle$), the β factor from Sierget's relation and by the averaging time of the correlator (t_{avg}).

Thus, one possible method to increase the SNR of a DCS measurement is to increase $\langle I_d \rangle$, which can be accomplished by either increasing the source power or the detection efficiency. However, to avoid damaging the tissue, we must adhere to the source power limits imposed by the regulatory agencies, such as the American National Standards Institute (ANSI) in the US and the National Sanitary Surveillance Agency (ANVISA) in

Brazil. For example, for a laser emitting light at $\lambda = 785$nm the maximum permissible power for continuous illumination is 28.4 mW. Note, however, that the lasers commonly used in DCS experiments are capable outputting up to 100 mW. To use the higher power outputted by the lasers, but without damaging the tissue and staying within the regulatory limits, we can illuminate the tissue intermittently. For example, we can increase the power to 79 mW by illuminating the tissue during 2.5s, interleaved with 4.5s periods of no illumination [20]. Alternatively, we can also increase the power by increasing the illumination area. To this end, we can use optical diffusers attached to the tip of optical fibers to homogeneously deliver light over a wider area. For example, by using a diffuser with a diameter of 5.5mm, we can continuously illuminate the tissue at 50 mW maximum [130].

Besides increasing the source power, we can also increase the detected intensity and the SNR by improving the detection aspects of our measurements. More specifically, we can improve the SNR by: 1) increasing the number of detection channels used to compute the averaged auto-correlation curves; 2) using efficient detectors, and/or; 3) using few-mode fibers. By bundling multiple detection channels at approximately the same position, we can average multiple auto-correlation curves, which in turn increases the SNR by approximately $\sqrt{N}$, where N is the number of detection channels. Although increasing the number of detection channels is the most widely used solution for increasing the SNR of a DCS measurement, we are usually limited to a few detectors; each additional detection channel considerably increases the cost and the complexity of a DCS system. Another option to increase the SNR of DCS is to use high quantum efficiency single-photon detectors. In practice, the commercially available detectors have a quantum efficiency of $\sim 50\%$ for 785nm light.

We can also increase the detected intensity by using few-mode fibers; the detected intensity is linearly proportional to the number of modes allowed to propagate in the optical fiber. However, since β is inversely proportional to the number of modes allowed to propagate in the fiber, the increase in $\langle I_d \rangle$ is cancelled by the decrease in β, and the SNR is approximately unchanged [20, 131]. Additionally, the use of few-mode fibers may also introduces modal noise, which is not taken into account in Equation 2.32. Thus, most DCS applications employ high-transmission single-mode fibers.

Although in most DCS applications β is equal to 0.5 (single-mode fibers with non-polarized light), we could theoretically increase β by in introducing light polarizers. However, by introducing light polarizers we would also reduce the detected intensity, and thus we would not necessarily improve the SNR. It is worth mentioning that β is also decreased by instrumental factors, such as the dead time and non-linearities of the detector and associated electronics, as well as the finite sampling time of the correlator. Additionally, light leakage from the source directly to the detector can also lead to smaller β values.

Finally, the averaging time and the bin-width of the correlator can also affect the SNR of DCS measurements. The most commonly used method for computing the auto-correlation curves is the multi-τ scheme, where data are processed simultaneously for many different sample times, allowing measurements of both small and large values of τ [21]. In the multi-τ scheme, the delay-times are directly related to the bin-widths. The bin-widths increase with increasing delay-time, and thus we expect a higher SNR for the later portions of the auto-correlation curves. In most applications, the averaging time (t_{avg}) is controlled by the user and can be adjusted according to the need of each experiment. Note, however, that a minimum t_{avg} may be imposed by the correlator.

For human applications, although using a larger averaging time will lead to higher SNR, decreases in the sampling time may introduce aliasing due to the oscillating nature of the blood flow [132, 133]. In human measurements, the DCS measure of blood flow is sensitive to any hemodynamic events, as well as any hemodynamic oscillations, such as the heart-beat ($\sim 1Hz$), the respiration rate ($\sim 0.3Hz$) and the Mayer waves ($\sim 0.1Hz$) [93, 134–136]. Thus, a compromise between an increase in SNR and the ability to separate the different hemodynamic changes is necessary. Most studies using DCS were limited to slower sampling rates (up to 1 Hz) due to the hardware correlator commonly employed. More recently, *Wang et al.* proposed a software correlator capable of acquiring DCS data with sampling rates up to 100 Hz [137]. With their software correlator, it is possible to change the delay-times, the bin-width and the averaging time as required by the experiment.

In practice, the design of a DCS instrument requires a few extra considerations, besides the improvement of the SNR. First, to assure that the correlation loss measured by DCS is due to the scatterers movement, a long-coherence laser is required; typically, a coherence length larger than 10 meters is sufficient [20]. Second, besides a high quantum efficiency, the DCS detectors must have a good timing resolution (faster than 1 ns), a small dead-time ($< 50ns$) and small dark counts. In a typical DCS measurement in an adult head, we expect to measure approximately 20 thousand counts per second, whereas the commonly employed detectors have less than 500 dark counts per seconds. Thus, we can safely ignore the effect of the dark counts.

The DCS measurement of blood flow is sensitive to the external pressure of the optical probe against the tissue. By increasing the probe pressure, we will reduce the blood flow in the external tissues, and thus the BFI from DCS is also reduced [138–140]. For brain measurements, it has recently been shown that although the BFI is reduced due to the probe pressure, the heart-rate pulsatilty of BFI is unchanged [139]. However, for measurements on the forearm, the BFI heart-rate pulsatility is also decreased with increasing probe pressure. Interestingly, it is possible to use these changes in BFI due to the external probre pressure to separate the extra-cerebral and cerebral physiologies [140].

Last, the optical-derived CBF has physical units (i.e., cm^2/s) rather than the more usual clinical units (i.e., ml / 100 g of tissue / min). In order to estimate the absolute CBF measured with DCS in the clinical units a previous calibration of the technique is required. Some authors have proposed the use of an indocyanine-green (ICG) bolus to recover absolute CBF in clinical units from a FD-DOS or TD-DOS measurement. This estimate of CBF with DOS can be used to recover a calibration factor to convert the CBF index from DCS to the absolute clinical units [23, 117, 141]. In a recent paper, *He et al.* showed that the calibration factor from the ICG method is reliable across different monitoring days and different patients [117]. Additionally, *Milej et al.* showed that the ICG method can provide accurate measurements of CBF (when compared to arterial spin labelling (ASL)-MRI) by using a two-layer model of the head [23].

Chapter 3

Real-time assessment of cerebral hemodynamics with diffuse optical spectroscopies in a neuro intensive care unit

As previously mentioned in Chapter 1, one of the main goals in the care of patients with severe neurological conditions, such as stroke or head trauma, is to prevent secondary damage [2–5]. To this end, close patient monitoring following acute brain lesions is essential, and it may directly improve mortality and morbidity rates [6–8].

In order to expand the usefulness of diffuse optical methods into the clinic, some studies have employed frequency- (FD-DOS) and time-domain (TD-DOS) diffuse optical spectroscopy to measure absolute tissue oxygenation. Either FD-DOS or TD-DOS can be combined with diffuse correlation spectroscopy (DCS) for measurements of CBF and metabolism. The combination of DCS and FD/TD-DOS has been explored to monitor patients in several clinical scenarios, e.g., for neonatal monitoring [15, 32–34, 63], during cerebrovascular interventions [37, 38, 40, 41, 45, 142], as well as for monitoring of neurocritical patients [47, 49, 50]. However, these studies mostly focused on the effects of specific events and interventions. Concerning the practical clinical application of diffuse optical methods, the important question related to the correlation between neurophysiology, as measured by DCS/DOS, and the clinical evolution of patients during hospitalization remains largely unaddressed [1].

---

[1] The results presented in this chapter are partially based on a manuscript we submitted to the journal *Frontiers in Medicine* [143]

3.1 Methods

3.1.1 Subject recruitment

We monitored eight patients for a total of ~ 30 hours. Four of the eight patients were diagnosed with ischemic stroke, and four patients with a subarachnoid hemorrhage. The patients were recruited during their admission to the neuro-ICU of the Clinical Hospital at the University of Campinas, Brazil. The optical probe was held on the forehead with a flexible rubber band. Continuous optical measurements were taken for at least 1 hour per day during the period of the patient hospitalization. Each brain hemisphere was measured sequentially, for at least thirty minutes on each side. All monitoring sessions were supervised by a specialized neurologist. The study was carried out in accordance with the Belmont Report and written informed consent from all subjects (or legally authorized surrogate) was obtained. The protocol was reviewed and approved by the ethics committee at the University of Campinas (Protocol number 56602516.2.0000.5404). The ethics committee approval and the consent form can be found in Appendices B and C.

Due to either excessive patient movement, bad coupling of the optical probe or poor data quality due to low SNR, we opted to excluded 6 patients from our analysis. Thus, here we have only focused on two representative case studies. First, we described the case of a 62-year-old female patient who was admitted to the intensive care unit (neuro-ICU) following aneurysmal subarachnoid hemorrhage (aSAH). Second, we describe the case of a 50-years old female who presented with left sided hemiparesis[2] and was found to have an ischemic stroke due to an occlusion on the right MCA.

3.1.2 Experimental protocol

Since this was a pilot observational study, the experimental protocol was designed so that the optical measurements would not interfere with any clinical practices. Therefore, the timing of each optical monitoring session was purposely chosen to avoid conflicts with any planned clinical intervention. The majority of the monitoring sessions happened in the early afternoon, prior to family visitation hours. No treatment decisions were made based on the optical measurements. Mean arterial pressure (MAP), arterial blood oxygen saturation (SaO_2), hemoglobin concentration (Hgb) and CBF_v from TCD were retrospectively recovered from the medical records and were taken at most an hour before

---

[2] Hemiparesis is a paralysis of one side of the body.

or after the optical measurements.

3.1.3 Optical instrumentation

For this study, we developed a hybrid diffuse optical instrument employing both a DCS module and a commercial FD-DOS module (Figure 3.1). The homemade DCS instrument employs 16 single photon-counting detector arrays (SPCM-AQ4C, Pacer, USA) and one long-coherence laser emitting at 785 nm (DL785-100-SO, CrystaLaser, USA). The signal from the detector feeds a hardware correlator (Correlator.com, China) that outputs the DCS auto-correlation curves. The DCS module was characterized and validated during my Master's project [21]. The FD-DOS module (Imagent, ISS Inc., USA) employs 4 photomultiplier tubes as detectors and 32 laser diodes modulated at 110 MHz that provide 8 sources, with four different wavelengths each (690, 705, 750 and 846 nm).

To permit FD-DOS and DCS measurements, we used an Arduino board programmed inside our control software to automatically switch between each module. The interleaved measurements of FD-DOS and DCS is necessary in order to avoid damaging the PMTs of the FD-DOS module due to the high power of the DCS source. The total sampling rate of our system is ~ 0.16 Hz. We developed an user-friendly graphical user interface (GUI) with LabVIEW (National Instruments, USA) to control the operation of both modules and to display in *real-time* CBF, StO_2, and $CMRO_2$. The GUI was based on current instruments available at the neuro-ICU, and it was adapted after feedback by clinical users in order to facilitate its use by hospital staff, such as neurointensivists and nurses. The GUI displays the *real-time* CBF, StO_2 and $CMRO_2$ values, in both a 5 minutes and in a 2 hours time window (Figure 3.2).

The optical probe[3] consisted of one DCS source and three DCS detectors combined with four DOS sources and one DOS detector, providing a total of three DCS source-detector combinations (separated at 1.5, 2.0, and 2.5 cm), and four DOS source-detector combinations (separated at 1.5, 2.0, 2.5 and 3.0 cm) (Figure 3.1). In this work, we opted to focus on a single DCS source-detector separation (2.5 cm) and only two DOS wavelengths (690 and 846 nm). With these separations, we were capable of probing the most external surface of the prefrontal cortex (PFC), as it was shown in previous studies [24, 144].

---

[3] The optical probe was a small rubber pad of approximately 2×5 cm.

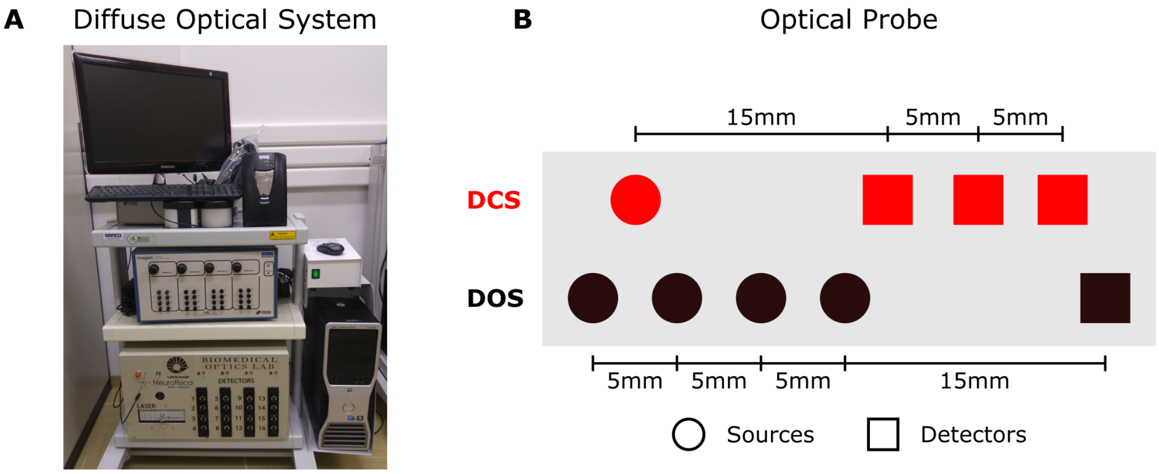

Figure 3.1: Instrumentation utilized for the study inside a intensive care unit. (A) The diffuse optical system, which combines a frequency-domain diffuse optical spectroscopy (DOS) module and a diffuse correlation spectroscopy (DCS) module. (B) A schematic of the optical probe employed in this study, which consisted of three DCS source-detector separations (1.5, 2.0 and 2.5 cm, in red) and four DOS source-detector separations (1.5, 2.0, 2.5 and 3.0 cm, in black). The optical probe was a small rubber pad of approximately 2×5 cm. This figure is part of a manuscript we recently submitted to Frontiers in Medicine [143].

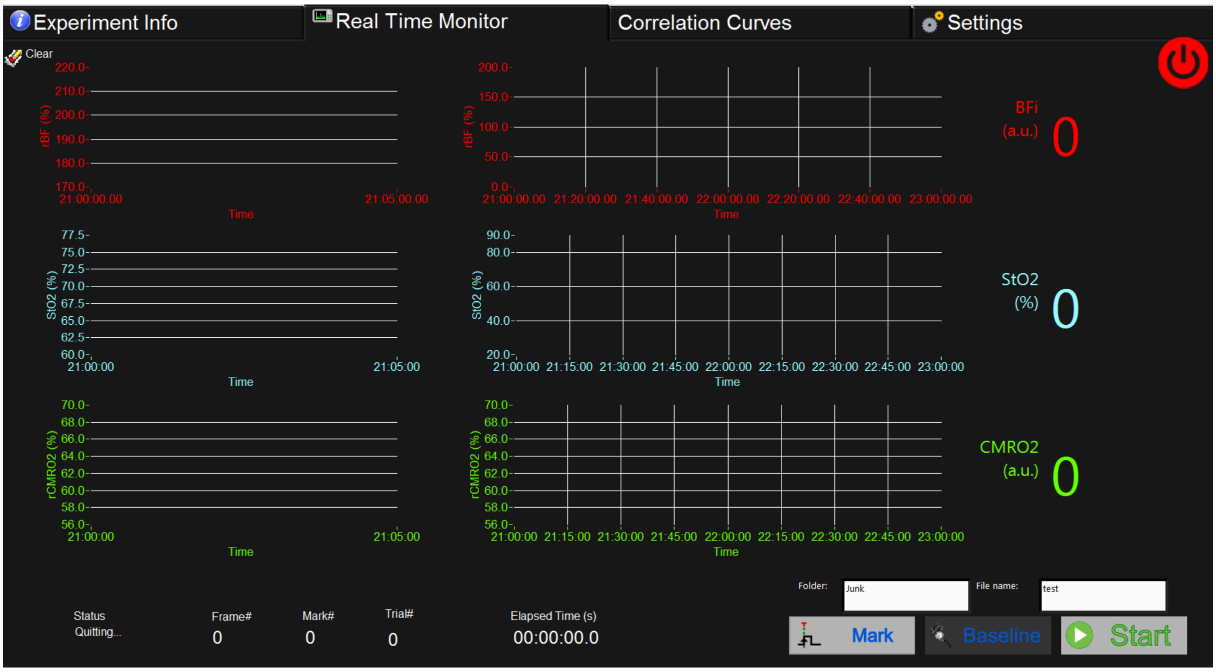

Status
Quitting...

Frame# 0

Mark# 0

Trial# 0

Elapsed Time (s) 00:00:00.0

Folder: Junk

File name: test

BFi (a.u.) 0

StO2 (%) 0

CMRO2 (a.u.) 0

Figure 3.2: Real-time graphical user interface (GUI) for the developed diffuse optical system. The interface display the *real-time* information of cerebral blood flow (CBF), oxygen saturation (StO_2) and cerebral metabolic rate of oxygen ($CMRO_2$), in a 5 minutes time window on the left, and in a 2 hours time window on the right.

3.1.4 Optical analysis

We employed a multi-spectral fitting algorithm to analyze the FD-DOS data. Briefly, we use a non-linear fitting procedure to compare the measured light intensity (AC_{Meas}) and phase (Ph_{Meas}) to the theoretical light intensity (AC_{Theo}) and phase (Ph_{Theo}) extracted from the solution of the diffusion equation assuming a semi-infinite homogeneous medium (Equation 2.8). In our approach, all DOS source-detector separations at all wavelengths were fit simultaneously to recover the HbO and HbR concentrations as well as the scattering parameters A and b using Equations 2.17 and 2.18, and we assumed constant water concentration fraction $f_{H_2O} = 0.75$. We used the Nelder-Mead non-linear least squares algorithm to minimize the cost-function:

$$\chi^2 = \chi^2_{Ph} + \chi^2_{AC}, \tag{3.1}$$

where

$$\chi^2_{AC} = \sum_{\lambda}\sum_{\rho_1}\sum_{\substack{\rho_2 \\ \rho_2 \neq \rho_1}} log\left(\frac{AC_{Meas}(\rho_1,\lambda)}{AC_{Meas}(\rho_2,\lambda)}\right) - log\left(\frac{AC_{Theo}(\rho_1,\lambda)}{AC_{Theo}(\rho_2,\lambda)}\right) \tag{3.2}$$

and

$$\chi^2_{Ph} = \sum_{\lambda}\sum_{\rho_1}\sum_{\substack{\rho_2 \\ \rho_2 \neq \rho_1}} \left(Ph_{Meas}(\rho_1,\lambda) - Ph_{Meas}(\rho_2,\lambda)\right) - \left(Ph_{Theo}(\rho_1,\lambda) - Ph_{Theo}(\rho_2,\lambda)\right). \tag{3.3}$$

To improve the stability of our fitting procedure, we first calculated the average scattering coefficients (i.e., A and b) from either the initial or the last 10 minutes of data (depending on the hemisphere placement order). Then, using the fixed parameters for A and b, we computed the HbO and HbR concentrations from each time point.

For the DCS analysis, we first estimated the absorption and scattering coefficients at the DCS wavelength (i.e., 785 nm) using the parameters recovered from the multi-spectral fit of our DOS data. Then, we fit the measured autocorrelation function to a semi-infinite homogeneous dynamic model to recover a BFI (Equation 2.16). For the DCS data, each source-detector separation was fit independently [13]. All analysis scripts were written using open-source libraries based on Python 3 [145–147].

Tissue oxygen saturation (StO_2) was calculated as the fraction of HbO considering all hemoglobin concentrations (i.e., $StO_2 = HbO/HbT$, where $HbT = HbO + HbR$). Oxygen extraction fraction (OEF) was computed as $OEF = (SaO_2 - StO_2)/(\gamma * SaO_2)$, where SaO_2 is the arterial blood oxygen saturation, and γ is the percentage of blood volume contained in the venous compartment of the vascular system, assumed to be 0.75 [30, 63]. From CBF and OEF, the cerebral metabolic rate of oxygen ($CMRO_2$) can be estimated as $CMRO_2 = Hgb * CBF * OEF$ [30, 31, 63]. All neurophysiological parameters were calculated for each time point continuously every 6 seconds.

Since systemic physiological data (MAP, SaO_2 and Hgb) were recovered from the medical records (which were collected every 2 hours), we only report the average data points of each neurophysiological parameter calculated across each optical monitoring session. This procedure allowed us to compare data from different sources. The error bars in the plots represent the standard deviation of the data across the time-window used for averaging.

3.2 Results

3.2.1 Cerebral hemodynamics of a subarachnoid hemorrhage patient monitored during hospitalization

We first report on the case of a 62-years-old female who was admitted to the neuro intensive care unit after a severe headache for 3 days associated with nausea, vomiting and elevated blood pressure. She rapidly progressed to coma right after admission. The first CT scan after admission revealed a right middle cerebral artery (MCA) aSAH with a Grade V on the Hunt & Hess scale (i.e., predicting a poor outcome and a low likelihood of survival, see Table A.1) [148] and Grade III on the Fisher Scale (i.e., low to high risk of vasospasm[4], see Table A.2) [149]. The TCD measurement performed on the first day of hospitalization did not show any signs of vasospasm (mean CBF_v of 73 cm/s and 83 cm/s, for the right and left MCA, respectively).

We started monitoring the patient with our diffuse optical system on the second day following admission, approximately 32 hours after hospitalization. At that time, MAP was 90 mmHg and we found lower CBF and $CMRO_2$ on the ipsilesional sideof the PFC when compared to the contralesional side [5] , consistent with lower metabolism following a brain hemorrhage. The OEF and the total hemoglobin concentration (HbT, which is proportional to cerebral blood volume) was similar between the two hemispheres. Figure 3.3 shows the daily averages of all the cerebral measurements obtained with our diffuse opti-

---

[4] Vasospasm is a sudden constriction of a blood vessel, reducing its diameter and flow rate.

[5] The ipsilesional side is the hemisphere on the side of the lesion, while the contralesional side is the opposite hemisphere.

cal system along with the mean arterial pressure and the CT scans performed during the whole hospitalization period. Shortly after the first optical monitoring session, the patient underwent an emergency ventriculostomy with EVD placement due to high intracranial pressure.

On the third day of hospitalization, during the second optical monitoring session, a large increase in MAP was observed (up to 122 mmHg), associated with an overall increase in CBF and $CMRO_2$. The increase in CBF and $CMRO_2$ was comparatively higher in the ipsilesional side. In addition, an increase in ipsilesional OEF and a decrease in ipsilesional HbT were also measured, suggesting high metabolic demand due to low blood availability in tissue. The CT scan obtained in the fourth day after admission revealed an extensive ischemic area on the ipsilesional hemisphere. The TCD performed in the fourth day found mean CBF_v of 64.2 and 68.3 cm/s on the right and left MCAs, respectively. In the fourth day of hospitalization, the patient evolved with non-photo reacting pupils and absent corneal reflex. The clinical examination remained unchanged even after analgesic and sedative drug withdrawal. With this prognostic, the clinical staff opted for comfort care. Due to intermittent clinical care to assist the patient, no optical monitoring was taken between the fourth and the fifth days.

On the sixth day of hospitalization, during the third optical monitoring session, OEF was below 40% in both hemispheres. Compared to the first optical monitoring session, CBF increased by 40 and 51% in the ipsilesional and contralesional sides, respectively. However, the increase in CBF was not followed by any significant changes in $CMRO_2$ (Figure 1). From the second to the sixth day after hospitalization, HbT increased in the contralesional side and decreased in the ipsilesional side. MAP at the sixth day was 85 mmHg.

For the following two days, ipsilesional CBF and $CMRO_2$ further decreased, respectively, by 82 and 69% (compared to day 6), and OEF dramatically increased by approximately 76%. Cerebral blood volume (CBV), as estimated by HbT) decreased in the contralesional side, reaching the levels of CBV in the ipsilesional side. The ipsilesional CBV remained relatively stable between the second and ninth day of hospitalization. The patient died on the ninth day after hospitalization. MAP decreased to 67 and 45 mmHg during the last two monitoring sessions, respectively.

The differences between the ipsilesional and the contralesional sides over the entire period can be more directly analyzed by computing the laterality index (LI) for each

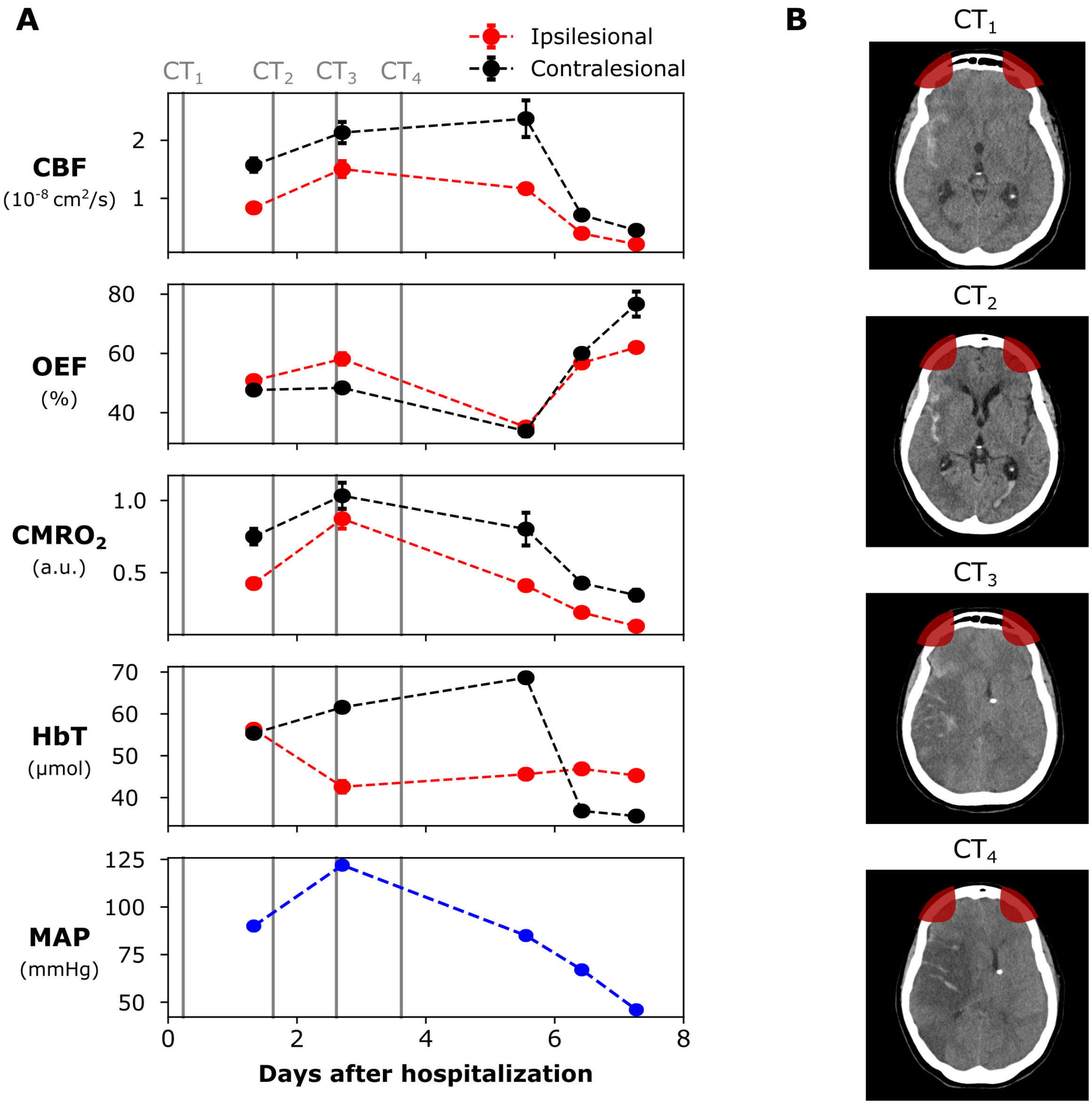

Figure 3.3: Evolution of the brain lesion in a 62 years old female patient following a high-grade aneurysmal subarachnoid hemorrhage (aSAH). (A) Neurophysiological parameters measured with the diffuse optical system, as well as the systemic mean arterial pressure (MAP). (B) Computed tomography (CT) images at different days during hospitalization (marked as vertical lines in the left panel). The patient died in the ninth day after hospitalization. The red areas in the CT images represent the optical sensitivity region. The error bars of each point represent the standard deviation of each parameter across the monitoring time-window. For some days, the standard deviation was too small to be shown. CBF: cerebral blood flow; OEF: oxygen extraction fraction; CMRO$_2$: cerebral metabolic rate of oxygen; HbT: total hemoglobin concentration. This figure is part of a manuscript we recently submitted to Frontiers in Medicine [143].

physiological parameter:

$$LI = \frac{X_{ipsi} - X_{contra}}{X_{ipsi} + X_{contra}}, \tag{3.4}$$

where X represents the parameter measured, and the subscript denotes the brain side.

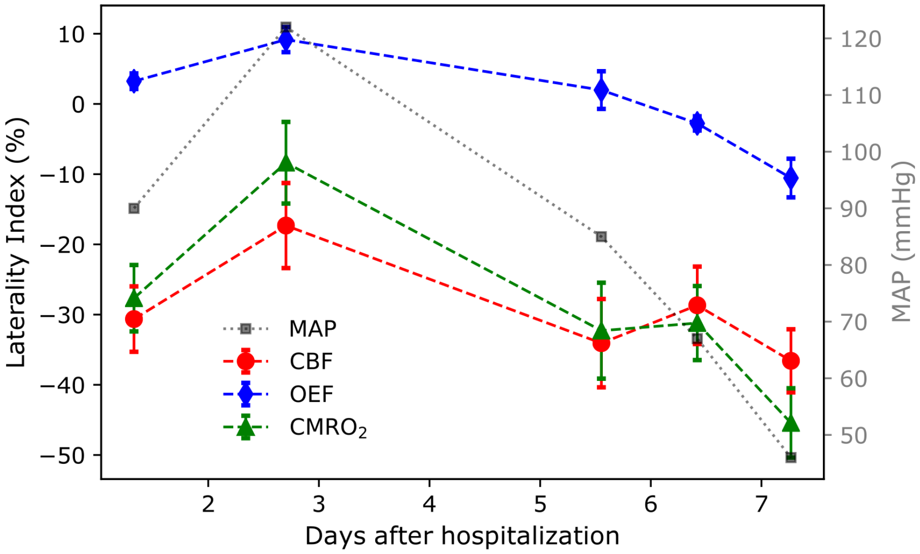

Figure 3.4: Temporal evolution of the laterality index for the optically derived physiological parameters in a 62 years old female patient following a high-grade aneurysmal subarachnoid hemorrhage (aSAH). The changes in the ipsilesional hemisphere compared to the changes in the contralesional hemisphere are shown in the left axis for cerebral blood flow (CBF, red circles), oxygen extraction fraction (OEF, blue diamond) and cerebral metabolic rate of oxygen (CMRO$_2$, green triangles). Evolution of the mean arterial pressure (MAP, gray squares) are shown in the right-axis for comparison. The error bars of each point represent the standard deviation of each parameter across the monitoring time-window. For some days, the standard deviation was too small to be shown.

Figure 3.4 shows the LI evolution over time for the patient following aSAH for all the hemodynamic and metabolic parameters provided by the optical system. Careful analysis of Figure 3.4 reveals two significant periods of hemispheric impairment. The first period occurred between the first and the third days after hospitalization, in which all the neurophysiological parameters in the ipsilesional PFC increased more than in the contralesional side. After the third day of hospitalization, the LI continuously decreased on the following days, consistently with the worsening of the patient condition.

3.2.2 Cerebral hemodynamics of a severe ischemic stroke patient

In order to further illustrate the capability of diffuse optical methods in the neuro-ICU in a wide range of neurological injuries, we also report on another case with a different stroke etiology and clinical outcome. The patient is a 50-years-old female with a history of diabetes, hypertension, and congestive heart failure, who presented with left sided hemiparesis and was found to have an ischemic stroke due to an occlusion on the right MCA with a National Institute of Health Stroke Scale (NIHSS) of 11 (i.e., a moderate

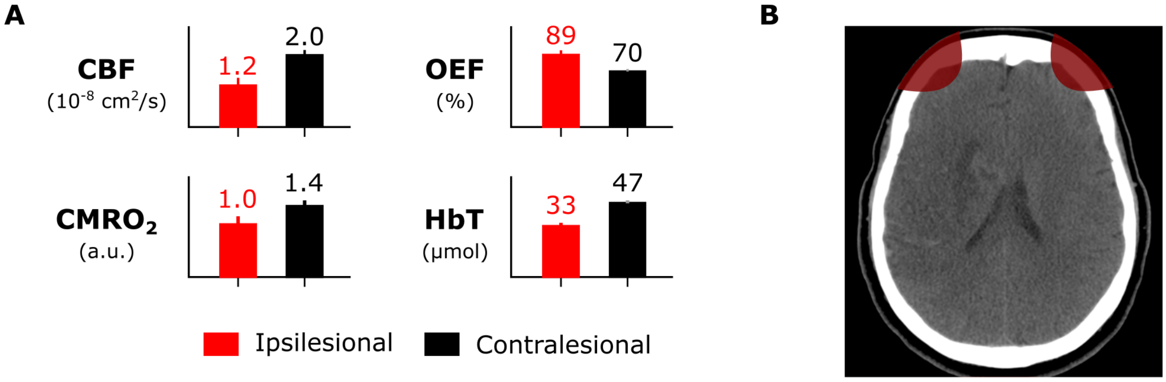

Figure 3.5: Neurophysiological information of a patient diagnosed with severe ischemic stroke on the right middle-cerebral artery at the thirteenth day after hospitalization. (A) Cerebral blood flow (CBF), oxygen extraction fraction (OEF), cerebral metabolic rate of oxygen ($CMRO_2$) and total hemoglobin concentration (HbT) measured with the diffuse optical system in the contralesional and the ipsilesional hemispheres. (B) Computed tomography (CT) scan from the single-day measurement of the patient. The red areas in the CT images represent the optical sensitivity region.

stroke, see Table A.3) [150]. Figure 3.5 shows the patient optical-derived parameters and the CT scan at the thirteenth day after hospitalization, while the patient was intubated and sedated. The CT image on the thirteenth day revealed an extensive ischemia on the right hemisphere. During this single monitoring session, CBF, $CMRO_2$ and HbT in the ipsilesional hemisphere were considerably lower than the contralesional hemisphere, consistent with a perfusion deficit and subsequent tissue necrosis caused by the large ischemia. Additionally, OEF in the ipsilesional hemisphere was 27% higher than OEF in the contralesional side, possibly reflecting the high demand of the surrounding tissue due to low blood availability in the affected hemisphere. During the monitoring period, the patient's arterial blood pressure was 129/65 mmHg. Ultimately, this patient was discharged after 42 days of hospitalization with severe residual deficits.

3.3 Discussion

Diffuse optics has been previously validated in different clinical settings as an alternative bedside monitoring tool, and it holds potential to personalize clinical management. Despite limitations in the penetration depth inherent to any diffuse optical technique [13, 17, 144], both DCS and DOS are capable of monitoring cerebral hemodynamics noninvasively and in real-time, without the use of exogenous contrasts, ionizing radiation, and without interfering with the current clinical practices. Unlike global systemic physiological monitors, the principles of light propagation limit the measurement to a region of interest, which can be useful to monitor specific regions such as an ischemic penumbra[6] or the region around a local brain injury. In addition, due to its portability and low cost, diffuse optical methods can be very useful to clinicians in places where clinical care conditions are restricted, such as during sports, in military fields and in developing regions. In these scenarios, access to other neuroimaging tools are very limited. Even in better clinical conditions, access to daily neuroimaging data for longer periods of time may not be readily available.

In this work, we report on results from two representative case-studies as part of translating a diffuse optical system to the neuro-ICU. For simplicity, we limited our measurements to the forehead, and thus we were only sensitive to focal changes in the PFC, which turned out to be sufficient to elucidate the main events during the evolution of the patient's brain injury. Here, we focused on the feasibility of performing longitudinal measurements in the neuro-ICU with the optical device. For this reason, to reduce possible interference with clinical interventions, we opted to minimize both the size of the optical probe and the monitoring time per day. However, we note that these choices are not intrinsic limitations from the optical system. The optical probes are small and customized so that they can be temporarily detached from the patients for any necessary reason. Since our optical system measures absolute concentration, we are not limited to a baseline or reference period. Also, the system's high portability allows its relocation alongside the patient with minimal time and effort. Concerning the duration of the measurement, long-term continuous monitoring (i.e., several hours per day) poses no extra-challenge in the present system. In fact, previous studies have reported optical measurements with a similar optical system for as long as 8 hours per day, both in adults [47, 50] and in neonates at the ICU [151].

The first observational case report presented in this work concerned a patient severely affected by aSAH, who was admitted almost three days after the event. Optical measurements obtained with DCS/DOS were consistent with the triphasic evolution of aSAH: hypoperfusion, hyperemia, and vasospasm [152, 153]. To the best of our knowledge, this is the first report on DCS/DOS long-term monitoring during the different phases following aSAH.

During the first day of monitoring, the patient had poor ipsilesional CBF and $CMRO_2$ but normal OEF when compared to the contralesional side, consistent with a hypoperfu-

---

[6] Ischemic penumbra is an ischemic tissue potentially destined for infarction but that is not irreversibly injured.

sion phase. In a previous PET study, *Yundt et al.* found similar trends of reduced CBF and $CMRO_2$, but unaffected OEF, during the early phases of aSAH [154, 155]. This pattern of low CBF and $CMRO_2$ but unaffected OEF may be related to an ongoing ischemia, to the start of the vasospasm phase or to a sign that the injury-related neurologic deficits have not yet peaked. Based on the first CT scan (collected prior to our first monitoring session, Figure 3.3), our results are most likely related to an ongoing ischemia. The initial aSAH insult (i.e., blood in the subarachnoid space) may impact mitochondrial function and diminish oxidative metabolism in favor of anaerobic metabolism [156], which may further explain our findings of low CBF and $CMRO_2$, but unaffected OEF.

At the third day after hospitalization, we found an increase in OEF at the ipsilesional side, which was associated with a bilateral increase in CBF and $CMRO_2$ (with a comparatively higher ipsilesional increase, Figure 3.4). Previously, *Yokose et al.* found decreased ipsilesional oxygen saturation (which corresponds to increased OEF) in severe aSAH patients with angiographic vasospasm with TD-DOS [157]. Thus, the higher OEF during the third day after hospitalization could be an indicative of vasospasm. The fact that the patient evolved to a severe ipsilesional ischemia between the fourth and fifth days is another indicative of vasospasm. Taken together, our results corroborate *Yokose et al.*'s, and reinforces the argument that decreases in tissue oxygenation (or, similarly, increases in OEF) may be a more sensitive measure of vasospasm than blood velocity in large arteries measured by TCD. Of note, prolonged elevation of ICP may also induce ischemia in aSAH patients; in this study we did not assess ICP, therefore we cannot confirm the real cause for ischemia in this patient.

We also measured increased CBF and decreased OEF in the contralesional side of the patient between the second and the sixth days following hospitalization. During these measurements, there was no significant difference in MAP. The increase in CBF with lower OEF is indicative of cerebral hyperemia that may have been secondary to an inflammatory mediated process causing significant vasodilation of the microvascular bed (therefore increasing CBF and HbT) [156, 158]. The cerebral hyperemia in the contralesional side may also be explained by an attempt to restore metabolic balance in the affected tissue. However, by this time the patient had already developed a large ischemic insult, and only the healthy tissue was capable of increasing CBF and appropriately oxygenating the tissue. Additionally, the ipsilesional ischemia may explain the fact that CBV (as measured by HbT) remained approximately constant across the different monitoring days (besides the first monitoring session).

In addition to the neurophysiological parameters, the possibility to probe hemispheric impairment can provide extra information to the patient's condition. The laterality index has been shown to be very useful for different clinical scenarios [159–162], and it can be readily assessed with the optical system by measuring both hemispheres. In the specific case of the aSAH patient, the LI revealed different dynamics during the period of hospitalization (Figure 3.4). The increase in LI at the third day after hospitalization could be indicative of a possible homeostatic attempt to restore the metabolic balance of the affected tissue. Similarly, the continuous decrease in the LI after day 3 is likely to reflect the worsening condition of the patient.

To further illustrate the general potential of diffuse optics in the neuro-ICU, we also presented a single-day study of a patient diagnosed with a severe ischemic stroke. In this case, we found a large CBF mismatch between the ipsilesional and the contralesional hemispheres (Figure 3.5), in agreement with the CBF mismatch from the aSAH patient after the development of cerebral ischemia. Notably, although CBF was lower on the ipsilesional hemisphere, we found high OEF in both hemispheres, which was comparatively higher on the ipsilesional hemisphere. This may be consistent with the idea of misery perfusion, a state in which there is high oxygen consumption (high OEF) despite low (but non-zero) CBF as the tissue attempts to promote recovery [50, 154, 162]. Currently, misery perfusion is hard to diagnose, and a larger study with acute ischemic stroke patients is needed in order to assess the feasibility of detecting misery perfusion with diffuse optical methods. Regardless, the second case study evidences the consistency and reproducibility of the results obtained with the diffuse optical measurements across different patients with different acute cerebrovascular diseases, and it further illustrates the potential of the technique to provide neurointensivists with accurate noninvasive neurophysiological information.

Overall, the results from the pilot observational case study presented here provide evidence that neurophysiological information derived from DOS and DCS is consistent with patient's clinical condition following different stages of an aSAH patient, as well as in an ischemic stroke patient. The optically-derived hemodynamic parameters were sensitive to the mismatch between the physiology of the ipsilesional and contralesional sides. We note, though, that further clinical studies with larger populations are needed to analyze the accuracy of the technique to find specific events, and/or to measure the effects of potential treatments on the patient's cerebral physiology. Together, our results reinforce that diffuse optics may provide useful information at the patient's bedside which could aid clinicians to make decisions based on the patient neurophysiology. The real-time access to patient's physiological condition may positively impact clinical care and therefore patient outcome [163–165]. In addition, our results show the feasibility of performing diffuse optical monitoring in a restricted environment in a developing country where access to other methods of cerebral monitoring are not always readily available.

Even though the optical results show strong agreement with clinical outcome, it is worth noting that the optical parameters can be more accurate. In this work we modeled the head as a semi-infinite medium for the DCS/DOS data analysis. By using the simplest model for analysis in order to get real-time monitoring, our results do not account for extracerebral contributions. Thus, it is likely that we have underestimated the cerebral physiology changes in CBF, HbT, OEF and $CMRO_2$ [14, 17, 144, 166]. In the future, multi-layer models can be used to isolate extracerebral contributions to the optical signal (for more information, see Chapter 5 and [20, 166–172]). However, these models either require an extra step in the monitoring setup or may not yet be reliable for clinical use. Nonetheless, the quantification of the neurophysiological changes does not affect the comparison between hemispheres, since extracerebral contributions are expected to similarly affect both the ipsilesional and the contralesional hemispheres.

3.4 Conclusion

To summarize, in this study we presented two observational case reports recorded during the translation of a hybrid diffuse optical system for real-time monitoring of cerebral hemodynamics inside a neuro-ICU. Our results suggest that optics may provide supporting information to monitor secondary damage following brain injury, and that optics can be safely and noninvasively applied early during hospitalization, at the bedside with minimal interference with standard clinical practices. The optically-derived hemodynamic parameters provide neurophysiological information at the microvasculature, which was consistent with the clinical outcome. Although we focused on two representative cases, our results support that diffuse optics can be a reliable tool for bedside monitoring and encourage further clinical validations with DCS/DOS in the neuro-ICU. Translation of diffuse optics to these settings can positively impact clinical care and patient outcome and can be especially useful in low-budget hospitals and in remote areas, where cerebral physiology monitoring is essential but not readily available.

Chapter 4

Cerebral optical monitoring of endovascular treatment of stroke

Mechanical thrombectomy has revolutionized treatment of patients with acute ischemic stroke due to large vessel occlusion, by providing rapid restoration of blood flow to ischemic brain tissue [173, 174]. Briefly, the mechanical thrombectomy procedure involves threading a catheter through the femoral artery to reach the clot in the cerebral artery and then mechanically remove it. Currently, procedural success for mechanical thrombectomy is defined by the degree of vessel recanalization visualized by angiography, most often using the modified treatment in cerebral ischemia score (mTICI, see Table A.4 for more details) [175, 176]. However, only about one-third of patients experience complete recanalization. The majority are left with some degree of residual cerebral hemodynamic impairment [173], which in turn correlates with infarct growth and greater long-term disability [177]. Moreover, the degree of large artery recanalization, an anatomic structural observation, does not always reflect parenchymal cerebral blood flow (CBF) [178–180], and this physiological factor holds potential to better predict infarct volume [178], clinical outcome [180], and inform medical management strategies. Currently, there is no suitable tool to measure CBF during mechanical thrombectomy in real-time, thus a continuous bedside monitor has potential to impact patient care.

Transcranial optical monitoring during mechanical thrombectomy has been carried out recently with commercial CW-DOS (or NIRS) instrumentation [46, 83]. While encouraging, these studies only found small changes in oxygen saturation, and the results did not necessarily correlate with outcome. Importantly, in these studies, the commercial NIRS systems may not have offered the most sensitive measure of change in the context of recanalization. Commercial NIRS may not accurately distinguish scalp and brain changes, and direct CBF monitoring with DCS, which is not possible with NIRS, may be a more sensitive tool for probing physiological changes during mechanical thrombectomy. The DCS blood flow signal is weighted towards comparatively (e.g., compared to NIRS) longer photon paths [144, 181] that penetrate more deeply into the brain. Additionally, the relative difference between intracerebral and extracerebral flow is greater than the relative difference in oxygen saturation between these two compartments. Therefore, it is likely that optical monitoring of CBF using DCS is inherently more sensitive to cerebral physiology changes than commercial NIRS systems [14, 17, 138, 144, 182].

In this chapter, we will describe our previously published study regarding the use of DOS and DCS for real-time monitoring of bilateral frontal lobe microvascular CBF during and after recanalization [142]. This work documented important first steps towards establishing continuous diffuse optical monitoring of cerebral microvasculature as a means for non-invasive, patient-specific quantification of tissue-level reperfusion following mechanical thrombectomy.

4.1 Methods

4.1.1 Subject recruitment

Between December, 1, 2017 and July, 2, 2018, we monitored 7 patients as part of an ongoing protocol to evaluate the safety and efficacy of transcranial optical monitoring during mechanical thrombectomy. More specifically, we monitored patients undergoing mechanical thrombectomy to treat acute ischemic stroke caused by unilateral occlusion of the cerebral arteries at the Hospital of the University of Pennsylvania. In total, we monitored 5 patients with unilateral middle-cerebral artery (MCA) occlusions, and 2 patients with unilateral internal carotid artery (ICA) occlusions. Since we were restricted to measurements on the forehead in this study, and since measurements on the forehead may not be sensitive to all MCA occlusions, herein we focus on and describe only preliminary results from two ICA occlusion patients. In both cases, mechanical thrombectomy was performed under general anesthesia. Endotracheal intubation occurred immediately prior to the initiation of optical monitoring, and mechanical ventilation continued throughout the course of the monitoring protocol.

The study was carried out in accordance with the Belmont Report with written informed consent from all subjects (or legally authorized surrogate). Given the time-sensitive nature of mechanical thrombectomy and the non-significant risk associated with this research protocol, written informed consent was obtained retrospectively. The protocol was approved by the University of Pennsylvania Institutional Review Board (Protocol Number 828249).

4.1.2 Experimental protocol

Eligible patients were identified by a vascular neurologist. In accordance with standard-of-care, patients were transported to the interventional neuroradiology suite in order to perform mechanical thrombectomy. After the patient was situated on the procedure table, optical probes were placed bilaterally on the lateral aspect of the forehead (Figure 4.1). To optimize the optical signal, care was taken with probe placement to avoid hair and frontal sinuses. The probes were fixed to the head with double-sided tape and an elastic bandage. Once the probes were secured, the light sources were turned on, and cerebral hemodynamic data was collected throughout the course of the mechanical thrombectomy procedure.

Patients routinely remained on the procedure table for several minutes after completion of the thrombectomy, and optical data collection continued during this time. Just prior to removing the patient from the procedure table, data collection was stopped, and the optical probes were removed from the patient's head. The TD-DOS IRF measurement was then carried out in a manner described elsewhere [114, 115]. MAP data was recorded once every minute and were retrospectively retrieved from the anesthesia record and time-synced with optical data. MAP was monitored either with an invasive catheter or a brachial cuff, depending on clinical availability.

4.1.3 Optical instrumentation

For this study, we developed a hybrid diffuse optical instrument that combines a homemade TD-DOS and a homemade DCS module (Figure 4.2-A). The TD-DOS module contains two pulsed lasers (BHLP-700, Becker&Hickl, Germany) emitting short light pulses ($\sim$100 ps) at a 50 MHz repetition rate and operating at different wavelengths (685 and 830nm), one hybrid photomultiplier tube (HPM-100, Becker&Hickl, Germany), and a TCSPC board (SPC130, Becker&Hickl, Germany). The DCS system contains 16 single-photon counters (SPCM-AQ4C, Pacer, USA) connected to a fast software correlator [137], as well as two long-coherence-length source lasers emitting light at 785nm (DL785-100-SO,

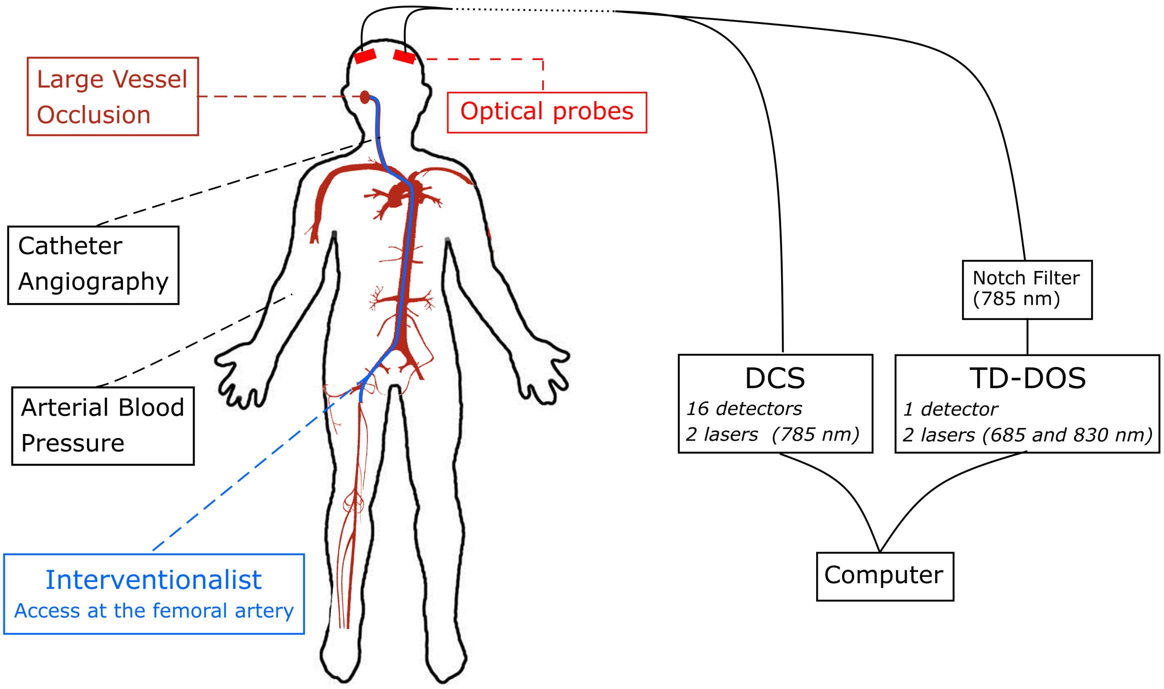

Figure 4.1: Schematic of the experimental setup for monitoring mechanical thrombectomy. After the patient was situated on the procedure table, two fiberoptic optical monitoring probes were placed on the lateral aspect of the forehead, bilaterally. Groin access and mechanical thrombectomy proceeded without delay. Microvascular cerebral blood flow (CBF), oxy-hemoglobin concentration, and deoxy-hemoglobin concentration were simultaneously monitored on the ipsilateral hemisphere with Diffuse Correlation Spectroscopy (DCS) and Time-Domain Diffuse Optical Spectroscopy (TD-DOS). A notch filter (centered at 785 nm) was placed in front of the TD-DOS detector to facilitate simultaneous TD-DOS/DCS measurements. On the contralateral hemisphere, CBF alone was monitored with DCS. This figure was extracted from our previously published study [142].

CrystaLaser, USA).

To permit simultaneous TD-DOS/DCS measurements, we introduced a fiber-coupled notch filter centered at 785 nm before the TD-DOS detector to block light from the DCS source (OZ Optics, Figure 4.1). Data acquisition was controlled with custom-written software in the LabVIEW environment (National Instruments, USA), with an interface based on current clinical monitors (similar to the interface from Chapter 4). The data acquisition rate was 20 Hz for DCS and 0.7 Hz for TD-DOS. For DCS, we employed two source-detector separations on each hemisphere: one short separation (0.7 cm) primarily sensitive to extra-cortical tissue, i.e., scalp and skull, and one long source-detector separation (2.5 cm), which has been shown to provide acceptable SNR and cortical sensitivity [17, 144, 182]. Since we were limited to use of a single TD-DOS detector, the TD-DOS measurement was made with a single, large source-detector separation (3.2 cm) on the

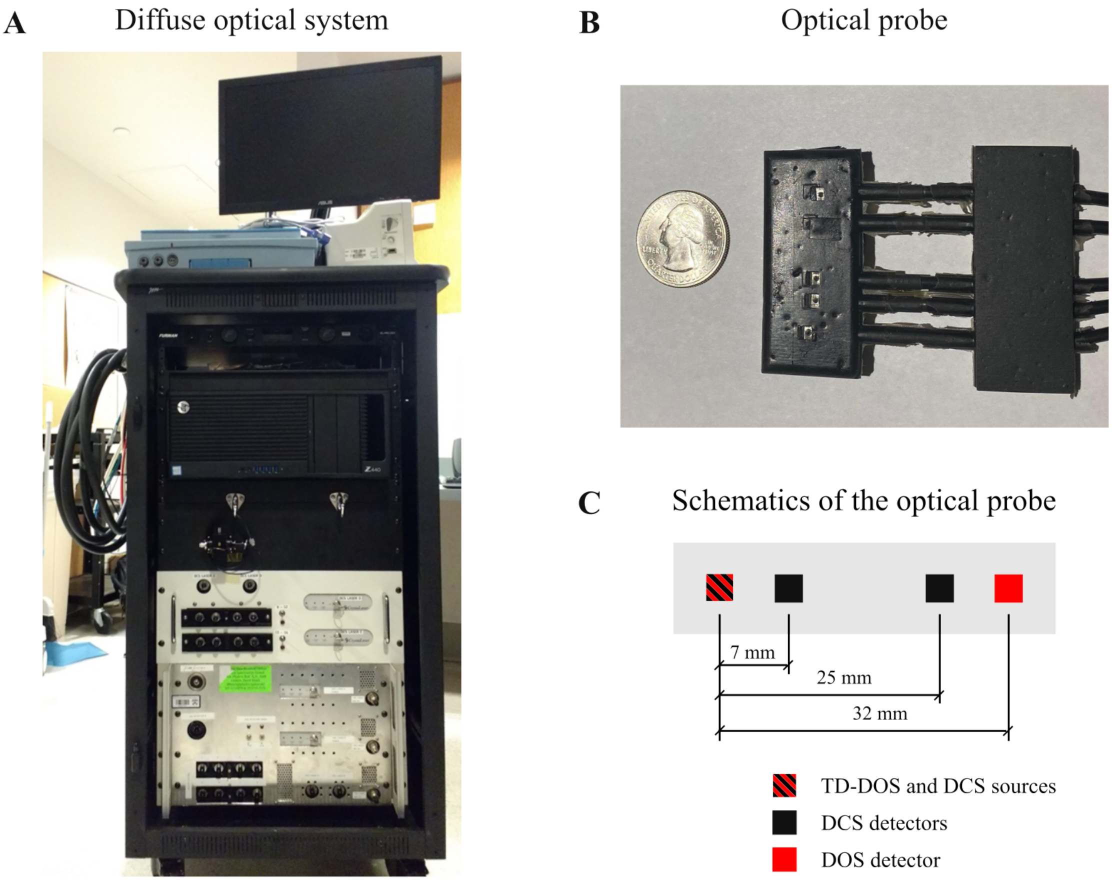

Figure 4.2: Instrumentation used to measure the cerebral hemodynamics of patients during mechanical thrombectomy. In (A) we show the instrument utilized in this study, which consisted of a time-domain diffuse optical spectroscopy (TD-DOS) module and a diffuse correlation spectroscopy (DCS) module. For simultaneous TD-DOS and DCS measurements, we used a notch filter (785 nm). (B) We created two rubber pad ($\sim 2 \times 5$ cm) to hold the optical fibers bilaterally on the forehead. The probes were fixed to the head with double-sided tape and an elastic bandage. Each probe consisted of two separations for DCS and one separation TD-DOS. However, we were only measured with TD-DOS on the hemisphere ipsilateral to the occlusion.

hemisphere of interest, i.e., ipsilateral to the occlusion[1]. We created a rubber pad ($\sim 2 \times 5$ cm) to hold the optical fibers on the forehead (Figure 4.2-B and C).

4.1.4 Optical analysis

The temporal decay of the DCS autocorrelation function, and therefore the recovered CBF indices, are sensitive to the optical properties of the underlying tissues. Thus, to improve DCS accuracy, we estimate the tissue absorption and reduced scattering coeffi-

---

[1] The ipsilateral hemisphere is the hemisphere on the same side as the occlusion.

cients independently with TD-DOS (for more details about TD-DOS see Section 2.2.1.4 and [59, 104, 109, 141]). For each TD-DOS wavelength, λ, we fit the baseline-averaged DTOF (i.e., averaged over $\sim$ 5 minute interval before the initiation of cerebral vasculature manipulation) to a convolution of the TD-DOS IRF and the semi-infinite Green's function solution of the photon diffusion equation. This enables the calculation of baseline tissue absorption and reduced scattering coefficients, i.e., $\mu_{a,o}(\lambda)$ and $\mu'_{s,o}(\lambda)$, along with the effective launch time of the incident source pulse on the tissue (T_o) [59, 109]. Thereafter, the DTOF acquired at every measurement time was fit to derive an absorption coefficient, $\mu_a(\lambda)$; these fits assumed constant reduced scattering coefficient and constant T_o (both were derived from baseline fit). The multispectral tissue absorption measurements also assume a water volume fraction of 0.75 (Equations 2.17 and 2.18). The scheme permits recovery of HbO and HbR concentrations at every time-point. This information, in turn, enables calculation of the tissue absorption and scattering coefficients at the DCS wavelength (785 nm) using the chromophore extinction coefficients [62].

To help distinguish between intracerebral and extracerebral blood flow changes, we employed a multi-distance DCS measurement. An approximate rule of thumb, which we will utilize in our thinking and analysis, is that the short source-detector separations measure exclusively extracerebral blood flow changes, while the long source-detector separations measure relative changes of cerebral blood flow (rCBF).

To improve the signal quality, we first down-sampled the DCS data by averaging sequential sets of two temporal autocorrelation curves measured by DCS. Then, to recover the blood flow changes, we separately fit the autocorrelation curves for each separation using a semi-infinite homogenous tissue model (Equation 2.16). We use a baseline-averaged autocorrelation curve (averaged over $\sim$ 5 minutes before the initiation of cerebral vasculature manipulation) to recover the coherence factor in the Siegert relation (β) [125]. Next, we fit every frame for the DCS blood flow index, assuming that β remains constant throughout the experiment. Finally, to reduce the effects of systemic physiological variations, the data was low-pass filtered using a Butterworth filter with a cutoff frequency of 0.0167 Hz. All analysis scripts were written using open-source libraries based on Python 3 [145–147].

4.2 Results

Patient 1 presented with acute onset aphasia and right hemiplegia, with admission a NIHSS of 24 (i.e., a severe stroke, Table A.3). The patient was not eligible for intra-

Table 4.1: Baseline, procedural, and outcome summary.

	Patient 1	Patient 2
Baseline		
Age	80-85	60-65
NIHSS	24	15
Vessel occlusion	left cervical ICA	right cervical ICA
ASPECTS	8	7
Infarct core (cc) *	5	19
Penumbra (cc) *	187	97
Procedural details		
Time from onset to recanalization (min)	196	278
Final mTICI score	2b	2b
Early complications	None	Difficulty achieving revascularization in context of ICA dissection
Late complications	None	Edema and hemorrhagic conversion necessitating decompressive hemicraniectomy
Outcome		
Discharge NIHSS	1	17
Discharge disposition	Home	Rehabilitation

*based on CT perfusion imaging analysis by RAPID software (iSchemaView, Inc., USA). Infarct core is defined by CBF $< 30\%$. Penumbra is defined by $\mathrm{T}_max > 6$ seconds.

venous thrombolysis because of oral anticoagulation use. The patient was transferred for consideration of mechanical thrombectomy; initial imaging revealed left ICA occlusion with patent intracranial circulation. Left hemisphere appeared to be filling via anterior communicating artery. CT perfusion identified a large territory at risk of infarction. While CT suggested a cervical ICA occlusion, catheter angiogram identified the occlusion in the intracranial ICA segment. Slow proximal flow created the false appearance of a more proximal occlusion on non-invasive imaging. Successful recanalization (mTICI 2b, see Table A.4) was achieved with a single pass of a Solitaire$^{\mathrm{TM}}$stent retriever (Medtronic PLC, USA). Table 4.1 summarizes the patient's clinical details. Figure 4.3 shows relevant neuro-imaging studies, i.e., CT perfusion/structural images and angiograms, before and after mechanical thrombectomy. For this patient, MAP was recorded non-invasively at the beginning of the procedure, but eventually, an invasive catheter was inserted (radial artery) for continuous blood pressure monitoring during a portion of the procedure.

At the time of recanalization, a large increase in optically measured rCBF was observed

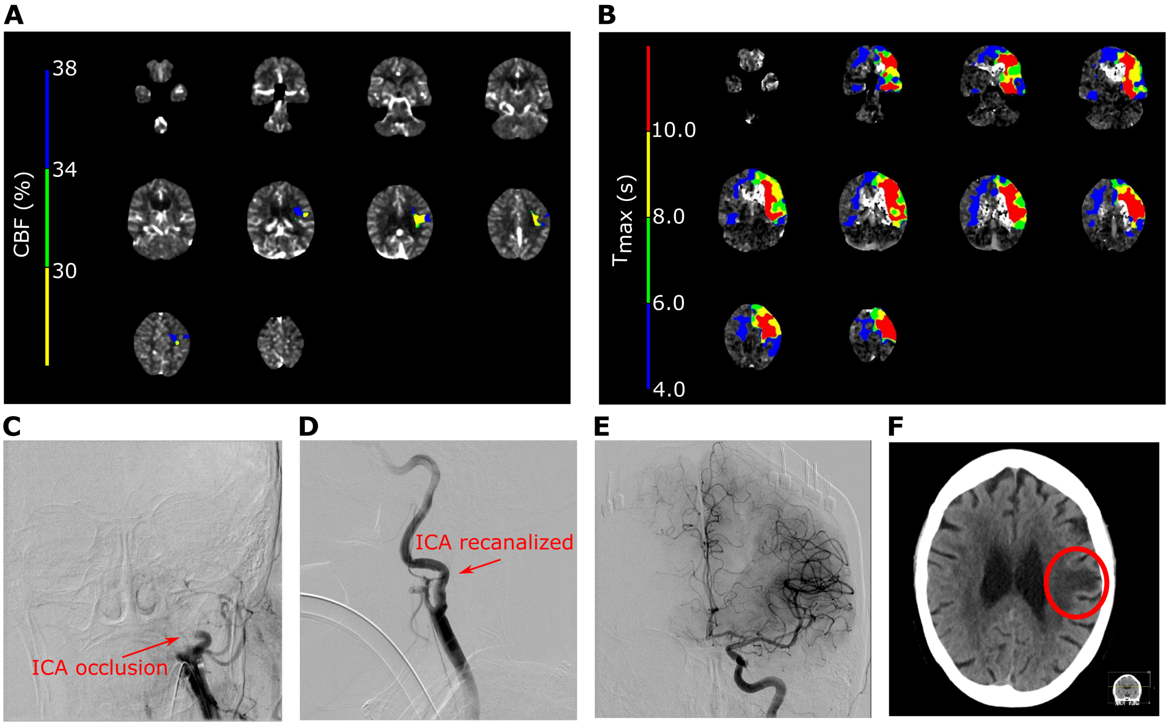

Figure 4.3: Imaging before and after mechanical thrombectomy (Patient 1). Baseline CT perfusion as analyzed by RAPID software (iSchemaView, Inc. Redwood City, CA) indicates (A) a small infarct core in the left hemisphere, as defined by Cerebral Blood Flow (CBF), lower than 30% of the contralateral values, and (B) a large penumbra, as defined by regions where the time to maximum (T_max) of the residue function obtained by deconvolution is higher than 6s. (C) Angiogram confirmed patency of left common carotid artery and occlusion of the internal carotid artery (ICA). After mechanical thrombectomy, an angiogram revealed (D) ICA recanalization, as well as (E) patent intracranial circulation. (F) Follow-up CT identified a small left lateral frontal lobe infarction (red circle). This figure was extracted from our previously published study [142].

in the affected hemisphere, with minimal change in extracerebral blood flow (Figure 4.4-A). After recanalization, despite a large MAP fluctuation (from 64 to 110 mmHg), CBF remained elevated, which could reflect intact autoregulatory mechanisms in the reperfused cerebral tissue. In the contralateral hemisphere, we also observed a transient increase in CBF at the time of recanalization, which returned to baseline after a few minutes (Figure 4.4-B). No complications occurred during mechanical thrombectomy. Patient 1 experienced near complete resolution of her neurologic deficits and she was discharged on hospital day 5 with an NIHSS of 1 (i.e., a minor stroke, Table A.3).

Patient 2 experienced several episodes of emesis and retching in the context of presumed gastroenteritis. Less than an hour following an episode of retching, the patient developed severe right-sided neck pain followed by acute onset left hemiplegia[2]. The pa-

---

[2] Hemiplegia is the same as hemiparesis, i.e., a paralysis of one side of the body.

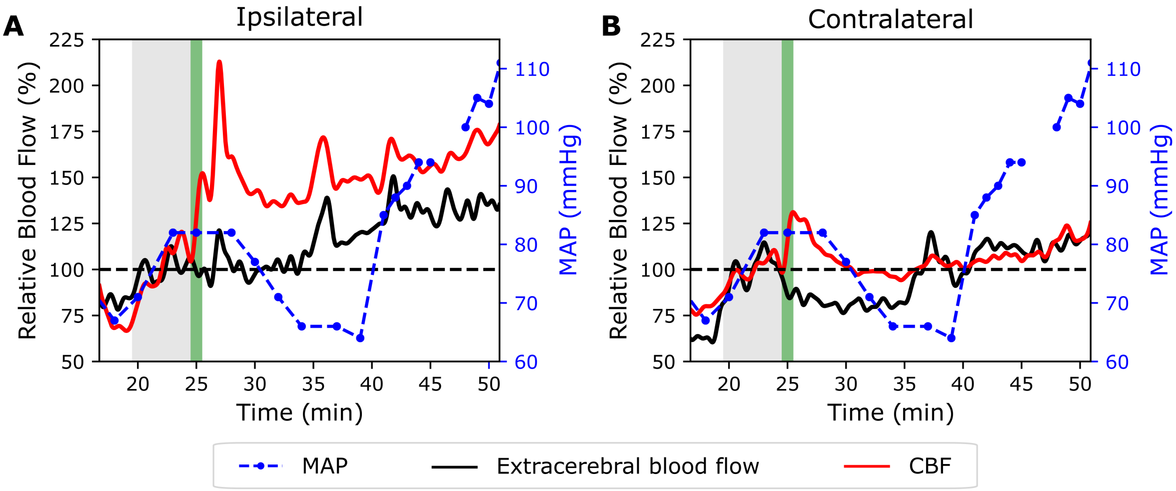

Figure 4.4: Hemodynamics of recanalization (Patient 1). Optical flow monitoring revealed a large and sudden increase in (A) ipsilateral CBF (red solid line, left axis) after recanalization (green bar); this sudden increase was not mimicked by the extracerebral tissue, which instead showed minimal blood flow changes at these times (black solid line, left axis). We also observed a smaller transient (B) contralateral CBF increase. Despite MAP fluctuations (blue dashed line, right axis), after recanalization CBF remained relatively stable on both sides. The grey shaded region represents baseline period. This figure was extracted from our previously published study [142].

tient presented with an NIHSS of 15 (i.e., a moderate to severe stroke, Table A.3) to the local emergency room. The patient was treated with intravenous thrombolysis and was transferred for consideration of mechanical thrombectomy. Upon arrival, the neurologic deficit was unchanged, and imaging revealed right cervical ICA occlusion with intact intracranial vasculature. Right hemisphere appeared to be filling via anterior communicating artery. The patient's clinical details are summarized in Table 4.1. Radiological imaging is presented in Figure 4.5. For this patient, MAP was non-invasively monitored by brachial cuff throughout the protocol. The decision was made to proceed with mechanical thrombectomy. Because of ICA dissection[3] and associated occlusion, the ICA was difficult to traverse, and after multiple attempts at angioplasty[4], an ICA stent was ultimately placed. There was no evidence of intracranial occlusion. When the ICA was first manipulated, there was a steep decline in MAP (124 to 66 mmHg), which was likely a consequence of carotid sinus disruption. This decline in MAP was accompanied by a bilateral decrease ($\sim$ 50%) in CBF and extracerebral flow (Figure 4.6). Blood pressure was then augmented pharmacologically; this increased contralateral flow but failed to improve blood flow on the side of the occlusion. Over the subsequent 15 minutes (prior to successful stent placement), blood flow in the affected hemisphere fluctuated dramatically.

---

[3] An arterial dissection is a tear in the lining of an artery.

[4] Angioplasty is a surgical repair or unblocking of a blood vessel.

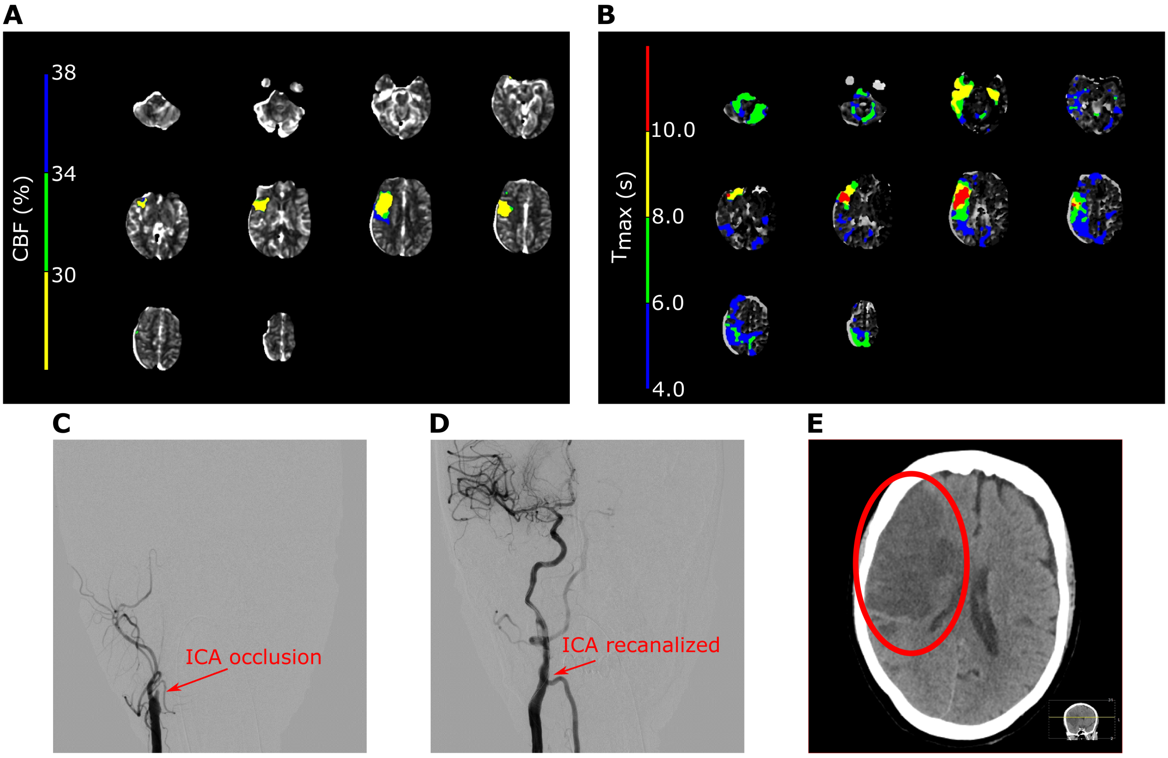

Figure 4.5: Imaging before and after mechanical thrombectomy (Patient 2). Baseline CT perfusion as analyzed by RAPID software (iSchemaView, Inc. Redwood City, CA) indicates (A) small-to-moderate infarct core in the right hemisphere, as defined by Cerebral Blood Flow (CBF) lower than 30% of the contralateral values, and (B) large penumbra, as defined by regions where the time to maximum ($T_{m}ax$) of the residue function obtained by deconvolution is higher than 6s. (C) Angiogram confirmed right cervical ICA occlusion, which was ultimately (D) recanalized after stent placement. (E) Follow-up CT identified a very large right hemispheric infarction (red circle). This figure was extracted from our previously published study [142].

More detailed inspection revealed that at times of low CBF, a near-total loss of pulsatile flow is apparent, along with intermittent periods of flow restoration. However, even with stable MAP on pressors, pulsatile flow in Patient 2 was not always maintained (Figure 4.7). At the time of stent placement, ipsilateral CBF continued to fluctuate for several minutes and slowly increased to almost 50% above the baseline value, despite stable MAP. Another spike in MAP was accompanied by a large CBF spike to almost double the baseline value. Notably, the intermittent loss of pulsatile flow was only seen in the ipsilateral CBF and was first instigated by the significant decrease in MAP prior to recanalization (Figures 4.6 and 4.7).

Immediate follow-up head CT showed evolved right hemispheric infarction along with patchy hyperdensity throughout the hemisphere. This is suggestive of a combination of contrast extravasation and some component of hemorrhage. The patient's final infarct

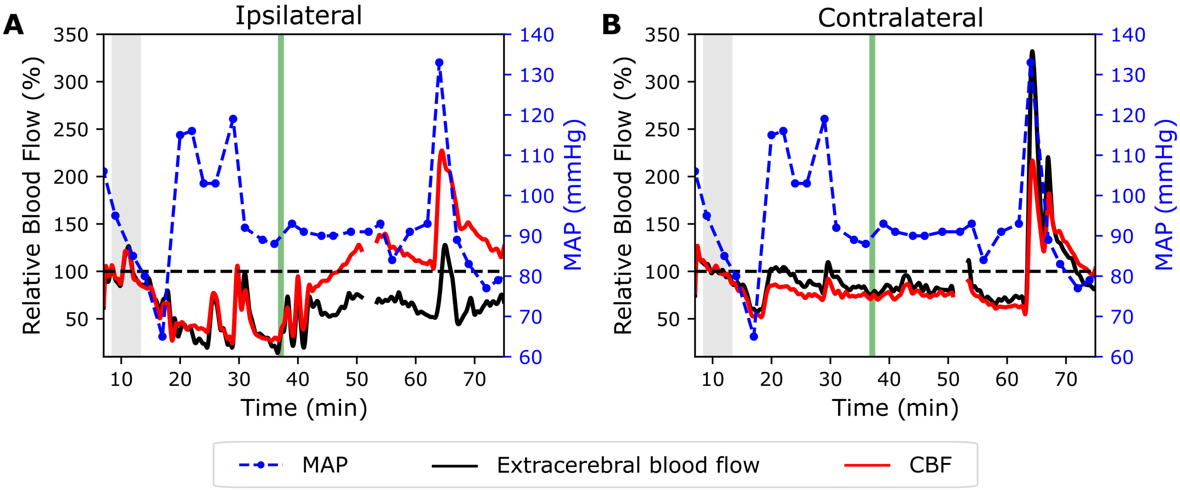

Figure 4.6: Hemodynamics of recanalization (Patient 2). Optics revealed a large and gradual increase in (A) ipsilateral CBF (red solid line, left axis) after recanalization (green bar), with minimal (B) contralateral CBF and extracerebral blood flow (black solid line, left axis) changes (black solid line, left axis). Prior to recanalization, a large drop in MAP (blue dashed line, right axis) was accompanied by a bilateral decrease (50%) in CBF and extracerebral flow. Blood pressure was augmented pharmacologically, which resulted in an increase in contralateral flow but failed to improve flow on the side of the occlusion. Grey shaded region represents the baseline period. This figure was extracted from our previously published study [142].

burden was very large, with associated edema and mass effect, necessitating decompressive hemicraniectomy[5] on hospital day 3. She was eventually discharged to a rehabilitation facility on hospital day 24, with an NIHSS of 17 (i.e., a moderate to severe stroke, Table A.3).

---

[5] Hemicraniectomy is a surgical procedure where a large flap of the skull is removed to decrease intracranial pressure.

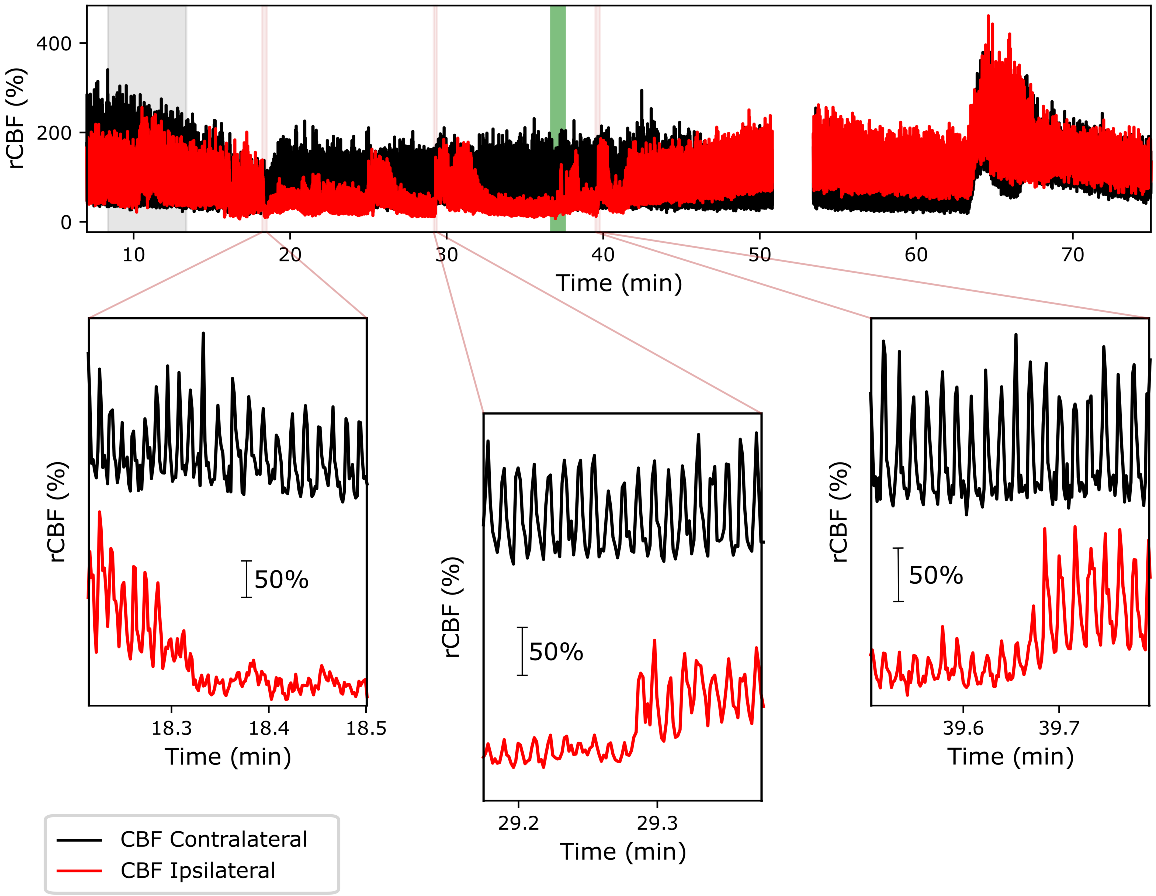

Figure 4.7: CBF heart-rate pulsatility during mechanical thrombectomy. Ipsilateral (red) and contralateral (black) CBF changes from Patient 2, before f]ltering. The Top panel shows CBF changes across the whole experiment. The green bar indicates the time of recanalization, and the grey shaded region indicates the baseline period. Each of the three bottom panels exhibits fast (without filtering) time variation in one of the three red shaded regions. These scaled zoomed-in versions of ipsilateral and contralateral CBF were separated to show the difference in heart-rate pulsatility across the different hemispheres and time. This figure was extracted from our previously published study [142].

4.3 Discussion

In this proof-of-concept study, we employed a noninvasive, contrast-free optical technique to monitor frontal lobe hemodynamics at the bedside during mechanical thrombectomy. To help distinguish between extracerebral and intracerebral blood flow changes, we obtained data from short (0.7 cm) and long (2.5 cm) source-detector separations. In two patients with cervical ICA occlusion, we measured an increase in ipsilateral CBF after recanalization while detecting no significant changes in extracerebral flow. A more detailed inspection of the CBF temporal response to mechanical thrombectomy revealed two distinct hemodynamic responses which were associated with divergent clinical outcomes.

Note, the DCS signal has contributions from arterial, capillary, and venous compartments. If cerebral blood volume is not transiently changing, the total blood flow in each vascular compartment is equal, and the precise compartmental contributions will not influence the measurement. When blood volume is transiently changing, DCS is more sensitive to arterial contributions [26, 126].

Patient 1 experienced a large and sudden increase in CBF after recanalization, which was sustained over the remainder of the monitoring period (~ 25 min). Notably, after recanalization, CBF remained elevated despite a large MAP fluctuation (between 64 and 111 mmHg), perhaps reflecting intact cerebrovascular autoregulation. Although it is often assumed that stroke impairs autoregulation [183], this assumption may not be true for all brain regions or for all patients [184] and may be affected by anesthetic drug and procedure factors [185]. In Patient 1, the large and sustained increase in CBF, and the apparent intact autoregulation, likely reflects the hemodynamics of effectively salvaged tissue. In fact, in a short interval follow-up, this patient made a quick and near-complete recovery with a very small final infarct burden. This result suggests that continuous monitoring of CBF with diffuse optics may facilitate individualized blood pressure goals aimed at optimizing CBF.

Interestingly, at the time of ICA recanalization in Patient 1, a transient increase in contralateral CBF was also observed. Prior to recanalization, this patient was perfusing the left hemisphere via the right carotid system with right-to-left flow through a patent anterior communicating artery. It is conceivable that this creates a “steal” phenomenon, in which blood flow to the unaffected right hemisphere is reduced. After recanalization, right to left flow through the anterior communicating artery is reduced and CBF in the right hemisphere increases. Additionally, some of this change could be related to MAP, which was elevated around the time of recanalization, and subsequently decreased ~ 5 minutes following recanalization.

In Patient 2, we observed a more gradual increase in CBF after recanalization, along with intermittent loss of pulsatile flow as seen by our fast DCS module on the ipsilateral hemisphere, but not the contralateral hemisphere (Figure 4.7). In fact, the initial loss of pulsatile flow coincided with a decline in MAP. These observations may indicate microvascular collapse in a low-flow state, perhaps enhanced by early infarct-related edema or elevated vasomotor tone of smooth muscle in arterioles [26]. Interestingly, with MAP augmentation, there was intermittent restitution of pulsatile flow. However, pulsatile flow was not well sustained, and even with ICA recanalization, we did not detect sudden increases in CBF, perhaps reflective of persistent microvascular dysfunction. These observations highlight another potentially valuable application of these bedside optics, i.e., to cases wherein the angiographic appearance of large vessel recanalization fails to adequately describe the hemodynamic state of the tissue. Identification of microvascular impairment after recanalization could enable clinicians to identify patients experiencing “no-reflow”, which has long been a nebulous and challenging clinical phenomenon that is associated with morbidity and mortality [186, 187].

In the case of Patient 2, the microvascular perturbation occurred in a patient that ultimately suffered a very large infarction. It is not clear if the microvascular impairment led to infarct expansion, or if the flow impairment was a consequence of the developing infarction. The temporal relationship of CBF with hypotension supports the former hypothesis, but conclusions should not be drawn from a single case. Ongoing studies will help to define the incidence of this discordance between large artery and microvascular flow and may identify additional hemodynamic patterns that occur with recanalization. Ultimately, the ability to non-invasively assess tissue reperfusion before and after recanalization may aid clinicians to more quickly assess treatment efficacy and concurrent physiologic management, such as blood pressure goals and head of bed angle.

It is also important to note that Patient 2 only achieved recanalization after extensive ICA manipulation, including multiple angioplasty attempts, and eventual ICA stenting. Some of the fluctuations before recanalization may reflect transient flow changes after balloon angioplasty, but we could not reliably synchronize the optical signal with every endovascular manipulation. In future studies, care will need to be taken to document endovascular manipulation in detail, as this may influence CBF or, equally important, may confirm that the hemodynamic changes are independent of endovascular manipulation. In this initial feasibility study, monitoring was limited to the interventional radiology suite, but continued monitoring in the ICU may present opportunities to further characterize post-recanalization stroke physiology in future work.

Variations in anesthetic depth impact cerebral metabolism and possibly influence outcome [188, 189], although clear clinical evidence of neuroprotection from anesthetics in cerebral ischemia has proven elusive [190]. Unfortunately, we could not determine anesthetic depth due to a lack of EEG monitoring during the procedure. Anesthetic dose may be abstracted from the anesthesia record, but it only crudely approximates the depth of anesthesia. Furthermore, it is challenging to draw any conclusions regarding the impact of cerebral metabolism changes due, in part, to limitations of steady-state modeling. Notably, both anesthesia and evolving ischemic conditions influence cellular metabolism, neither of which are static variables. Nevertheless, the observed sudden asymmetric changes in flow are not likely the effect of anesthesia, since anesthesia effects would likely be more diffuse.

One limitation of DCS is that hair can disrupt the DCS signal and delay probe placement; thus, measurements in this study were restricted to anterior frontal lobe. Given this limitation, care was taken to place the probes on the lateral aspect of the forehead. In this position, diffuse optics likely measures a combination of ACA and MCA flow, rather than exclusively MCA flow. This situation presents less of a problem for patients with ICA occlusion, but it may be an important consideration when monitoring patients with MCA occlusion in whom we expect reduced sensitivity to parenchymal changes. CT perfusion imaging that is now routinely obtained in acute stroke patients may help identify patients in whom flow impairment can be detected using frontally placed optical probes. Ultimately, with more reliable and rapid DCS systems capable of transcranial monitoring through hair, a more targeted placement of the optical probes over tissues of primary interest will be possible.

Similarly to the previous chapter (Chapter 3), a potential limitation of our study is the use of a SI homogenous medium tissue model for light transport, which may underestimate CBF changes [14, 17, 144, 166, 182]. Furthermore, light detected by the long source-detector separation is also sensitive to extracerebral changes, as these photons traverse the extracerebral tissues before reaching the intracerebral tissues. This could lead to erroneous interpretation of extracerebral blood flow changes as CBF changes. Nonetheless, by using multi-distance measurements, our results demonstrated that mechanical thrombectomy primarily affected CBF, as measured by the long source-detector separation, which is consistent with the underlying vascular anatomy and supports the notion that long DCS source-detector separations are primarily affected by cerebral tissue. In future studies, multi-layer approaches for DCS/DOS can and should be used to more carefully separate intracerebral and extracerebral blood flow changes (see Chapter 5 and [20, 166–172]). Calibration of CBF indices recovered from DCS would enable absolute comparison of CBF across subjects [23, 117, 141], but this is unlikely to affect the relative flow reported in this study if not coupled to multi-layer models.

4.4 Conclusions

We have demonstrated the feasibility of real-time monitoring of cerebral hemodynamics during mechanical thrombectomy. By measuring the frontal lobe microvascular hemodynamics with diffuse optics, it was possible to observe distinct perfusion profiles in two patients with divergent clinical outcomes. Although future studies in larger populations are clearly needed to better delineate application opportunities for DCS/DOS optical hemodynamic monitoring during mechanical thrombectomy, this pilot demonstration of diffuse optics shows promise for assessing the response to endovascular treatment and for guiding physiology-based therapy in this and other contexts.

Chapter 5

Improvement of the optical parameters recovered from diffuse optical spectroscopies

In Chapters 3 and 4, we employed a semi-infinite (SI) homogeneous model to recover the cerebral hemodynamics of neurocritical patients. However, as previously highlighted, the SI assumption may lead to erroneous interpretation of the cerebral physiology, as diffuse optical measurements are contaminated by extra-cerebral physiology. In this chapter, we propose the implementation of an improved model to recover the absorption and flow changes. More specifically, we propose the application of a two-layer model that attempts to separate the contributions from the extra-cerebral tissues (mainly scalp and skull) from the cerebral tissues. To test our two-layer model algorithm, we generated data in three different controlled environments: 1) forward-model simulations with noise; 2) simulations using the finite-elements method, and; 3) phantom experiments.

5.1 The two-layer model

We decided to use the two-layer model for a cylinder [53, 168–170, 191] as it is more computationally robust then the standard two-layer solution for a laterally unbounded medium [53, 170]. Specifically, we modeled the tissue as an infinitely thick cylinder with radius a, composed of two layers: a first layer with thickness ℓ, representing the extra-cerebral tissues, and; a second infinitely thick layer, representing the cerebral tissue (Figure 5.1). Although we restricted our discussion to the FD-DOS and DCS solutions, our results can be extended for time-domain measurements with a Fourier-transform of the solution presented below.

Briefly, by solving the FD-DOS diffusion equation (Equation 2.7) for the two-layer cylinder depicted in Figure 5.1, it is possible to show that the fluence in the k-th layer, Φ_k, can be written as [191]:

$$\Phi_k(\vec{r},\omega) = \sum_{n=1}^{\infty} G_k(s_n, z, \omega) J_0(s_n\rho) J_1^{-2}(a's_n), \tag{5.1}$$

where J_n are the Bessel functions of first kind and order n, s_n are positive roots of the 0-order Bessel function of first kind divided by $a' = a + z_b$ (i.e., $J_0(a's_n) = 0$), with $z_b = 2D_1(1+R_{eff})/(1-R_{eff})$, and R_{eff} is the fraction of photons that are internally diffusely reflected at the cylinder boundary. Since we generally measure using the reflection geometry (Figure 2.1), we are only interested in the fluence at the first layer, Φ_1. In this case, G_1 is defined as:

$$\begin{aligned} G_1(s_n, z, \omega) =& \frac{\exp\left(-\alpha_1|z-z_0|\right) - \exp\left(-\alpha_1(z+z_0+2z_b)\right)}{2D_1\alpha_1} \\ &+ \frac{\sinh\left(\alpha_1(z_0+z_b)\right)\sinh\left(\alpha_1(z+z_b)\right)}{D_1\alpha_1 \exp\left(\alpha_1(\ell+z_b)\right)} \\ &\times \frac{D_1\alpha_1 - D_2\alpha_2}{D_1\alpha_1\cosh\left(\alpha_1(\ell+z_b)\right) + D_2\alpha_2\sinh\left(\alpha_1(\ell+z_b)\right)}, \end{aligned} \tag{5.2}$$

where $\alpha_k = \sqrt{\frac{v\mu_{ak}}{D_k} + s_n^2 + \frac{i\omega}{D_k}}$ and $z_0 = 1/\mu'_{s1}$. Note that here we assumed that each layer have the same refractive index. To compute the diffusely reflected intensity (R), we used Fick's Law [53, 170]:

$$R(\vec{r}) = D_1 \frac{\partial}{\partial z}\Phi_1(\vec{r},\omega)\bigg|_{z=0}. \tag{5.3}$$

Finally, we can compute the theoretical amplitude (AC_{Theo}) and phase (Θ_{Theo}) with:

$$\begin{aligned} AC_{Theo} &= |R(\vec{r})| \\ \Theta_{Theo} &= \arg\left[R(\vec{r})\right]. \end{aligned} \tag{5.4}$$

Last, we can show that the DCS solution for a two-layer infinitely thick cylinder is formally identical to Equations 5.1 and 5.2, but with a different α_k:

$$\alpha_k = \sqrt{\frac{v\mu_{ak}}{D_k} + s_n^2 + \frac{\mu'_{sk}k_0^2F_k}{3D_k}\tau}, \tag{5.5}$$

where $k_0 = 2\pi/\lambda$ and F_k is the flow index in the k_{th} layer. Note that the DCS solution

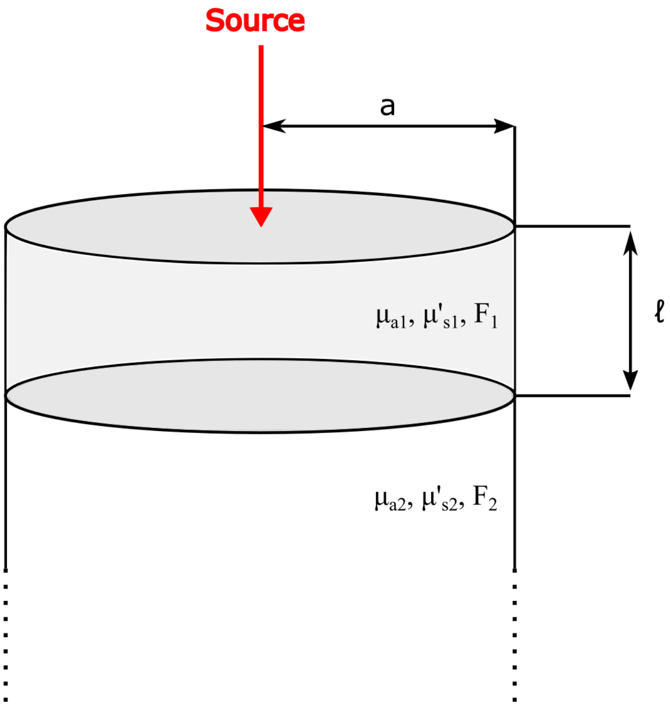

Figure 5.1: Pictorial representation of the two-layer geometry. We modelled the tissue as an infinitely thick cylinder with radius a, composed of two layers: a first layer with thickness ℓ, representing the extra-cerebral tissues, and; a second infinitely thick layer, representing the cerebral tissue. Each layer have different optical properties (μ_{ai}, μ'_{si}) and flow (F_i) .

depends in each layer's optical properties (μ_{a1}, μ_{a2}, μ'_{s1} and μ'_{s2}) as well as the flow in each layer (F_1 and F_2).

5.2 Methods

5.2.1 The fitting algorithm

To recover the optical properties of each layer from the FD-DOS data, we used a global optimizer implemented in Matlab (*fmincon*), which we found to be the algorithm less sensitive to the initial conditions. We attempted to minimize the following cost function, assuming N source-detector separations:

$$\begin{aligned}
\chi^2 =& \chi^2_{AC} + \chi^2_{\Theta} \\
\chi^2 =& \sum_{i=2}^{N} \left[\log\left(\frac{AC_{Theo}(\rho_i)}{AC_{Theo}(\rho_1)} \right) - \log\left(\frac{AC_{Meas}(\rho_i)}{AC_{Meas}(\rho_1)} \right) \right]^2 \\
&+ \sum_{i=2}^{N} \left[(\Theta_{Theo}(\rho_i) - \Theta_{Theo}(\rho_1)) - (\Theta_{Meas}(\rho_i) - \Theta_{Meas}(\rho_1)) \right]^2 ,
\end{aligned} \tag{5.6}$$

where AC_{Meas} and Θ_{Meas} are the measured amplitude and phase, respectively, and AC_{Theo} and Θ_{Theo} are the theoretical values from Equation 5.4. Here, we used the shortest source-detector separation ($i = 1$) as the amplitude and phase reference to avoid the necessity of computing two additional scaling factors. Additionally, since the amplitude decreases approximately exponentially with increasing source-detector separation, we opted to minimize the difference of the logarithm of the amplitude to reduce any potential biases to the shorter source-detector separations.

To better constraint our algorithm, we bounded the minimization algorithm between $0.01 \leq \mu_{ai}(cm^{-1}) \leq 0.4$ and $4 \leq \mu'_{si}(cm^{-1}) \leq 15$, where $i = 1, 2$ refers to the first and second layers, respectively. These limits were based on the expected values for the optical coefficients of an adult head [62]. Also, we assumed prior knowledge of the first layer thickness (ℓ) to recover the optical properties of each layer. Note that this assumption is not a limitation for neurocritical patients, as in these patients we will always have access to at least one type of structural brain imaging (such as CT or MRI), allowing direct measures of ℓ.

To recover the flow indexes (F_1 and F_2) from the DCS data, we minimized the squared difference of the theoretical and experimental auto-correlation functions, i.e.:

$$\chi^2_{DCS} = \sum_{\tau_i} \left(g_2^{(Theo)}(\tau_i) - g_2^{(Meas)}(\tau_i) \right)^2 . \tag{5.7}$$

In our fitting algorithm, we restricted the minimization algorithm to delay times in which $g_2(\tau) \geq 1.1$. To compute β from Siegert's relation [125], we used a SI model to fit the early portion of the auto-correlation curves (i.e., $g_2(\tau) > 1.2$), separately for each source-detector separation. In the DCS computations, we used the optical properties recovered with either a SI or two-layer model of the FD-DOS data, and we bounded our fitting algorithm to recover flow in the range $0.001 \leq F_i(10^{-8}\text{cm}^2/s) \leq 1000$, where $i = 1, 2$ refers to the first and second layers, respectively.

5.2.2 Forward-model simulations

To test the efficacy of our two-layer algorithm, we first generated data using the forward-model with varying optical properties. We randomly generated 150 curves with μ_{a1} and μ_{a2} varying between 0.05 and $0.2cm^{-1}$, and μ'_{s1} and μ'_{s2} varying between 7 and 12 cm^{-1}. We repeated the simulation three times, with different levels of noise, to simulate the experimental noise: 1) without noise; 2) 1% amplitude noise and 0.05^o phase noise, and; 3) 2% amplitude noise and 0.1^o phase noise. Note that in common experimental conditions, we expect approximately 2% amplitude noise and 0.1^o phase noise [170]. We generated amplitude and phase data for 20 source-detectors separations, equally divided between 0.8 and 4.6 cm.

5.2.3 Simulation using a finite-elements package

To test our algorithm in a more realistic scenario, we used an open-source package that uses the finite-elements method to simulate diffuse optical spectroscopy data (NIRFAST) [192, 193]. With this package, we generated a two-layered cube, with dimensions $20 \times 15 \times 15cm$ and with a node size of $0.15cm$. This was a compromise between the precision and the run-time of the simulation. We varied the absorption coefficient of the second layer (μ_{a2}) between 0.08 and $0.17cm^{-1}$, in steps of 0.01 cm^{-1}, with a fixed absorption coefficient in the first layer ($\mu_{a1} = 0.1cm^{-1}$) and with fixed scattering coefficients in both layers ($\mu'_{s1} = \mu'_{s2} = 8cm^{-1}$). We repeated the simulation three times, with different first layer thicknesses: ℓ = 0.8, 1.2 and 1.4 cm. Here, we also generated amplitude and phase data for 20 source-detectors separations, equally divided between 0.8 and 4.6 cm. However, to better match experimental conditions, we restricted our analysis to two different representative sets of 8 source-detector separations:

$$\begin{aligned} \rho_{Long} &= 0.8, 1.2, 1.6, 2.0, 2.8, 3.2, 3.6, 4.0 \text{ cm}, \\ \rho_{Short} &= 0.8, 1.2, 1.4, 1.8, 2.0, 2.2, 2.4, 3.0 \text{ cm}. \end{aligned} \tag{5.8}$$

5.2.4 Phantom measurements

To test our algorithm in a real environment, we also conducted a two-layer liquid phantom experiment. We developed a black acrylic aquarium capable of mimicking a two-layer geometry (Figure 5.2-A). To separate each layer, we used a thin plastic film attached to a black frame, and we used silicon glue to seal the frame edges. We have also attached a peristaltic pump to the aquarium, to induce flow changes in the second layer. To attach the optical fibers, we have drilled holes in one side of the phantom, such that the fibers were directly in contact with the liquid. The phantom allowed measurements with FD-DOS with 8 different source-detector separations (0.7, 1.2, 1.5, 1.7, 2.0, 2.2, 2.5, 3.0 cm), and DCS with 4 source-detector separations (0.8, 1.5, 2 and 2.5 cm). To avoid saturation of the shorter source-detector separations, we glued neutral-density filters in some of the optical fiber positions. In this experiment, we used the hybrid optical system developed at UNICAMP (see Section 3.1.3 for more details).

To calibrate the expected optical properties, we first conducted a semi-infinite measurement (i.e., without the thin plastic film). To this end, we used an initial solution composed of 4500ml of distilled water, 200ml of Liponfundin 20% and 2ml of an ink solution. The ink solution was composed of 0.5 ml of ink (Nankin, Acrilex) and 25ml of water. Then, we varied the absorption of the medium by multiple additions of 0.5ml of the ink solution.

For the two-layer experiment (Figure 5.2-B), we used a starting solution with the same initial concentrations used in the semi-infinite experiment. We fixed the first-layer thickness at $\ell = 1.2$ cm and varied the absorption of the second-layer by adding 0.5ml of a similar ink solution. In the two-layer experiment, after each addition of ink, we also changed the flow in the second layer by changing the flow output of the peristaltic pump, which was capable of outputting a maximum of 3L/min. After each flow and absorption change, we waited at least 6 minutes for the solution to stabilize.

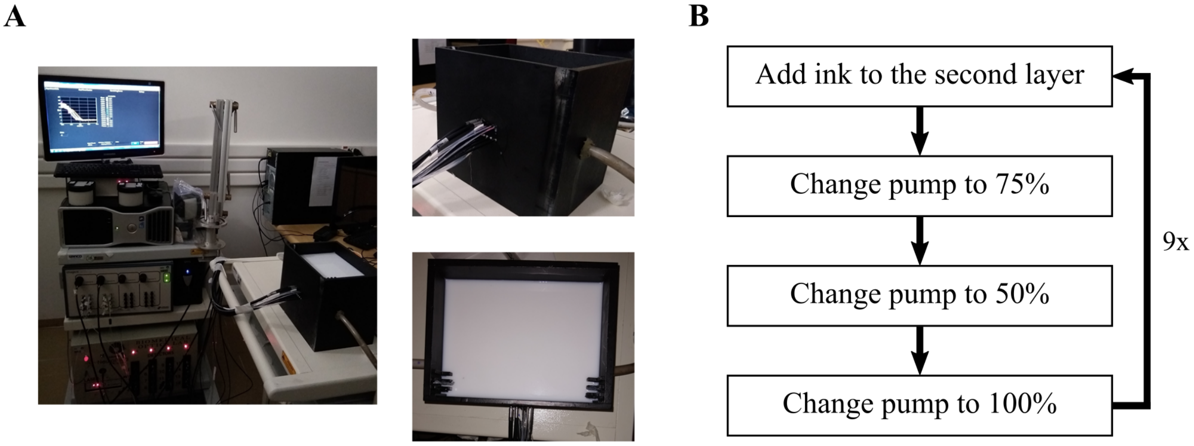

Figure 5.2: Experimental setup for the phantom measurements. (A) We used the system developed at UNICAMP (see Chapter 3), and developed a black acrylic aquarium capable of mimicking a two-layer geometry. In our two-layer experiment, we started with an initial solution composed of 4500ml of water, 200ml of a lipid emulsion (Lipofundin 20%), and 2ml of an ink solution (0.5 ml of ink and 25ml of water). (B) To simulate changes in the second layer, We varied the absorption by multiple additions of 0.5ml of the ink solution. After each ink addition, we have also changed the flow in the second layer by changing the flow output of a peristaltic pump. We repeated this process nine times.

5.3 Results

5.3.1 Forward-model

First, we tested our two-layer algorithm with the forward-model generated data (Section 5.2.2). For the simulations without noise, the algorithm was capable of precisely recovering all four optical coefficients (green points in Figure 5.3). However, when we tried to recover the optical properties in the two datasets with noise, we were unable to recover the scattering coefficient of the second layer (μ'_{s2}), independently of the noise level. However, the errors on μ'_{s2} did not seem to affect the accuracy in the recovery of the other three parameters: we were able to recover the absorption coefficient of both layers (μ_{a1} and μ_{a2}), as well as the scattering coefficient of the first layer (μ'_{s1}).

To understand our inability to recover the scattering of the second layer, we generated several amplitude and phase curves for a medium with $\ell = 1.2$ cm, with varying μ'_{s2} (between 5 and 15 cm^{-1}), but fixed $\mu'_{a1} = 0.1cm^{-1}$, $\mu_{a2} = 0.14cm^{-1}$ and $\mu'_{s1} = 8cm^{-1}$. As seen in Figure 5.4, even though we varied the scattering coefficient of the second layer across a wide range, we encountered minimal differences in the amplitude and phase values with source-detector separations up to 4.6 cm. Notably, the differences due to changes

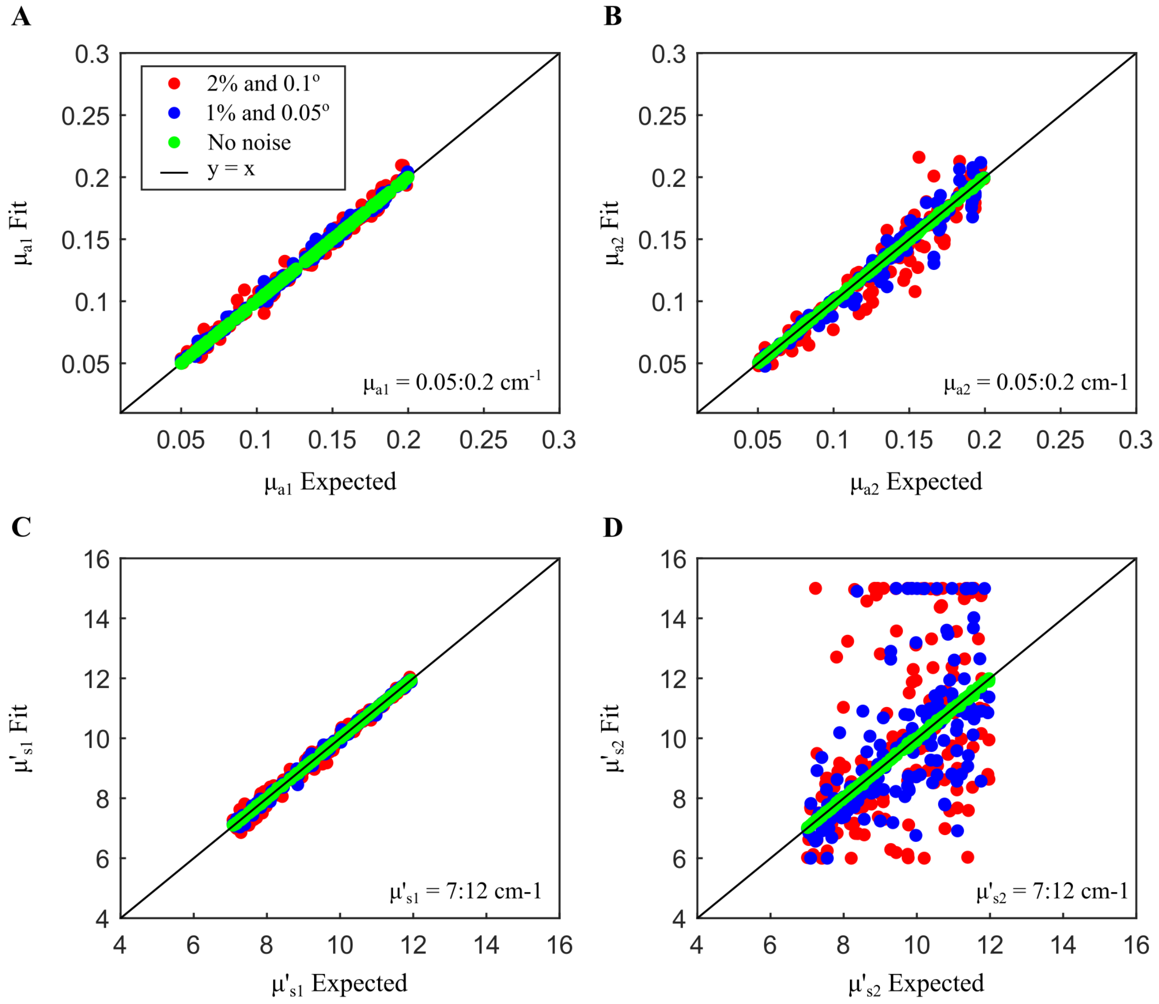

Figure 5.3: Results of the forward model simulations. Our two-layer algorithm was capable of recovering the (A) absorption coefficient in the first, (B) the absorption coefficient in the second layer, as well as the (C) scattering coefficient of the first layer, independently of the noise level. However, although we were able to recover the (D) scattering coefficient of the second layer for the case without noise, we were unable to accurately recover μ'_{s2} for the simulations with noise. Note that the errors on μ'_{s2} did not seem to affect our accuracy in the recovery of the other three parameters.

in μ'_{s2} were on the same order of the expected noise. Since we are not sensitive to the scattering coefficient of the second layer (μ'_{s2}), we assumed that the scattering coefficients of the first and second layers are equal (i.e., $\mu'_{s1} = \mu'_{s2} = \mu'_{s}$). This assumption, although arbitrary, improves the recovery of optical properties as it allows our algorithm to fit for one less parameter. Note that we do not expect errors in μ'_{s2} to affect the recovery of the other parameters (Figure 5.3).

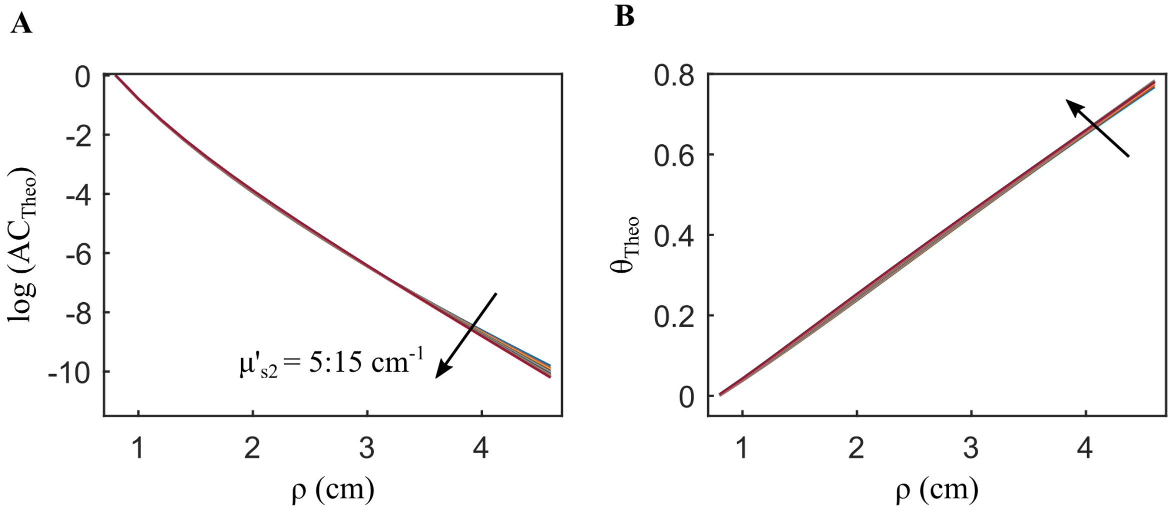

Figure 5.4: Theoretical (A) amplitude (AC_{Theo}) and (B) phase (Θ_{Theo}) values simulated for source-detector separations between 0.8 and 4.6cm. We varied scattering coefficient in the second layer (μ'_{s2}) between 5 and 15 cm^{-1}, and fixed the absorption coefficient at 0.1 cm^{-1} and 0.14 cm^{-1}, for the first second layers, respectively. We also fixed the scattering coefficient of the first layer at 8 cm^{-1}, and the first layer thickness was 1.2 cm.

5.3.2 Simulation using a finite-elements package

To further test our algorithm, we also tried to recover the optical properties in a set of simulations using the NIRFAST package. To quantify the recovery error on each optical parameter, we calculated the relative error, which is defined as:

$$\text{Relative Error} = \frac{X_{Meas} - X_{Expected}}{X_{Expected}}, \tag{5.9}$$

where X_{Meas} and $X_{Expected}$ are the measured and expected optical coefficients. First, we attempted to recover the optical properties using the shorter set of source-detector separations, ρ_{Short} (Equation 5.8). In this case, we were able to recover all three optical properties, for all three layer thicknesses, with relative error of approximately: -0.4% for μ_{a1}, -10.6% for μ_{a2}, and 6.2% for μ'_s (Figure 5.5). When using the longer source-detector separations (ρ_{Long}), we were able to recover slightly better results for the absorption in the second layer, for all three layer thicknesses, with relative errors of approximately -8.5% for μ_{a1}, 2.5% for μ_{a2}, and 7.6% for μ'_s (Figure 5.6).

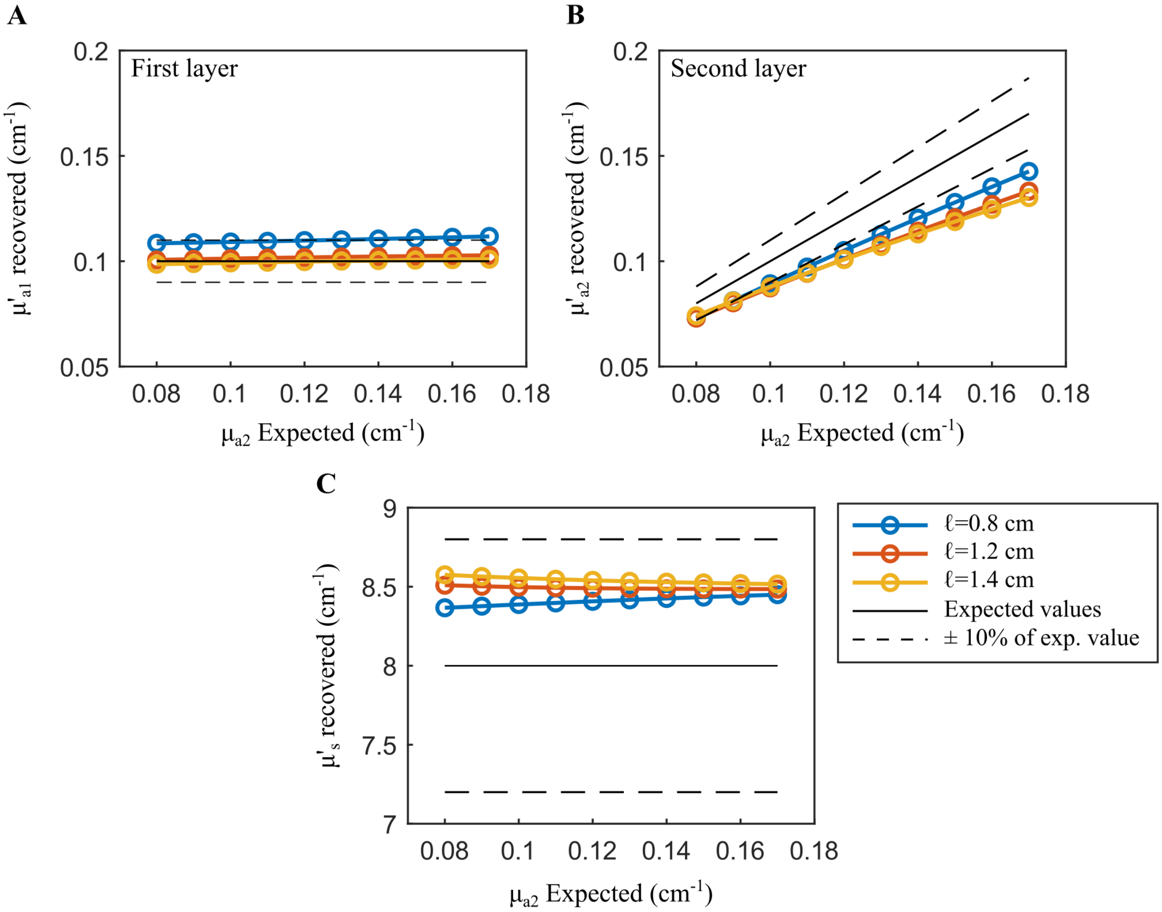

Figure 5.5: Results of the NIRFAST simulations with the shorter set of source-detector separations (ρ_{Short}). By assuming that the scattering coefficient of the first and second layer are equal ($\mu'_{s1} = \mu'_{s2} = \mu'_{s}$), we were able to recover within $\sim 10\%$ of the expected values (A) the absorption coefficient of the first layer (μ_{a1}), (B) the absorption coefficient of the second layer, as well as (C) the scattering coefficient (μ'_{s}).

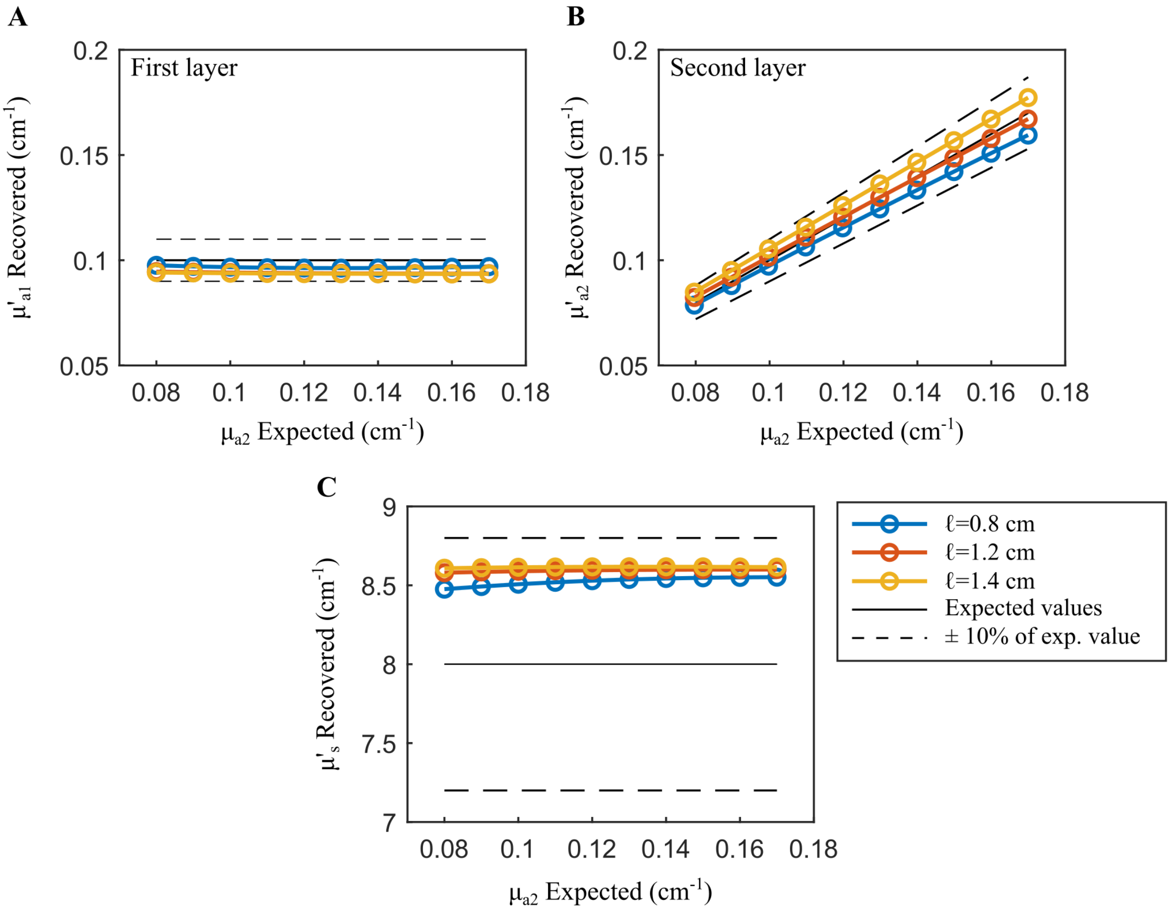

Figure 5.6: Results of the NIRFAST simulations with the longer set of source-detector separations (ρ_{Long}). By assuming that the scattering coefficient of the first and second layer are equal ($\mu'_{s1} = \mu'_{s2} = \mu'_s$), we were able to recover with errors $< 10\%$ (A) the absorption coefficient of the first layer (μ_{a1}), (B) the absorption coefficient of the second layer, as well as (C) the scattering coefficient (μ'_s).

5.3.3 Phantom experiments

Last, we validated our two-layer algorithm to recover the optical properties in a more realistic experiment using a liquid phantom. In order to recover a single value of μ_{a1}, μ_{a2} and μ'_s for each step of ink addition, we averaged the amplitude and phase data across all changes in pump flow. In Figure 5.7, we show the values recovered from the two-layer model compared to the expected values recovered from the semi-infinite experiment for the 690 nm wavelength. In agreement with the results from Figure 5.5, that used similar source-detector separations, we were able to recover all the optical properties of each layer within 10% of the expected values (Figure 5.7). Although the correct trend in the absorption values was recovered from the two layer phantom using a SI model, the absolute values for the second layer were underestimated.

To test the two-layer model for DCS, we also changed the flow in the second layer of the phantom. In our initial attempt, we tried to recover the flow indexes from each layer (F_1 and F_2) using the optical properties recovered by fitting the FD-DOS data with a SI model, i.e., we assumed that $\mu_a^{(SI)} = \mu_{a1} = \mu_{a2}$ and $\mu_s'^{(SI)} = \mu'_{s1} = \mu'_{s2}$. We used all four DCS source-detector separations (0.8, 1.5, 2.0 and 2.5 cm) simultaneously to recover

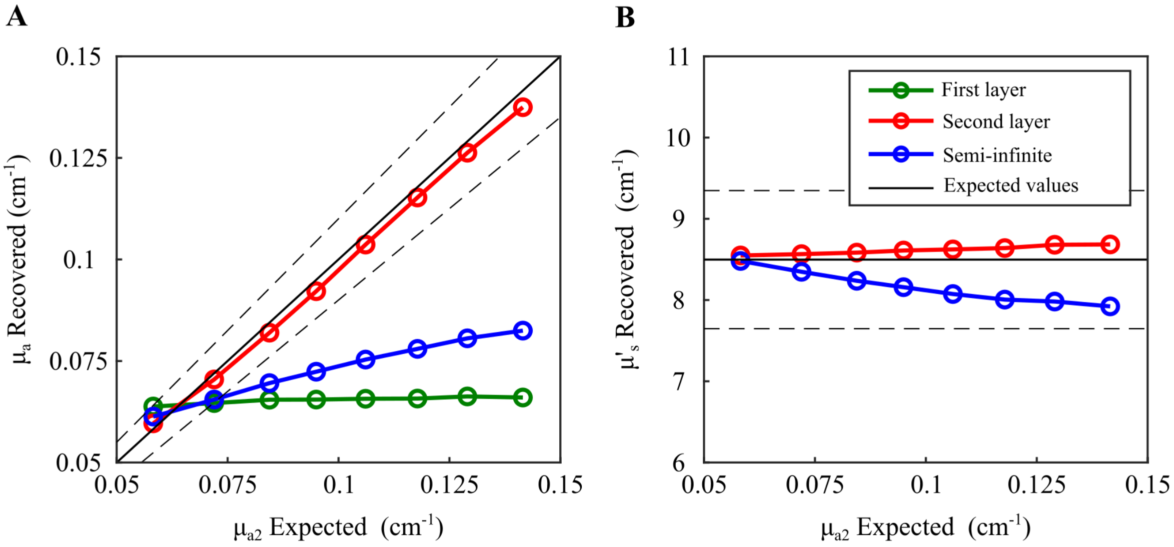

Figure 5.7: Optical coefficients recovered from the two-layer phantom experiment. By employing the two-layer model, we recovered the (A) absorption coefficients and (B) scattering coefficients from each layer of our phantom experiment. We accurately recovered the increasing absorption coefficients in the second layer (μ_{a2}, red curve), and a stable absorption coefficient in the first layer (μ_{a1}, green curve), and a stable scattering coefficient. Note that we assumed an equal scattering coefficients for both layers ($\mu'_s = \mu'_{s1} = \mu'_{s2}$). We also show the values recovered using a SI model for the two-layer phantom data (blue curves). The expected values were calibrated with a SI phantom measurement.

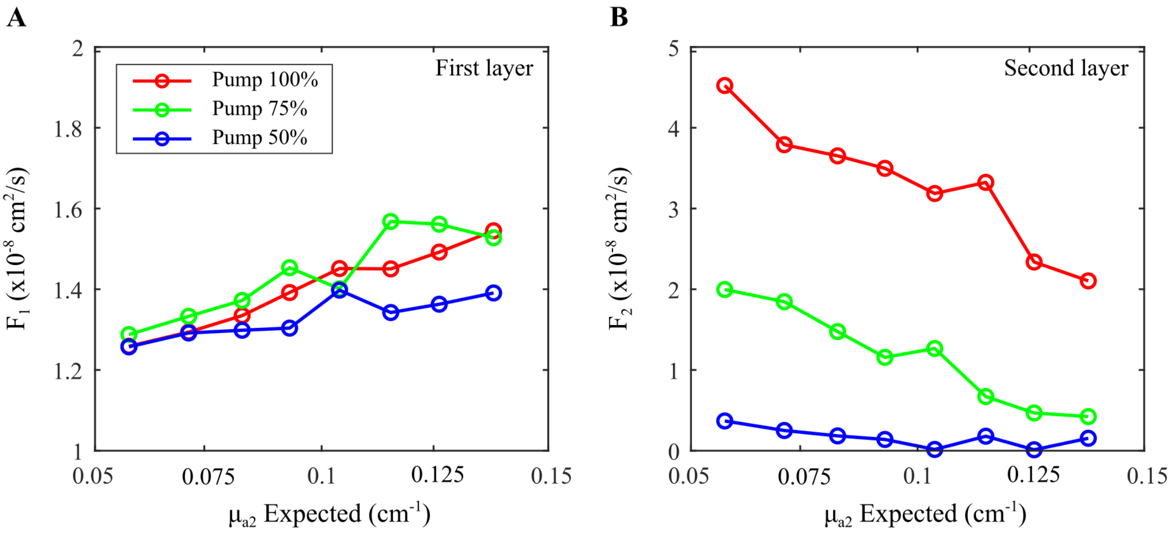

Figure 5.8: Flow recovered from the two-layer phantom experiment using a two-layer model for DCS, and a SI model for FD-DOS. We found (A) an increase in the first layer flow (F_1), and (B) a decrease in the second layer flow (F_2), with increase absorption for each pump flow.

the flow indexes. As seen in Figure 5.8, although we expected similar flow across the different pump states, we measured an increase in F_1 and a decrease in F_2 with increasing μ_{a2}. Thus, by not properly accounting for the absorption differences between the first and second layers, we introduced systematic errors in the recovery of the flow indexes.

Then, we tried to fit the DCS data using the two-layer optical properties obtained with FD-DOS (i.e., μ_{a1}, μ_{a2} and $\mu_s' = \mu_{s1}' = \mu_{s2}'$). To better match common experimental conditions, we also restricted our fitting algorithm to use only the shortest (0.8 cm) and longest (2.5 cm) DCS source-detector separations. To reduce the number of parameters in the two-layer algorithm for DCS, we first recovered the blood flow index of the first layer (F_1) using the shortest DCS separation and the first layer optical properties (μ_{a1} and μ_s') as input to a SI model. For first-layer thicknesses larger than 1 cm, which is the case for an adult head, a 0.8 cm source-detector separation is only sensitive to the first layer, and thus a SI model suffices to recover F_1. Then, to estimate F_2, we used the long DCS source-detector separation, the F_1 recovered from the short DCS separation and the two-layer optical properties obtained with FD-DOS as input to the two-layer model for DCS.

With this method, as seen in Figure 5.9-A, we recovered F_1 values that were independent of the changes in absorption and flow of the second-layer, as expected. Furthermore, we also recovered F_2 values that were independent of the absorption changes in the second-layer (Figure 5.9-B). More precisely, when the pump was at 100%, we ob-

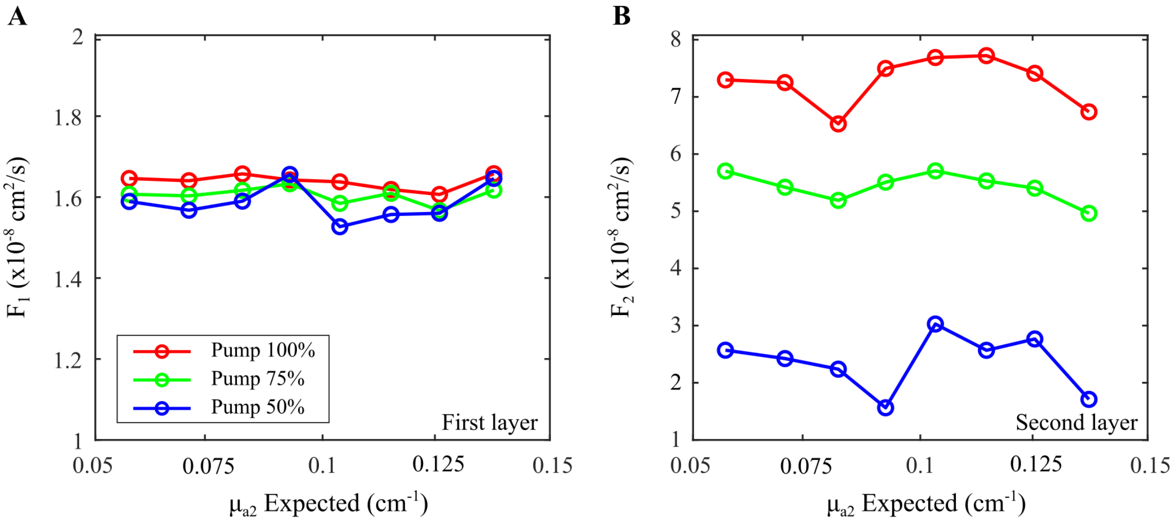

Figure 5.9: Flow recovered using the two-layer model for both DCS and FD-DOS. We found (A) a stable flow in the first layer (F_1), regardless of the absorption and flow changes in the second layer. (B) The recovered flow values from the second layer (F_2) were independent of the absorption changes, and were consistent with the expected changes due to the pump flow changes.

tained $F_2 = (7.1 \pm 0.5) \times 10^{-8} cm^2/s$, while for the pump at 75% we obtained: $F_2 = (5.3 \pm 0.3) \times 10^{-8} cm^2/s$. When comparing the values between the pump at 100 and 75%, we obtained a relative difference in flow of $(75 \pm 5)\%$, as expected. When the pump was 50%, we obtained $F_2 = (2.3 \pm 0.5) \times 10^{-8} cm^2/s$, and encountered a relative change of $(32 \pm 7)\%$, when comparing with the pump at 100%.

5.4 Discussion and Conclusions

In this study, we validated a two-layer model for FD-DOS to recover the optical properties in three different controlled environments. First, we showed that FD-DOS measurements with source-detector separations up to 4.6 cm are not sensitive to the scattering coefficient of the second layer. Then, by assuming that the scattering coefficients of the first and second layers are equal, we showed that it is possible to recover the optical properties as well as the flow indexes from each layer with approximately 10% error. As mentioned in the previous chapters, in the diffuse optics literature the most common approach for data analysis has been the SI model. However, as seen in Figure 5.7, the SI assumption may lead to underestimation of the true changes from the second-layer. Nonetheless, although the SI model underestimates the changes in the second-layer, a simplistic SI assumption can still recover the correct trends of physiological changes. Thus, although the two-layer model certainly improves the results presented in the previous chapters, it does not invalidate the results obtained with the SI model.

Unfortunately, we are unable to apply the two-layer method presented in this current chapter to the results from the previous chapters. To accurately measure the two-layer optical properties from FD-DOS with a single modulation frequency, we need at least 8 source-detector separations [53, 170], but in Chapter 3 we were restricted to four source-detector separations for FD-DOS. However, we measured three source-detector separations for DCS, and thus we could use a two-layer model for the DCS data, but not for FD-DOS data. To check whether using a two-layer model only for DCS would improve the accuracy in the recovery of the flow changes, we tested our two-layer algorithm for DCS using a SI model for FD-DOS. However, as seen in Figure 5.8, this still resulted in the misinterpretation of absorption changes as flow changes. Thus, to properly improve the reliability of the diffuse optical measurements of cerebral physiology, we need to account for the layer differences of both the optical coefficients and the difference in flow.

It is worth noting a few limitations of the study presented in this chapter. First, we did not simulate data for DCS, as currently this is not implemented in NIRFAST; a DCS simulation could allow us to estimate the error in the absolute flow estimates. Additionally, the two-layer model is still not a perfect model, as the extra-cerebral tissues are highly heterogeneous; for example, we expect different optical properties for the scalp and the skull [62]. However, more complex models (such as a three-layer model [167, 168]) requires extra parameters, which will further complicate the recovery algorithms. In future studies, by simulating a realistic head with NIRFAST it may be possible to estimate the errors introduced by a heterogeneous first-layer for different models. Nonetheless, although simplistic, our two-layer approach for DOS and DCS already has the potential to improve the reliability of cerebral hemodynamic monitoring with diffuse optics over the traditional SI methods.

Chapter 6

Summary and Perspectives

The main goal of this work was to show that diffuse optics can aid in *real-time* monitoring of cerebrovascular diseases. To this end, we first developed and translated a hybrid diffuse optical system to a neuro intensive care unit (neuro-ICU) of a public hospital in Brazil ('Hospital de Clínicas', University of Campinas). Our hybrid system combined FD-DOS and DCS to monitor cerebral oxygenation and cerebral blood flow in real-time. To facilitate its use by clinical personnel, we developed a user-friendly graphical user interface based on current clinical monitors already in the neuro-ICU. The pilot study presented in Chapter 3 showed that diffuse optics may provide supporting information for monitoring secondary damage in neurocritical patients, with minimal interference with standard clinical practices. The optically-derived hemodynamic parameters provided neurophysiological information at the microvasculature level which was consistent with the patient clinical outcome.

Then, we reported in Chapter 4 a pilot study that demonstrates the feasibility of real-time monitoring of cerebral blood flow hemodynamics during mechanical thrombectomy. We reported two cases of patients with internal carotid artery occlusions that underwent mechanical thrombectomy at the Hospital of the University of Pennsylvania. By measuring the frontal lobe microvascular hemodynamics with diffuse optics, it was possible to observe distinct reperfusion profiles for patients with divergent clinical outcomes. Our results suggest that cerebral hemodynamic monitoring with diffuse optics hold potential for assessing the response to endovascular treatment of stroke. Taken together, the results from Chapters 3 and 4 showed that diffuse optics is a promising monitoring tool for guiding physiology-based therapy in neurocritical patients. Thus, the translation of diffuse optics to clinical settings may positively impact clinical care and patient outcome, and may be especially useful in low-budget hospitals and in remote areas, where cerebral physiology monitoring is essential but not readily available.

Last, we also proposed the implementation of a two-layer model to separate the extra-cerebral and cerebral contributions to the optical signal. We showed that it is possible to recover the optical properties and flow from the first and the second layer of our model (representing the extra-cerebral and cerebral layers, respectively) within $\sim$10% error. This is more accurate than what is currently reported in the literature. Additionally, we showed that a simplistic SI model underestimates the true cerebral changes, and that by not accounting for the layer differences in the optical properties one may misinterpret absorption changes as flow changes. This is especially relevant for neurocritical patients, where the cerebral oxygenation and CBF may be independently changing.

There are few possible steps that could further improve the results presented in this thesis. First, to show that diffuse optics can positively impact patient outcome, a larger longitudinal validation study in the clinic is necessary. Here, we focused on case-reports to assess whether diffuse optics is sensitive to the individual physiology of the patients; however, no conclusions should be drawn from case-studies. Additionally, the development of new optical probes capable of measuring through hair is still lacking. Although measurements in the forehead may be useful for diseases with a global cerebral response, a targeted placement of the optical probes over a region of interest may be more informative. For example, by using a neuro-navigator system, physicians could place the optical probes directly over the penumbra in ischemic stroke patients, potentially improving the sensitivity of diffuse optics to the salvageable tissues. By directly measuring the penumbra, clinicians could develop specific therapeutic interventions based on the individual's physiology, which has the potential to positively impact clinical care and patient outcome.

From the modeling perspective, the two-layer model proposed in Chapter 5 is still a simplistic approximation, as it does not take into account the heterogeneous structure of the extra-cerebral tissues. To this end, a comparison of the two-layer model with more complex models, such as a three-layer model [167] is advisable. However, the increase in the number of free parameters could decrease the robustness of more complex models. By simulating realistic head geometries (e.g. using the NIRFAST package) it may be possible to assess the efficacy of the two-layer model as well as other more complex models. Additionally, by comparing the results from *in vivo* diffuse optical studies with other gold-standard measurements of cerebral hemodynamics (such as ASL), it may be possible to estimate the experimental uncertainties of the two-layer model [23].

Appendix A

Description of the clinical scales

Table A.1: Description of the Hunt & Hess grade scale and associated mortality rate [148].

Grade	Criteria	Mortality rate
I	Asymptomatic, mild headache, slight nuchal rigidity	30%
II	Moderate to severe headache, nuchal rigidity, no neurologic deficit other than cranial nerve palsy	40%
III	Drowsiness, confusion, mild focal neurologic deficit	50%
IV	Stupor, moderate-severe hemiparesis	80%
V	Coma, decerebrate posturing	90%

Table A.2: Description of the Fisher grade scale and associated risk of vasospasm [149].

Grade	Blood on CT	Risk of vasospasm
I	No SAH* detected	Low (0-21%)
II	Diffuse or vertical layer of subarachnoid blood <1mm thick	Low (0-25%)
III	Localized clot and/or vertical layer within the subarachnoid space >1mm thick	Low to high (23-96%)
IV	ICH or IVH with diffuse or no SAH*	Low to moderate (0-35%)

*SAH: Subarachnoid hemorrhage; ICH: Intracerebral hemorrhage; IVH: intravertricular hemorrhage.

Table A.3: National Institute of Health Stroke Scale (NIHSS) scores and associated stroke severity [150].

Score	Stroke severity
0	No stroke symptoms
1–4	Minor stroke
5–15	Moderate stroke
16–20	Moderate to severe stroke
21–42	Severe stroke

Table A.4: Modified treatment in cerebral ischemia scale grade definition (mTICI) [175, 176].

Grade	Definition
0	No perfusion
1	Antegration reperfusion past the initial occlusion, but limited distal branch filling with little or slow distal reperfusion
2a	Antegrade reperfusion of less than half of the previously occluded target artery ischemic territory
2b	Antegrade reperfusion of more than half of the previously occluded target artery ischemic territory
3	Complete antegrade reperfusion of the previously occluded target artery ischemic territory, with absence of visualized occlusion in all distal branches

Appendix B

Ethics committee approval letter

PARECER CONSUBSTANCIADO DO CEP

DADOS DA EMENDA

Título da Pesquisa: Desenvolvimento de Instrumentação e Metodologias para Monitoramento da Oxigenação, Fluxo Sanguíneo e Metabolismo Cerebral com Espectroscopias Ópticas de Difusão

Pesquisador: Rickson Coelho Mesquita

Área Temática:

Versão: 3

CAAE: 56602516.2.0000.5404

Instituição Proponente: Instituto de Física "Gleb Wataghin"

Patrocinador Principal: Financiamento Próprio

DADOS DO PARECER

Número do Parecer: 1.909.944

Apresentação do Projeto:

Emenda ao projeto original, com a seguinte justificativa:

"Trata-se de uma emenda que visa exclusivamente adicionar 3 alunos relacionados com a aquisição e análise de dados à equipe do projeto (Sérgio Luiz Novi Júnior, Doutorado; Andrés Fabián Quiroga Soto, Doutorado; Alex de Castro Carvalho, IC). Todos os detalhes relacionados com a pesquisa foram mantidos em relação ao projeto aprovado."

Objetivo da Pesquisa:

Mantidos em relação ao projeto original.

Avaliação dos Riscos e Benefícios:

Mantidos em relação ao projeto original.

Comentários e Considerações sobre a Pesquisa:

Solicitação de inclusão de novos pesquisadores ao projeto.

Considerações sobre os Termos de apresentação obrigatória:

Formulário Plataforma Brasil foi adequadamente preenchido e a emenda devidamente justificada.

Recomendações:

Conclusões ou Pendências e Lista de Inadequações:

Emenda aprovada.

Considerações Finais a critério do CEP:

- O sujeito de pesquisa deve receber uma via do Termo de Consentimento Livre e Esclarecido, na íntegra, por ele assinado (quando aplicável).

- O sujeito da pesquisa tem a liberdade de recusar-se a participar ou de retirar seu consentimento em qualquer fase da pesquisa, sem penalização alguma e sem prejuízo ao seu cuidado (quando aplicável).

- O pesquisador deve desenvolver a pesquisa conforme delineada no protocolo aprovado. Se o pesquisador considerar a descontinuação do estudo, esta deve ser justificada e somente ser realizada após análise das razões da descontinuidade pelo CEP que o aprovou. O pesquisador deve aguardar o parecer do CEP quanto à descontinuação, exceto quando perceber risco ou dano não previsto ao sujeito participante ou quando constatar a superioridade de uma estratégia diagnóstica ou terapêutica oferecida a um dos grupos da pesquisa, isto é, somente em caso de necessidade de ação imediata com intuito de proteger os participantes.

- O CEP deve ser informado de todos os efeitos adversos ou fatos relevantes que alterem o curso normal do estudo. É papel do pesquisador assegurar medidas imediatas adequadas frente a evento adverso grave ocorrido (mesmo que tenha sido em outro centro) e enviar notificação ao CEP e à Agência Nacional de Vigilância Sanitária – ANVISA – junto com seu posicionamento.

- Eventuais modificações ou emendas ao protocolo devem ser apresentadas ao CEP de forma clara e sucinta, identificando a parte do protocolo a ser modificada e suas justificativas e aguardando a aprovação do CEP para continuidade da pesquisa. Em caso de projetos do Grupo I ou II apresentados anteriormente à ANVISA, o pesquisador ou patrocinador deve enviá-las também à mesma, junto com o parecer aprovatório do CEP, para serem juntadas ao protocolo inicial.

- Relatórios parciais e final devem ser apresentados ao CEP, inicialmente seis meses após a data deste parecer de aprovação e ao término do estudo.

-Lembramos que segundo a Resolução 466/2012 , item XI.2 letra e, “cabe ao pesquisador apresentar dados solicitados pelo CEP ou pela CONEP a qualquer momento".

Este parecer foi elaborado baseado nos documentos abaixo relacionados:

Tipo Documento	Arquivo	Postagem	Autor	Situação
Informações Básicas do Projeto	PB_INFORMAÇÕES_BÁSICAS_856126 E2.pdf	20/01/2017 19:15:31		Aceito
TCLE / Termos de Assentimento / Justificativa de Ausência	TCLE_Validacao.pdf	20/05/2016 10:05:05	Rickson Coelho Mesquita	Aceito
TCLE / Termos de Assentimento / Justificativa de Ausência	TCLE_Pacientes.pdf	20/05/2016 10:04:49	Rickson Coelho Mesquita	Aceito
Folha de Rosto	FolhaRosto_CEP_Rickson.pdf	19/05/2016 11:45:14	Rickson Coelho Mesquita	Aceito
Outros	Anuencia_Assinado.pdf	16/05/2016 23:01:16	Rickson Coelho Mesquita	Aceito
Projeto Detalhado / Brochura Investigador	ProjetoPesquisa_Revisado.pdf	16/05/2016 22:59:46	Rickson Coelho Mesquita	Aceito

Situação do Parecer:
Aprovado

Necessita Apreciação da CONEP:
Não

CAMPINAS, 07 de Fevereiro de 2017

Assinado por:
Renata Maria dos Santos Celeghini
(Coordenador)

Appendix C

Consent forms

TERMO DE CONSENTIMENTO LIVRE E ESCLARECIDO

Monitoramento da oxigenação, fluxo sanguíneo e metabolismo cerebral com espectroscopias ópticas de difusão em pacientes de AVC

Rickson C. Mesquita, Rodrigo M. Forti, Lenise Valler, Marilise Katsurayama, Danilo dos Santos Silva, Wagner M. Avelar

Número do CAAE: 56602516.2.0000.5404

Você está sendo convidado a participar como voluntário de uma pesquisa. Este documento, chamado Termo de Consentimento Livre e Esclarecido, visa assegurar seus direitos como participante e é elaborado em duas vias, uma que deverá ficar com você e outra com o pesquisador.

Por favor, leia com atenção e calma, aproveitando para esclarecer suas dúvidas. Se houver perguntas antes ou mesmo depois de assiná-lo, você poderá esclarecê-las com o pesquisador. Se preferir, pode levar este Termo para casa e consultar seus familiares ou outras pessoas antes de decidir participar. Não haverá nenhum tipo de penalização ou prejuízo se você não aceitar participar ou retirar sua autorização em qualquer momento.

Justificativa e objetivos:

O objetivo geral deste projeto é avaliar a utilidade de técnicas ópticas no Brasil para auxiliar no monitoramento de pacientes com AVC. Uma vez que estas técnicas são novas na realidade brasileira, tal estudo se faz importante para melhor conhecer como doenças cerebrovasculares, como o acidente vascular cerebral (AVC), afeta o funcionamento do cérebro. Também é importante saber como estas novas técnicas podem ajudar a melhorar o diagnóstico e acompanhamento de pacientes após serem diagnosticados com alguma lesão cerebrovascular.

As técnicas a serem utilizadas são conhecidas como espectroscopia óptica de difusão (DOS) e espectroscopia de correlação de difusão (DCS). DOS e DCS são técnicas inofensivas, capazes de produzir informações sobre as mudanças da oxigenação e do fluxo de sangue no cérebro quando este interage com a luz infravermelha de forma portátil e não invasiva. Nosso equipamento usa uma combinação de DOS e de DCS.

Procedimentos:

Participando do estudo você está sendo convidado a ser monitorado com uma técnica extra ao que já se faz clinicamente. Os pesquisadores irão trazer um equipamento óptico de DOS/DCS até o seu leito, e colocarão um sensor óptico sobre a sua cabeça. Este sensor contém fibras ópticas, que serão posicionadas para iluminar e/ou coletar a luz infravermelha. A potência e o comprimento de onda da luz incidente não produzem riscos para você. A coleta de dados durará entre 2 horas e 8 horas, dependendo do seu diagnóstico inicial e prognóstico de melhora durante o período de internação. Durante este período você não estará restrito a nada, seguindo o tratamento normalmente. Este procedimento poderá se repetir todos os dias durante a sua hospitalização, até o dia de você ir embora.

Durante a realização do exame você estará acompanhado pelos pesquisadores, que passarão informações detalhadas e esclarecerão as suas dúvidas a respeito de cada procedimento. Caso você se sinta desconfortável, pode pedir para encerrar o estudo a qualquer momento, em qualquer dia. Neste caso, a sua participação será interrompida sem qualquer penalidade. Seu tratamento no hospital não será prejudicado de forma alguma.

Rubrica do pesquisador:_______________ Rubrica do participante:_______________

Desconfortos e riscos:

As técnicas de DOS e DCS tem sido utilizadas desde o início da década de 1990 como instrumento de pesquisa, incluindo pacientes com distúrbios e doenças neurológicos, sem nenhum risco determinado. Não há riscos previsíveis da técnica, pois a potência da luz utilizada é muito baixa para produzir algum dano no tecido.

Quanto aos desconfortos, você poderá sentir um pouco a pressão das fibras sobre a sua cabeça. O procedimento é minucioso e o uso do arranjo pode causar um certo desconforto. Por este motivo, o sensor óptico será reposicionado a cada 2 horas. Caso o desconforto seja grande, você poderá avisar aos pesquisadores e eles reposicionarão o arranjo para melhorar o conforto antes deste período.

Benefícios:

Você não obterá nenhuma vantagem direta com a sua participação nesse estudo. Contudo, os resultados da pesquisa podem, a longo prazo, trazer melhorias nos diagnósticos e tratamentos clínicos com DOS/DCS para pacientes com doenças cerebrovasculares, na mesma situação que a sua. Os resultados do seu exame de DOS/DCS ficarão à disposição caso você e/ou seu médico queiram saber os resultados no futuro.

Sigilo e privacidade:

Você tem a garantia de que sua identidade será mantida em sigilo e nenhuma informação será dada a outras pessoas que não façam parte da equipe de pesquisadores. Na divulgação dos resultados desse estudo, seu nome não será citado. Os resultados do estudo poderão fazer parte do prontuário médico, mesmo que retrospectivo.

Ressarcimento e Indenização:

Você não será reembolsado pela sua participação na pesquisa, uma vez que a mesma não vai gerar nenhum gasto. Você terá a garantia ao direito a indenização diante de eventuais danos decorrentes da pesquisa.

Contato:

Em caso de dúvidas sobre a pesquisa, você poderá entrar em contato com os pesquisadores Rickson Coelho Mesquita, no Laboratório de Física Médica do Hospital das Clínicas da UNICAMP, na Rua Tessália Vieira de Camargo, 126, telefone (19) 3521-0137, e-mail: rickson@ifi.unicamp.br, ou com Marilise Katsurayama, no Departamento de Neurologia do Hospital das Clínicas da UNICAMP, na Rua Tessália Vieira de Camargo, 126, telefone (19) 3521-7489, e-mail: marilise_k@hotmail.com

Em caso de denúncias ou reclamações sobre sua participação e sobre questões éticas do estudo, você poderá entrar em contato com a secretaria do Comitê de Ética em Pesquisa (CEP) da UNICAMP das 08:30hs às 11:30hs e das 13:00hs as 17:00hs na Rua: Tessália Vieira de Camargo, 126; CEP 13083-887 Campinas – SP; telefone (19) 3521-8936 ou (19) 3521-7187; e-mail: cep@fcm.unicamp.br.

O Comitê de Ética em Pesquisa (CEP).

O papel do CEP é avaliar e acompanhar os aspectos éticos de todas as pesquisas envolvendo seres humanos. A Comissão Nacional de Ética em Pesquisa (CONEP), tem por objetivo desenvolver a regulamentação sobre proteção dos seres humanos envolvidos nas pesquisas. Desempenha um papel coordenador da rede de Comitês de Ética em Pesquisa (CEPs) das instituições, além de assumir a função de órgão consultor na área de ética em pesquisas.

Rubrica do pesquisador:_______________ Rubrica do participante:_______________

Consentimento livre e esclarecido:

Após ter recebido esclarecimentos sobre a natureza da pesquisa, seus objetivos, métodos, benefícios previstos, potenciais riscos e o incômodo que esta possa acarretar, aceito participar e declaro estar recebendo uma via original deste documento assinada pelo pesquisador e por mim, tendo todas as folhas por nós rubricadas:

Nome do (a) participante: ____

Contato telefônico: ____

e-mail (opcional): ____

____ Data: ____/_____/______.
(Assinatura do participante ou nome e assinatura do seu RESPONSÁVEL LEGAL)

Responsabilidade do Pesquisador:

Asseguro ter cumprido as exigências da resolução 466/2012 CNS/MS e complementares na elaboração do protocolo e na obtenção deste Termo de Consentimento Livre e Esclarecido. Asseguro, também, ter explicado e fornecido uma via deste documento ao participante. Informo que o estudo foi aprovado pelo CEP perante o qual o projeto foi apresentado. Comprometo-me a utilizar o material e os dados obtidos nesta pesquisa exclusivamente para as finalidades previstas neste documento ou conforme o consentimento dado pelo participante.

____ Data: ____/_____/______.
(Assinatura do pesquisador)

Rubrica do pesquisador:______________ Rubrica do participante:______________

Bibliography

1. Lotufo, P. A., Goulart, A. C., De Azeredo Passos, V. M., Satake, F. M., de Souza, M. D. F. M., França, E. B., Ribeiro, A. L. P. & Bensenõr, I. J. M. Cerebrovascular disease in Brazil from 1990 to 2015: Global Burden of Disease 2015. *Revista Brasileira de Epidemiologia* **20,** 129–141 (2017).

2. Al-Tamimi, Y. Z., Orsi, N. M., Quinn, A. C., Homer-Vanniasinkam, S. & Ross, S. A. A Review of Delayed Ischemic Neurologic Deficit Following Aneurysmal Subarachnoid Hemorrhage: Historical Overview, Current Treatment, and Pathophysiology. *World Neurosurgery* **73,** 654–667 (2010).

3. Cunningham, A. S., Salvador, R., Coles, J. P., Chatfield, D. A., Bradley, P. G., Johnston, A. J., Steiner, L. A., Fryer, T. D., Aigbirhio, F. I., Smielewski, P., Williams, G. B., Carpenter, T. A., Gillard, J. H., Pickard, J. D. & Menon, D. K. Physiological thresholds for irreversible tissue damage in contusional regions following traumatic brain injury. *Brain* **128,** 1931–1942 (2005).

4. Vergouwen, M. D., Vermeulen, M., van Gijn, J., Rinkel, G. J., Wijdicks, E. F., Muizelaar, J. P., Mendelow, A. D., Juvela, S., Yonas, H., Terbrugge, K. G., Macdonald, R. L., Diringer, M. N., Broderick, J. P., Dreier, J. P. & Roos, Y. B. Definition of Delayed Cerebral Ischemia After Aneurysmal Subarachnoid Hemorrhage as an Outcome Event in Clinical Trials and Observational Studies. *Stroke* **41,** 2391–2395 (2010).

5. Werner, C. & Engelhard, K. Pathophysiology of traumatic brain injury. *British Journal of Anaesthesia* **99,** 4–9 (2007).

6. Le Roux, P. *et al.* Consensus summary statement of the International Multidisciplinary Consensus Conference on Multimodality Monitoring in Neurocritical Care: A statement for healthcare professionals from the Neurocritical Care Society and the European Society of Intensive Care Medicine. *Intensive Care Medicine* **40,** 1189–1209 (2014).

7. Sandsmark, D. K., Kumar, M. A., Park, S. & Levine, J. M. Multimodal Monitoring in Subarachnoid Hemorrhage. *Stroke* **43,** 1440–1445 (2012).

8. Oddo, M., Villa, F. & Citerio, G. Brain multimodality monitoring. *Current Opinion in Critical Care* **18,** 111–118 (2012).
9. Bishop, C. C., Powell, S., Rutt, D. & Browse, N. L. Transcranial doppler measurement of middle cerebral artery blood flow velocity: A validation study. *Stroke* **17,** 913–915 (1986).
10. Demchuk, A. M., Christou, I., Wein, T. H., Felberg, R. A., Malkoff, M., Grotta, J. C. & Alexandrov, A. V. Accuracy and Criteria for Localizing Arterial Occlusion With Transcranial Doppler. *Journal of Neuroimaging* **10,** 1–12 (2000).
11. Purkayastha, S. & Sorond, F. Transcranial doppler ultrasound: Technique and application. *Seminars in Neurology* **32,** 411–420 (2012).
12. Banu, S. H. EEG in ICU: A monitoring tool for critically ill patient. *Bangladesh Critical Care Journal* **2,** 28–34 (2014).
13. Durduran, T., Choe, R., Baker, W. B. & Yodh, A. G. Diffuse optics for tissue monitoring and tomography. *Reports on Progress in Physics* **73,** 076701 (2010).
14. Durduran, T. & Yodh, A. G. Diffuse correlation spectroscopy for non-invasive, micro-vascular cerebral blood flow measurement. *NeuroImage* **85,** 5163 (2014).
15. Ferradal, S. L., Yuki, K., Vyas, R., Ha, C. G., Yi, F., Stopp, C., Wypij, D., Cheng, H. H., Newburger, J. W., Kaza, A. K., Franceschini, M. A., Kussman, B. D. & Grant, P. E. Non-invasive Assessment of Cerebral Blood Flow and Oxygen Metabolism in Neonates during Hypothermic Cardiopulmonary Bypass: Feasibility and Clinical Implications. *Scientific Reports* **7,** 44117 (2017).
16. Shang, Y., Li, T. & Yu, G. Clinical applications of near-infrared diffuse correlation spectroscopy and tomography for tissue blood flow monitoring and imaging. *Physiological Measurement* **38,** R1–R26 (2017).
17. Mesquita, R. C., Durduran, T., Yu, G., Buckley, E. M., Kim, M. N., Zhou, C., Choe, R., Sunar, U. & Yodh, A. G. Direct measurement of tissue blood flow and metabolism with diffuse optics. *Philosophical Transactions of the Royal Society A: Mathematical, Physical and Engineering Sciences* **369,** 4390–4406 (2011).
18. Fantini, S., Sassaroli, A., Tgavalekos, K. T. & Kornbluth, J. Cerebral blood flow and autoregulation: current measurement techniques and prospects for noninvasive optical methods. *Neurophotonics* **3,** 031411 (2016).
19. Ferrari, M. & Quaresima, V. A brief review on the history of human functional near-infrared spectroscopy (fNIRS) development and fields of application. *NeuroImage* **63,** 921–935 (2012).

20. Baker, W. B. *Optical Cerebral Blood Flow Monitoring of Mice To Men* PhD thesis (University of Pennsylvania, 2015), 273.

21. Forti, R. M. *Determination of the dynamical properties in turbid media using diffuse correlation spectroscopy: applications to biological tissues* Master's dissertation (University of Campinas, 2015).

22. Yu, G., Floyd, T. F., Durduran, T., Zhou, C., Wang, J., Detre, J. a. & Yodh, A. G. Validation of diffuse correlation spectroscopy for muscle blood flow with concurrent arterial spin labeled perfusion MRI. *Optics express* **15,** 1064–1075 (2007).

23. Milej, D. *et al.* Quantification of cerebral blood flow in adults by contrast-enhanced near-infrared spectroscopy: Validation against MRI. *Journal of Cerebral Blood Flow & Metabolism* (2019).

24. Kim, M. N. *et al.* Noninvasive Measurement of Cerebral Blood Flow and Blood Oxygenation Using Near-Infrared and Diffuse Correlation Spectroscopies in Critically Brain-Injured Adults. *Neurocritical Care* **12,** 173–180 (2010).

25. Parthasarathy, A. B., Gannon, K. P., Baker, W. B., Favilla, C. G., Balu, R., Kasner, S. E., Yodh, A. G., Detre, J. A. & Mullen, M. T. Dynamic autoregulation of cerebral blood flow measured non-invasively with fast diffuse correlation spectroscopy. *Journal of Cerebral Blood Flow and Metabolism* **38,** 230–240 (2018).

26. Baker, W. B., Parthasarathy, A. B., Gannon, K. P., Kavuri, V. C., Busch, D. R., Abramson, K., He, L., Mesquita, R. C., Mullen, M. T., Detre, J. A., Greenberg, J. H., Licht, D. J., Balu, R., Kofke, W. A. & Yodh, A. G. Noninvasive optical monitoring of critical closing pressure and arteriole compliance in human subjects. *Journal of Cerebral Blood Flow and Metabolism* **37,** 2691–2705 (2017).

27. Zirak, P., Delgado-Mederos, R., Martí-Fàbregas, J. & Durduran, T. Effects of acetazolamide on the micro- and macro-vascular cerebral hemodynamics: a diffuse optical and transcranial doppler ultrasound study. *Biomedical optics express* **1,** 1443–1459 (2010).

28. Buckley, E. M., Hance, D., Pawlowski, T., Lynch, J., Wilson, F. B., Mesquita, R. C., Durduran, T., Diaz, L. K., Putt, M. E., Licht, D. J., Fogel, M. A. & Yodh, A. G. Validation of diffuse correlation spectroscopic measurement of cerebral blood flow using phase-encoded velocity mapping magnetic resonance imaging. *Journal of Biomedical Optics* **17,** 037007 (2012).

29. Zhou, C., Eucker, S. A., Durduran, T., Yu, G., Ralston, J., Friess, S. H., Ichord, R. N., Margulies, S. S. & Yodh, A. G. Diffuse optical monitoring of hemodynamic changes in piglet brain with closed head injury. *Journal of Biomedical Optics* **14,** 034015 (2009).

30. Culver, J. P., Durduran, T., Furuya, D., Cheung, C., Greenberg, J. H. & Yodh, A. G. Diffuse Optical Tomography of Cerebral Blood Flow, Oxygenation, and Metabolism in Rat during Focal Ischemia. *Journal of Cerebral Blood Flow & Metabolism* **23,** 911–924 (2003).

31. Valabrègue, R., Aubert, A., Burger, J., Bittoun, J. & Costalat, R. Relation between Cerebral Blood Flow and Metabolism Explained by a Model of Oxygen Exchange. *Journal of Cerebral Blood Flow & Metabolism* **23,** 536–545 (2003).

32. Farzam, P., Buckley, E. M., Lin, P.-Y., Hagan, K., Grant, P. E., Inder, T. E., Carp, S. A. & Franceschini, M. A. Shedding light on the neonatal brain: probing cerebral hemodynamics by diffuse optical spectroscopic methods. *Scientific Reports* **7,** 15786 (2017).

33. Wong, F. in *Prenatal and Postnatal Determinants of Development* 69–87 (Humana Press, New York, NY, 2016).

34. Busch, D. R., Rusin, C. G., Miller-Hance, W., Kibler, K., Baker, W. B., Heinle, J. S., Fraser, C. D., Yodh, A. G., Licht, D. J. & Brady, K. M. Continuous cerebral hemodynamic measurement during deep hypothermic circulatory arrest. *Biomedical Optics Express* **7,** 3461 (2016).

35. Ko, T. S. *et al.* Non-invasive optical neuromonitoring of the temperature-dependence of cerebral oxygen metabolism during deep hypothermic cardiopulmonary bypass in neonatal swine. *Journal of Cerebral Blood Flow & Metabolism* **40,** 187–203 (2018).

36. Pennekamp, C. W., Bots, M. L., Kappelle, L. J., Moll, F. L. & de Borst, G. J. The Value of Near-Infrared Spectroscopy Measured Cerebral Oximetry During Carotid Endarterectomy in Perioperative Stroke Prevention. A Review. *European Journal of Vascular and Endovascular Surgery* **38,** 539–545 (2009).

37. Pennekamp, C. W., Immink, R. V., Den Ruijter, H. M., Kappelle, L. J., Ferrier, C. M., Bots, M. L., Buhre, W. F., Moll, F. L. & De Borst, G. J. Near-infrared spectroscopy can predict the onset of cerebral hyperperfusion syndrome after carotid endarterectomy. *Cerebrovascular Diseases* **34,** 314–321 (2012).

38. Shang, Y., Cheng, R., Dong, L., Ryan, S. J., Saha, S. P. & Yu, G. Cerebral monitoring during carotid endarterectomy using near-infrared diffuse optical spectroscopies and electroencephalogram. *Physics in Medicine and Biology* **56,** 3015–3032 (2011).

39. Delgado-Mederos, R., Gregori-Pla, C., Zirak, P., Blanco, I., Dinia, L., Marín, R., Durduran, T. & Martí-Fàbregas, J. Transcranial diffuse optical assessment of the microvascular reperfusion after thrombolysis for acute ischemic stroke. *Biomedical Optics Express* **9,** 1262 (2018).

40. Favilla, C. G., Mesquita, R. C., Mullen, M., Durduran, T., Lu, X., Kim, M. N., Minkoff, D. L., Kasner, S. E., Greenberg, J. H., Yodh, A. G. & Detre, J. A. Optical Bedside Monitoring of Cerebral Blood Flow in Acute Ischemic Stroke Patients During Head-of-Bed Manipulation. *Stroke* **45,** 1269–1274 (2014).

41. Gregori-Pla, C., Blanco, I., Camps-Renom, P., Zirak, P., Serra, I., Cotta, G., Maruccia, F., Prats-Sánchez, L., Martínez-Domeño, A., Busch, D. R., Giacalone, G., Martí-Fàbregas, J., Durduran, T. & Delgado-Mederos, R. Early microvascular cerebral blood flow response to head-of-bed elevation is related to outcome in acute ischemic stroke. *Journal of Neurology* **266,** 990–997 (2019).

42. Kim, M. N., Edlow, B. L., Durduran, T., Frangos, S., Mesquita, R. C., Levine, J. M., Greenberg, J. H., Yodh, A. G. & Detre, J. A. Continuous optical monitoring of cerebral hemodynamics during head-of-bed manipulation in brain-injured adults. *Neurocritical Care* **20,** 443–453 (2014).

43. Ko, T., Mavroudis, C. D., Boorady, T., Mensah-Brown, K., Morgan, R., Lautz, A., Bratinov, G., Lin, Y., Jeong, S., Nadkarni, V. M., Berg, R. A., Sutton, R. M., Yodh, A. G., Kilbaugh, T. J. & Licht, D. *Prediction of Return of Spontaneous Circulation During Cardiopulmonary Resuscitation using Frequency-Domain Diffuse Optical Spectroscopy in a Pediatric Swine Model of Asphyxial Cardiac Arrest* in *Biophotonics Congress: Biomedical Optics Congress 2018 (Microscopy/Translational/Brain/OTS)* (OSA, Washington, D.C., 2018), CW2B.5.

44. Favilla, C. G., Parthasarathy, A. B., Detre, J. A., Yodh, A. G., Mullen, M. T., Kasner, S. E., Gannon, K. & Messé, S. R. Non-invasive respiratory impedance enhances cerebral perfusion in healthy adults. *Frontiers in Neurology* **8,** 1–7 (2017).

45. Favilla, C. G., Forti, R. M., Zamzam, A., Detre, J. A., Mullen, M. T., Yodh, A. G., Kasner, S. E., Busch, D. R., Baker, W. B., Mesquita, R. C., Kung, D. & Messé, S. R. Perfusion Enhancement with Respiratory Impedance After Stroke (PERI-Stroke). *Neurotherapeutics* (2019).

46. Ritzenthaler, T., Cho, T.-H., Mechtouff, L., Ong, E., Turjman, F., Robinson, P., Berthezène, Y. & Nighoghossian, N. Cerebral near-infrared spectroscopy a potential approach for thrombectomy monitoring. *Stroke* **48,** 3390–3392 (2017).

47. Selb, J., Wu, K.-C., Sutin, J., Lin, P.-Y. (, Farzam, P., Bechek, S. & Shenoy, A. Prolonged monitoring of cerebral blood flow and autoregulation with diffuse correlation spectroscopy in neurocritical care patients. *Neurophotonics* **5,** 1 (2018).

48. Muehlschlegel, S., Selb, J., Patel, M., Diamond, S. G., Franceschini, M. A., Sorensen, A. G., Boas, D. A. & Schwamm, L. H. Feasibility of NIRS in the Neurointensive Care Unit: A Pilot Study in Stroke Using Physiological Oscillations. *Neurocritical Care* **11,** 288–295 (2009).

49. Busch, D. R., Balu, R., Baker, W. B., Guo, W., He, L., Diop, M., Milej, D., Kavuri, V., Amendolia, O., St. Lawrence, K., Yodh, A. G. & Kofke, W. A. Detection of Brain Hypoxia Based on Noninvasive Optical Monitoring of Cerebral Blood Flow with Diffuse Correlation Spectroscopy. *Neurocritical Care* **30,** 72–80 (2019).

50. Baker, W. B., Balu, R., He, L., Kavuri, V. C., Busch, D. R., Amendolia, O., Quattrone, F., Frangos, S., Maloney-Wilensky, E., Abramson, K., Mahanna Gabrielli, E., Yodh, A. G. & Andrew Kofke, W. Continuous non-invasive optical monitoring of cerebral blood flow and oxidative metabolism after acute brain injury. *Journal of Cerebral Blood Flow and Metabolism* **39,** 1469–1485 (2019).

51. Kainerstorfer, J. M., Sassaroli, A., Tgavalekos, K. T. & Fantini, S. Cerebral autoregulation in the microvasculature measured with near-infrared spectroscopy. *Journal of Cerebral Blood Flow and Metabolism* **35,** 959–966 (2015).

52. Case, K. M., Zweifel, P. F. & Pomraning, G. C. Linear Transport Theory. *Physics Today* **21,** 72–73 (1968).

53. Fantini, S. & Sassaroli, A. in *Handbook of Optical Biomedical Diagnostics, Second Edition, Volume 1: Light-Tissue Interaction* chap. 7 (SPIE PRESS, 2016).

54. Dougherty, R., Ackerson, B., Reguigui, N., Dorri-Nowkoorani, F. & Nobbmann, U. Correlation transfer: Development and application. *Journal of Quantitative Spectroscopy and Radiative Transfer* **52,** 713–727 (1994).

55. Boas, D. A. *Diffuse photon probes of structural and dynamical properties of turbid media: Theory and biomedical application* PhD thesis (University of Pennsylvania, 1996), 260.

56. Haskell, R. C., Svaasand, L. O., Tsay, T.-T., Feng, T.-C., Tromberg, B. J. & McAdams, M. S. Boundary conditions for the diffusion equation in radiative transfer. *Journal of the Optical Society of America A* **11,** 2727 (1994).

57. Patterson, M., Madsen, S., Moulton, J. & Wilson, B. *Diffusion equation representation of photon migration in tissue* in *1991 IEEE MTT-S International Microwave Symposium Digest* (IEEE, 1991), 905–908.

58. Farrell, T. J., Patterson, M. S. & Wilson, B. A diffusion theory model of spatially resolved, steady-state diffuse reflectance for the noninvasive determination of tissue optical properties in vivo. *Medical Physics* **19,** 879–888 (1992).

59. Torricelli, A., Contini, D., Pifferi, A., Caffini, M., Re, R., Zucchelli, L. & Spinelli, L. Time domain functional NIRS imaging for human brain mapping. *NeuroImage* **85,** 28–50 (2014).

60. Ackerson, B. J., Dougherty, R. L., Reguigui, N. M. & Nobbmann, U. Correlation transfer: Application of radiative transfer solution methods to photon correlation problems. *Journal of Thermophysics and Heat Transfer* **6,** 577–588 (1992).

61. Corlu, A., Choe, R., Durduran, T., Lee, K., Schweiger, M., Arridge, S. R., Hillman, E. M. C. & Yodh, A. G. Diffuse optical tomography with spectral constraints and wavelength optimization. *Applied Optics* **44,** 2082 (2005).

62. Jacques, S. L. Optical properties of biological tissues: a review. *Physics in Medicine and Biology* **58,** R37–R61 (2013).

63. Jain, V., Buckley, E. M., Licht, D. J., Lynch, J. M., Schwab, P. J., Naim, M. Y., Lavin, N. A., Nicolson, S. C., Montenegro, L. M., Yodh, A. G. & Wehrli, F. W. Cerebral oxygen metabolism in neonates with congenital heart disease quantified by MRI and optics. *Journal of Cerebral Blood Flow and Metabolism* **34,** 380–388 (2014).

64. Corlu, A., Durduran, T., Choe, R., Schweiger, M., Hillman, E. M. C., Arridge, S. R. & Yodh, A. G. Uniqueness and wavelength optimization in continuous-wave multispectral diffuse optical tomography. *Optics Letters* **28,** 2339 (2003).

65. Arridge, S. R. & Lionheart, W. R. B. Nonuniqueness in diffusion-based optical tomography. *Optics Letters* **23,** 882 (1998).

66. Delpy, D. T., Cope, M., Van Der Zee, P., Arridge, S., Wray, S. & Wyatt, J. Estimation of optical pathlength through tissue from direct time of flight measurement. *Physics in Medicine and Biology* **33,** 1433–1442 (1988).

67. Scholkmann, F., Kleiser, S., Metz, A. J., Zimmermann, R., Mata Pavia, J., Wolf, U. & Wolf, M. A review on continuous wave functional near-infrared spectroscopy and imaging instrumentation and methodology. *NeuroImage* **85,** 6–27 (2014).

68. Novi Junior, S. L., Aparecido da Rocha, W. A., Carvalho, A. D. C., Scavariello, G. H., Forti, R. M., Guiroga Soto, A. F., Oliveira, V. R., Yasuda, C. L. & Mesquita, R. C. Desenvolvimento de Novos Métodos para Investigação do Cérebro durante o Estado de Repouso. *Revista Brasileira de Física Médica* **11,** 33 (2018).

69. Novi, S. L., Rodrigues, R. B. M. L. & Mesquita, R. C. Resting state connectivity patterns with near-infrared spectroscopy data of the whole head. *Biomedical Optics Express* **7,** 2524 (2016).

70. De Oliveira, S. R., Machado, A. C. C., de Paula, J. J., Novi, S. L., Mesquita, R. C., de Miranda, D. M. & Bouzada, M. C. F. Changes of functional response in sensorimotor cortex of preterm and full-term infants during the first year: An fNIRS study. *Early Human Development* **133,** 23–28 (2019).

71. De Oliveira, S. R., de Paula Machado, A. C. C., de Paula, J. J., de Moraes, P. H. P., Nahin, M. J. S., Magalhães, L. d. C., Novi, S. L., Mesquita, R. C., de Miranda, D. M. & Bouzada, M. C. F. Association between hemodynamic activity and motor performance in six-month-old full-term and preterm infants: a functional near-infrared spectroscopy study. *Neurophotonics* **5,** 1 (2017).

72. Mesquita, R. C., Franceschini, M. A. & Boas, D. A. Resting state functional connectivity of the whole head with near-infrared spectroscopy. *Biomedical Optics Express* **1,** 324 (2010).

73. Franceschini, M. A., Joseph, D. K., Huppert, T. J., Diamond, S. G. & Boas, D. A. Diffuse optical imaging of the whole head. *Journal of Biomedical Optics* **11,** 054007 (2006).

74. Eggebrecht, A. T., Ferradal, S. L., Robichaux-Viehoever, A., Hassanpour, M. S., Dehghani, H., Snyder, A. Z., Hershey, T. & Culver, J. P. Mapping distributed brain function and networks with diffuse optical tomography. *Nature Photonics* **8,** 448–454 (2014).

75. Piper, S. K., Krueger, A., Koch, S. P., Mehnert, J., Habermehl, C., Steinbrink, J., Obrig, H. & Schmitz, C. H. A wearable multi-channel fNIRS system for brain imaging in freely moving subjects. *NeuroImage* **85,** 64–71 (2014).

76. Pinti, P., Aichelburg, C., Lind, F., Power, S., Swingler, E., Merla, A., Hamilton, A., Gilbert, S., Burgess, P. & Tachtsidis, I. Using Fiberless, Wearable fNIRS to Monitor Brain Activity in Real-world Cognitive Tasks. *Journal of Visualized Experiments* (2015).

77. Pinti, P., Aichelburg, C., Gilbert, S., Hamilton, A., Hirsch, J., Burgess, P. & Tachtsidis, I. A Review on the Use of Wearable Functional Near-Infrared Spectroscopy in Naturalistic Environments. *Japanese Psychological Research* **60,** 347–373 (2018).

78. McKendrick, R., Parasuraman, R., Murtza, R., Formwalt, A., Baccus, W., Paczynski, M. & Ayaz, H. Into the wild: Neuroergonomic differentiation of hand-held and augmented reality wearable displays during outdoor navigation with functional near infrared spectroscopy. *Frontiers in Human Neuroscience* **10** (2016).

79. Strait, M. & Scheutz, M. What we can and cannot (yet) do with functional near infrared spectroscopy. *Frontiers in Neuroscience* **8** (2014).

80. Boas, D. A., Elwell, C. E., Ferrari, M. & Taga, G. Twenty years of functional near-infrared spectroscopy: Introduction for the special issue. *NeuroImage* **85,** 1–5 (2014).

81. Green, M. S., Sehgal, S. & Tariq, R. Near-infrared spectroscopy: The new must have tool in the intensive care unit? *Seminars in Cardiothoracic and Vascular Anesthesia* **20,** 213–224 (2016).

82. Obrig, H. NIRS in clinical neurology - a ’promising’ tool? *NeuroImage* **85,** 535–546 (2014).

83. Hametner, C., Stanarcevic, P., Stampfl, S., Rohde, S., Veltkamp, R. & Bösel, J. Non-invasive cerebral oximetry during endovascular therapy for acute ischemic stroke: An observational study. *Journal of Cerebral Blood Flow and Metabolism* **35,** 1722–1728 (2015).

84. Greisen, G., Leung, T. & Wolf, M. Has the time come to use near-infrared spectroscopy as a routine clinical tool in preterm infants undergoing intensive care? *Philosophical Transactions of the Royal Society A: Mathematical, Physical and Engineering Sciences* **369,** 4440–4451 (2011).

85. Wolf, M., Ferrari, M. & Quaresma, V. Progress of near-infrared spectroscopy and topography for brain and muscle clinical applications. *Journal of Biomedical Optics* **12,** 062104 (2007).

86. Proenca, M., Grossenbacher, O., Dasen, S., Moser, V., Ostojic, D., Lemkaddem, A., Ferrario, D., Lemay, M., Wolf, M., Fauchere, J. C. & Karen, T. *Performance Assessment of a Dedicated Reflectance Pulse Oximeter in a Neonatal Intensive Care Unit* in *Proceedings of the Annual International Conference of the IEEE Engineering in Medicine and Biology Society, EMBS* **2018-July** (IEEE, 2018), 1502–1505.

87. Davies, D. J., Clancy, M., Dehghani, H., Lucas, S. J. E., Forcione, M., Yakoub, K. M. & Belli, A. Cerebral Oxygenation in Traumatic Brain Injury: Can a Non-Invasive Frequency Domain Near-Infrared Spectroscopy Device Detect Changes in Brain Tissue Oxygen Tension as Well as the Established Invasive Monitor? *Journal of Neurotrauma* **36,** 1175–1183 (2019).

88. Gagnon, L., Cooper, R. J., Yücel, M. A., Perdue, K. L., Greve, D. N. & Boas, D. A. Short separation channel location impacts the performance of short channel regression in NIRS. *NeuroImage* **59,** 2518–2528 (2012).

89. Gagnon, L., Perdue, K., Greve, D. N., Goldenholz, D., Kaskhedikar, G. & Boas, D. A. Improved recovery of the hemodynamic response in diffuse optical imaging using short optode separations and state-space modeling. *NeuroImage* **56,** 1362–1371 (2011).

90. Goodwin, J. R., Gaudet, C. R. & Berger, A. J. Short-channel functional near-infrared spectroscopy regressions improve when source-detector separation is reduced. *Neurophotonics* **1,** 015002 (2014).

91. Huppert, T. J. Commentary on the statistical properties of noise and its implication on general linear models in functional near-infrared spectroscopy. *Neurophotonics* **3,** 010401 (2016).

92. Kirilina, E., Jelzow, A., Heine, A., Niessing, M., Wabnitz, H., Brühl, R., Ittermann, B., Jacobs, A. M. & Tachtsidis, I. The physiological origin of task-evoked systemic artefacts in functional near infrared spectroscopy. *NeuroImage* **61,** 70–81 (2012).

93. Yücel, M. A., Selb, J., Aasted, C. M., Lin, P.-Y., Borsook, D., Becerra, L. & Boas, D. A. Mayer waves reduce the accuracy of estimated hemodynamic response functions in functional near-infrared spectroscopy. *Biomedical Optics Express* **7,** 3078 (2016).

94. Fantini, S., Franceschini, M. A. & Gratton, E. Semi-infinite-geometry boundary problem for light migration in highly scattering media: a frequency-domain study in the diffusion approximation. *Journal of the Optical Society of America B* **11,** 2128 (1994).

95. Fantini, S., Franceschini, M. A., Fishkin, J. B., Barbieri, B. & Gratton, E. Quantitative determination of the absorption spectra of chromophores in strongly scattering media: a light-emitting-diode based technique. *Applied Optics* **33,** 5204 (1994).

96. Torjesen, A., Istfan, R. & Roblyer, D. Ultrafast wavelength multiplexed broad bandwidth digital diffuse optical spectroscopy for in vivo extraction of tissue optical properties. *Journal of Biomedical Optics* **22,** 036009 (2017).

97. Doulgerakis, M., Eggebrecht, A. T. & Dehghani, H. High-density functional diffuse optical tomography based on frequency-domain measurements improves image quality and spatial resolution. *Neurophotonics* **6** (eds Luo, Q., Ding, J. & Fu, L.) 1 (2019).

98. Pogue, B., Testorf, M., McBride, T., Osterberg, U. & Paulsen, K. Instrumentation and design of a frequency-domain diffuse optical tomography imager for breast cancer detection. *Optics Express* **1,** 391 (1997).

99. McBride, T. O., Pogue, B. W., Jiang, S., Österberg, U. L. & Paulsen, K. D. A parallel-detection frequency-domain near-infrared tomography system for hemoglobin imaging of the breast in vivo. *Review of Scientific Instruments* **72,** 1817 (2001).

100. Pham, T. H., Coquoz, O., Fishkin, J. B., Anderson, E. & Tromberg, B. J. Broad bandwidth frequency domain instrument for quantitative tissue optical spectroscopy. *Review of Scientific Instruments* **71,** 2500–2513 (2000).

101. No, K.-S., Kwong, R., Chou, P. H. & Cerussi, A. Design and testing of a miniature broadband frequency domain photon migration instrument. *Journal of Biomedical Optics* **13,** 050509 (2008).

102. Culver, J. P., Choe, R., Holboke, M. J., Zubkov, L., Durduran, T., Slemp, A., Ntziachristos, V., Chance, B. & Yodh, A. G. Three-dimensional diffuse optical tomography in the parallel plane transmission geometry: Evaluation of a hybrid frequency domain/continuous wave clinical system for breast imaging. *Medical Physics* **30,** 235–247 (2003).

103. Thompson, A. B. & Sevick-Muraca, E. M. Near-infrared fluorescence contrast-enhanced imaging with intensified charge-coupled device homodyne detection: measurement precision and accuracy. *Journal of Biomedical Optics* **8,** 111 (2003).

104. Pifferi, A., Contini, D., Mora, A. D., Farina, A., Spinelli, L. & Torricelli, A. New frontiers in time-domain diffuse optics , a review. *Journal of Biomedical Optics* **21** (2016).

105. Bianco, S. D., Martelli, F. & Zaccanti, G. Penetration depth of light re-emitted by a diffusive medium: theoretical and experimental investigation. *Physics in Medicine and Biology* **47,** 4131–4144 (2002).

106. Steinbrink, J., Wabnitz, H., Obrig, H., Villringer, A. & Rinneberg, H. Determining changes in NIR absorption using a layered model of the human head. *Physics in Medicine and Biology* **46,** 879–896 (2001).

107. Alerstam, E., Andersson-Engels, S. & Svensson, T. Improved accuracy in time-resolved diffuse reflectance spectroscopy. *Optics Express* **16,** 10440 (2008).

108. Cubeddu, R., Pifferi, A., Taroni, P., Torricelli, A. & Valentini, G. Experimental test of theoretical models for time-resolved reflectance. *Medical Physics* **23,** 1625–1633 (1996).

109. Spinelli, L., Martelli, F., Farina, A., Pifferi, A., Torricelli, A., Cubeddu, R. & Zaccanti, G. Accuracy of the nonlinear fitting procedure for time-resolved measurements on diffusive phantoms at NIR wavelengths. *Optical Tomography and Spectroscopy of Tissue VIII* **7174,** 717424 (2009).

110. Contini, D., Spinelli, L., Torricelli, A., Pifferi, A. & Cubeddu, R. *Novel method for depth-resolved brain functional imaging by timedomain NIRS* in *Optics InfoBase Conference Papers* (eds Pogue, B. W. & Cubeddu, R.) (2007), 662908.

111. Selb, J., Stott, J. J., Franceschini, M. A., Sorensen, A. G. & Boas, D. A. Improved sensitivity to cerebral hemodynamics during brain activation with a time-gated optical system: analytical model and experimental validation. *Journal of Biomedical Optics* **10,** 011013 (2005).

112. Liebert, A., Wabnitz, H., Steinbrink, J., Obrig, H., Möller, M., Macdonald, R., Villringer, A. & Rinneberg, H. Time-resolved multidistance near-infrared spectroscopy of the adult head: intracerebral and extracerebral absorption changes from moments of distribution of times of flight of photons. *Applied Optics* **43,** 3037 (2004).

113. Liebert, A., Wabnitz, H. & Elster, C. Determination of absorption changes from moments of distributions of times of flight of photons: optimization of measurement conditions for a two-layered tissue model. *Journal of Biomedical Optics* **17,** 057005 (2012).

114. Pirovano, I., Re, R., Candeo, A., Contini, D., Torricelli, A. & Spinelli, L. Instrument response function acquisition in reflectance geometry for time-resolved diffuse optical measurements. *Biomedical Optics Express* **11,** 240 (2020).

115. Liebert, A., Wabnitz, H., Grosenick, D. & Macdonald, R. Fiber dispersion in time domain measurements compromising the accuracy of determination of optical properties of strongly scattering media. *Journal of Biomedical Optics* **8,** 512–516 (2003).

116. Selb, J., Zimmermann, B. B., Martino, M., Ogden, T. & Boas, D. A. *Functional brain imaging with a supercontinuum time-domain NIRS system* in *Optical Tomography and Spectroscopy of Tissue X* (eds Tromberg, B. J., Yodh, A. G. & Sevick-Muraca, E. M.) **8578** (2013), 857807.

117. He, L. *et al.* Noninvasive continuous optical monitoring of absolute cerebral blood flow in critically ill adults. *Neurophotonics* **5,** 1 (2018).

118. Becker, W. *Advanced time-correlated single photon counting techniques* 2005.

119. Wabnitz, H., Moeller, M., Liebert, A., Obrig, H., Steinbrink, J. & Macdonald, R. Time-Resolved Near-Infrared Spectroscopy and Imaging of the Adult Human Brain. **977,** 143–148 (2017).

120. Selb, J., Joseph, D. K. & Boas, D. A. Time-gated optical system for depth-resolved functional brain imaging. *Journal of Biomedical Optics* **11,** 044008 (2006).

121. Zucchelli, L., Contini, D., Re, R., Torricelli, A. & Spinelli, L. Method for the discrimination of superficial and deep absorption variations by time domain fNIRS. *Biomedical Optics Express* **4,** 2893 (2013).

122. Spinelli, L., Pifferi, A., Contini, D., Cubeddu, R. & Torricelli, A. *Time-resolved optical stratigraphy in turbid media* in (eds Depeursinge, C. D. & Vitkin, I. A.) (2009), 73710A.

123. Dutton, N. A. W., Gnecchi, S., Parmesan, L., Holmes, A. J., Rae, B., Grant, L. A. & Henderson, R. K. *A time-correlated single-photon-counting sensor with 14GS/S histogramming time-to-digital converter* in *2015 IEEE International Solid-State Circuits Conference - (ISSCC) Digest of Technical Papers* (IEEE, 2015), 1–3.

124. Fujisaka, S.-i., Ozaki, T., Suzuki, T., Kamada, T., Kitazawa, K., Nishizawa, M., Takahashi, A. & Suzuki, S. in, 427–433 (2016).

125. Lemieux, P. A. & Durian, D. J. Investigating non-Gaussian scattering processes by using nth-order intensity correlation functions. *J. Opt. Soc. Am. A* **16,** 1651–1664 (1999).

126. Boas, D. A., Sakadžic, S., Selb, J., Farzam, P., Franceschini, M. A. & Carp, S. A. Establishing the diffuse correlation spectroscopy signal relationship with blood flow. *Neurophotonics* **3,** 031412 (2016).

127. Tang, J., Erdener, S. E., Li, B., Fu, B., Sakadzic, S., Carp, S. A., Lee, J. & Boas, D. A. Shear-induced diffusion of red blood cells measured with dynamic light scattering-optical coherence tomography. *Journal of Biophotonics* **11,** e201700070 (2018).

128. Zhou, C., Yu, G., Furuya, D., Greenberg, J. H., Yodh, A. G. & Durduran, T. Diffuse optical correlation tomography of cerebral blood flow during cortical spreading depression in rat brain. *Optics Express* **14,** 1125 (2006).

129. Zhou, C. *In-vivo optical imaging and spectroscopy of cerebral hemodynamics* PhD thesis (University of Pennsylvania, 2007).

130. Tamborini, D., Farzam, P., Zimmermann, B., Wu, K.-C., Boas, D. A. & Franceschini, M. A. Development and characterization of a multidistance and multiwavelength diffuse correlation spectroscopy system. *Neurophotonics* **5,** 1 (2017).

131. He, L., Lin, Y., Shang, Y., Shelton, B. J. & Yu, G. Using optical fibers with different modes to improve the signal-to-noise ratio of diffuse correlation spectroscopy flow-oximeter measurements. *Journal of Biomedical Optics* **18,** 037001 (2013).

132. Zuo, X. N., Di Martino, A., Kelly, C., Shehzad, Z. E., Gee, D. G., Klein, D. F., Castellanos, F. X., Biswal, B. B. & Milham, M. P. The oscillating brain: Complex and reliable. *NeuroImage* **49,** 1432–1445 (2010).

133. Cheng, R., Shang, Y., Hayes, D., Saha, S. P. & Yu, G. Noninvasive optical evaluation of spontaneous low frequency oscillations in cerebral hemodynamics. *NeuroImage* **62,** 1445–1454 (2012).

134. JULIEN, C. The enigma of Mayer waves: Facts and models. *Cardiovascular Research* **70,** 12–21 (2006).

135. Chen, B. R., Kozberg, M. G., Bouchard, M. B., Shaik, M. A. & Hillman, E. M. C. A Critical Role for the Vascular Endothelium in Functional Neurovascular Coupling in the Brain. *Journal of the American Heart Association* **3** (2014).

136. Czosnyka, M., Brady, K., Reinhard, M., Smielewski, P. & Steiner, L. A. Monitoring of cerebrovascular autoregulation: Facts, myths, and missing links. *Neurocritical Care* **10,** 373–386 (2009).

137. Wang, D., Parthasarathy, A. B., Baker, W. B., Gannon, K., Kavuri, V., Ko, T., Schenkel, S., Li, Z., Li, Z., Mullen, M. T., Detre, J. A. & Yodh, A. G. Fast blood flow monitoring in deep tissues with real-time software correlators. *Biomedical Optics Express* **7,** 776 (2016).

138. Mesquita, R. C., Schenkel, S. S., Minkoff, D. L., Lu, X., Favilla, C. G., Vora, P. M., Busch, D. R., Chandra, M., Greenberg, J. H., Detre, J. A. & Yodh, A. G. Influence of probe pressure on the diffuse correlation spectroscopy blood flow signal: extra-cerebral contributions. *Biomedical Optics Express* **4,** 978 (2013).

139. Wang, D., Baker, W. B., He, H., Gao, P., Zhu, L., Peng, Q., Li, Z., Li, F., Chen, T. & Feng, H. Influence of probe pressure on the pulsatile diffuse correlation spectroscopy blood flow signal on the forearm and forehead regions. *Neurophotonics* **6,** 1 (2019).

140. Baker, W. B., Parthasarathy, A. B., Ko, T. S., Busch, D. R., Abramson, K., Tzeng, S.-Y., Mesquita, R. C., Durduran, T., Greenberg, J. H., Kung, D. K. & Yodh, A. G. Pressure modulation algorithm to separate cerebral hemodynamic signals from extracerebral artifacts. *Neurophotonics* **2,** 035004 (2015).

141. Diop, M., Verdecchia, K., Lee, T.-Y. & St Lawrence, K. Calibration of diffuse correlation spectroscopy with a time-resolved near-infrared technique to yield absolute cerebral blood flow measurements. *Biomedical Optics Express* **2,** 2068 (2011).

142. Forti, R. M. *et al.* Transcranial Optical Monitoring of Cerebral Hemodynamics in Acute Stroke Patients during Mechanical Thrombectomy. *Journal of Stroke and Cerebrovascular Diseases* **28,** 1483–1494 (2019).

143. Forti, R. M., Katsurayama, M., Menko, J., Valler, L., Quiroga, A., Falcão, A. L. E., Li, L. M. & Mesquita, R. C. Real-time non-invasive assessment of cerebral hemodynamics with diffuse optical spectroscopies in a neuro intensive care unit: an observational case study. *Frontiers in Medicine* (Submitted).

144. Selb, J., Boas, D. A., Chan, S.-T., Evans, K. C., Buckley, E. M. & Carp, S. A. Sensitivity of near-infrared spectroscopy and diffuse correlation spectroscopy to brain hemodynamics: simulations and experimental findings during hypercapnia. *Neurophotonics* **1,** 015005 (2014).

145. Newville, M., Ingargiola, A., Stensitzki, T. & Allen, D. B. LMFIT: Non-Linear Least-Square Minimization and Curve-Fitting for Python. *Zenodo* (2014).

146. Oliphant, T. E. SciPy: Open source scientific tools for Python. *Computing in Science and Engineering* (2007).

147. Hunter, J. D. Matplotlib: A 2D Graphics Environment. *Computing in Science & Engineering* **9,** 90–95 (2007).

148. Hunt, W. E. & Hess, R. M. Surgical risk as related to time of intervention in the repair of intracranial aneurysms. *Journal of neurosurgery* **28,** 14–20 (1968).

149. Fisher, C. M., Kistler, J. P. & Davis, J. M. Relation of Cerebral Vasospasm to Subarachnoid Hemorrhage Visualized by Computerized Tomographic Scanning. *Neurosurgery* **6,** 1–9 (1980).

150. Lyden, P., Brott, T., Tilley, B., Welch, K. M., Mascha, E. J., Levine, S., Haley, E. C., Grotta, J. & Marler, J. Improved reliability of the NIH Stroke Scale using video training. NINDS TPA Stroke Study Group. *Stroke* **25,** 2220–2226 (1994).

151. Buckley, E. M., Lynch, J. M., Goff, D. A., Schwab, P. J., Baker, W. B., Durduran, T., Busch, D. R., Nicolson, S. C., Montenegro, L. M., Naim, M. Y., Xiao, R., Spray, T. L., Yodh, A., Gaynor, J. W. & Licht, D. J. Early postoperative changes in cerebral oxygen metabolism following neonatal cardiac surgery: Effects of surgical duration. *The Journal of Thoracic and Cardiovascular Surgery* **145,** 196–205.e1 (2013).

152. Oliveira, M. L., de Azevedo, D., de Azevedo, M., Nogueira, R. C., Teixeira, M. & Bor-Seng-Shu, E. Encephalic hemodynamic phases in subarachnoid hemorrhage: how to improve the protective effect in patient prognoses. *Neural Regeneration Research* **10,** 748 (2015).

153. Martin, N. A., Patwardhan, R. V., Alexander, M. J., Africk, C. Z., Lee, J. H., Shalmon, E., Hovda, D. A. & Becker, D. P. Characterization of cerebral hemodynamic phases following severe head trauma: hypoperfusion, hyperemia, and vasospasm. *Journal of Neurosurgery* **87,** 9–19 (1997).

154. Carpenter, D. A., Grubb, R. L., Tempel, L. W. & Powers, W. J. Cerebral oxygen metabolism after aneurysmal subarachnoid hemorrhage. *Journal of Cerebral Blood Flow and Metabolism* **11,** 837–844 (1991).

155. Yundt, K. D., Grubb, R. L., Diringer, M. N. & Powers, W. J. Autoregulatory Vasodilation of Parenchymal Vessels is Impaired during Cerebral Vasospasm. *Journal of Cerebral Blood Flow & Metabolism* **18,** 419–424 (1998).

156. Oddo, M., Levine, J. M., Frangos, S., Maloney-Wilensky, E., Carrera, E., Daniel, R. T., Levivier, M., Magistretti, P. J. & LeRoux, P. D. Brain Lactate Metabolism in Humans With Subarachnoid Hemorrhage. *Stroke* **43,** 1418–1421 (2012).

157. Yokose, N., Sakatani, K., Murata, Y., Awano, T., Igarashi, T., Nakamura, S., Hoshino, T. & Katayama, Y. Bedside Monitoring of Cerebral Blood Oxygenation and Hemodynamics after Aneurysmal Subarachnoid Hemorrhage by Quantitative Time-Resolved Near-Infrared Spectroscopy. *World Neurosurgery* **73,** 508–513 (2010).

158. de Lima Oliveira, M., Kairalla, A. C., Fonoff, E. T., Martinez, R. C. R., Teixeira, M. J. & Bor-Seng-Shu, E. Cerebral Microdialysis in Traumatic Brain Injury and Subarachnoid Hemorrhage: State of the Art. *Neurocritical Care* **21,** 152–162 (2013).

159. Carey, J. R., Kimberley, T. J., Lewis, S. M., Auerbach, E. J., Dorsey, L., Rundquist, P. & Ugurbil, K. Analysis of fMRI and finger tracking training in subjects with chronic stroke. *Brain* **125,** 773–788 (2002).

160. Lindenberg, R., Renga, V., Zhu, L. L., Nair, D. & Schlaug, G. Bihemispheric brain stimulation facilitates motor recovery in chronic stroke patients. *Neurology* **75,** 2176–2184 (2010).

161. Schaechter, J. D., Kraft, E., Hilliard, T. S., Dijkhuizen, R. M., Benner, T., Finklestein, S. P., Rosen, B. R. & Cramer, S. C. Motor Recovery and Cortical Reorganization after Constraint-Induced Movement Therapy in Stroke Patients: A Preliminary Study. *Neurorehabilitation and Neural Repair* **16,** 326–338 (2002).

162. Johansen-Berg, H., Rushworth, M. F. S., Bogdanovic, M. D., Kischka, U., Wimalaratna, S. & Matthews, P. M. The role of ipsilateral premotor cortex in hand movement after stroke. *Proceedings of the National Academy of Sciences* **99,** 14518–14523 (2002).

163. Papanikolaou, J., Makris, D., Karakitsos, D., Saranteas, T., Karabinis, A., Kostopanagiotou, G. & Zakynthinos, E. Cardiac and central vascular functional alterations in the acute phase of aneurysmal subarachnoid hemorrhage. *Critical Care Medicine* **40,** 223–232 (2012).

164. Messerer, M., Daniel, R. T. & Oddo, M. Neuromonitoring after major neurosurgical procedures. *Minerva anestesiologica* **78,** 810–22 (2012).

165. Sarrafzadeh, A., Schlenk, F., Meisel, A., Dreier, J., Vajkoczy, P. & Meisel, C. Immunodepression After Aneurysmal Subarachnoid Hemorrhage. *Stroke* **42,** 53–58 (2011).

166. Gagnon, L., Desjardins, M., Jehanne-Lacasse, J., Bherer, L. & Lesage, F. Investigation of diffuse correlation spectroscopy in multi-layered media including the human head. *Optics Express* **16,** 15514 (2008).

167. Verdecchia, K., Diop, M., Lee, A., Morrison, L. B., Lee, T.-Y. & St. Lawrence, K. Assessment of a multi-layered diffuse correlation spectroscopy method for monitoring cerebral blood flow in adults. *Biomedical Optics Express* **7,** 3659 (2016).

168. Liemert, A. & Kienle, A. Light diffusion in N-layered turbid media: steady-state domain. *Journal of Biomedical Optics* **15,** 025003 (2010).

169. Liemert, A. & Kienle, A. Light diffusion in a turbid cylinder II Layered case. *Optics Express* **18,** 9266 (2010).

170. Hallacoglu, B., Sassaroli, A. & Fantini, S. Optical Characterization of Two-Layered Turbid Media for Non-Invasive, Absolute Oximetry in Cerebral and Extracerebral Tissue. *PLoS ONE* **8** (ed Hoshi, Y.) e64095 (2013).

171. Alexandrakis, G., Busch, D. R., Faris, G. W. & Patterson, M. S. Determination of the optical properties of two-layer turbid media by use of a frequency-domain hybrid Monte Carlo diffusion model. *Applied Optics* **40,** 3810 (2001).

172. Martelli, F., Sassaroli, A., Del Bianco, S., Yamada, Y. & Zaccanti, G. Solution of the time-dependent diffusion equation for layered diffusive media by the eigenfunction method. *Physical Review E - Statistical Physics, Plasmas, Fluids, and Related Interdisciplinary Topics* **67,** 14 (2003).

173. Goyal, M. *et al.* Endovascular thrombectomy after large-vessel ischaemic stroke: A meta-analysis of individual patient data from five randomised trials. *The Lancet* **387,** 1723–1731 (2016).

174. Powers, W. J. *et al.* 2018 Guidelines for the Early Management of Patients With Acute Ischemic Stroke: A Guideline for Healthcare Professionals From the American Heart Association/American Stroke Association. *Stroke* **49,** e46–e110. eprint: `1608.04207` (2018).

175. Zaidat, O. O. *et al.* Recommendations on angiographic revascularization grading standards for acute ischemic stroke: A consensus statement. *Stroke* (2013).

176. Gomis, M. & Dávalos, A. Recanalization and Reperfusion Therapies of Acute Ischemic Stroke: What have We Learned, What are the Major Research Questions, and Where are We Headed? *Frontiers in Neurology* **5** (2014).

177. Chamorro, Á., Blasco, J., López, A., Amaro, S., Román, L. S., Llull, L., Renú, A., Rudilosso, S., Laredo, C., Obach, V., Urra, X., Planas, A. M., Leira, E. C. & MacHo, J. Complete reperfusion is required for maximal benefits of mechanical thrombectomy in stroke patients. *Scientific Reports* **7,** 1–7 (2017).

178. Soares, B. P., Tong, E., Hom, J., Cheng, S. C., Bredno, J., Boussel, L., Smith, W. S. & Wintermark, M. Reperfusion is a more accurate predictor of follow-up infarct volume than recanalization: A proof of concept using CT in acute ischemic stroke patients. *Stroke* **41,** 34–41 (2010).

179. Tomsick, T. Long-Term Clinical Follow-Up of Therapeutic Internal Carotid Artery Occlusion. *American Journal of Neuroradiology* **28,** 1626–1626 (2007).

180. Eilaghi, A., Brooks, J., D'Esterre, C., Zhang, L., Swartz, R. H., Lee, T. Y. & Aviv, R. I. Reperfusion is a stronger predictor of good clinical outcome than recanalization in ischemic stroke. *Radiology* **269,** 240–248 (2013).

181. Middleton, A. A. & Fisher, D. S. Discrete scatterers and autocorrelations of multiply scattered light. *Physical Review B* **43,** 5934–5938 (1991).

182. Durduran, T., Yu, G., Burnett, M. G., Detre, J. A., Greenberg, J. H., Wang, J., Zhou, C. & Yodh, A. G. Diffuse optical measurement of blood flow, blood oxygenation, and metabolism in a human brain during sensorimotor cortex activation. *Optics Letters* **29,** 1766 (2004).

183. Dawson, S. L., Panerai, R. B. & Potter, J. F. Serial changes in static and dynamic cerebral autoregulation after acute ischaemic stroke. *Cerebrovascular Diseases* **16,** 69–75 (2003).

184. Jordan, J. D. & Powers, W. J. Cerebral autoregulation and acute ischemic stroke. *American Journal of Hypertension* (2012).

185. Kofke, W. A., Dong, M. L., Bloom, M., Policare, R., Janosky, J. & Sekhar, L. Transcranial Doppler ultrasonography with induction of anesthesia for neurosurgery. *Journal of Neurosurgical Anesthesiology* **6,** 89–97 (1994).

186. Soares, B. P., Chien, J. D. & Wintermark, M. MR and CT monitoring of recanalization, reperfusion, and penumbra salvage: Everything that recanalizes does not necessarily reperfuse! *Stroke* **40,** 24–28 (2009).

187. Dalkara, T. & Arsava, E. M. *Can restoring incomplete microcirculatory reperfusion improve stroke outcome after thrombolysis* 2012.

188. Stullken Edward H., M. D., Milde, J. H., Michenfelder John D., M. D. & Tinker John H., M. D. The Nonlinear Responses of Cerebral Metabolism to Low Concentrations of Halothane, Enflurane, Isoflurane, and Thiopental. *Anesthesiology: The Journal of the American Society of Anesthesiologists* **46,** 28–34 (1977).

189. Nellgård, B., Mackensen, G. B., Pineda, J., Wellons, J. C., Pearlstein, R. D. & Warner, D. S. Anesthetic Effects on Cerebral Metabolic Rate Predict Histologic Outcome from Near-complete Forebrain Ischemia in the Rat. *Anesthesiology: The Journal of the American Society of Anesthesiologists* **93,** 431–436 (2000).

190. Slupe, A. M. & Kirsch, J. R. Effects of anesthesia on cerebral blood flow, metabolism, and neuroprotection. *Journal of Cerebral Blood Flow & Metabolism* **38,** 2192–2208 (2018).

191. Liemert, A. & Kienle, A. Light diffusion in a turbid cylinder I Homogeneous case. *Optics Express* **18,** 9456 (2010).

192. Jermyn, M., Ghadyani, H., Mastanduno, M. A., Turner, W., Davis, S. C., Dehghani, H. & Pogue, B. W. Fast segmentation and high-quality three-dimensional volume mesh creation from medical images for diffuse optical tomography. *Journal of Biomedical Optics* **18,** 086007 (2013).

193. Dehghani, H., Eames, M. E., Yalavarthy, P. K., Davis, S. C., Srinivasan, S., Carpenter, C. M., Pogue, B. W. & Paulsen, K. D. Near infrared optical tomography using NIRFAST: Algorithm for numerical model and image reconstruction. *Communications in Numerical Methods in Engineering* **25,** 711–732 (2009).